Design, Fabrication and Evaluation of Photo-activated Gas Sensors based on

Semiconducting Nanostructures

by

Ehsan Espid

B.A.Sc., University of Tehran, 2012
M.A.Sc., University of Tehran, 2014
M.A.Sc., University of British Columbia, 2015

A THESIS SUBMITTED IN PARTIAL FULFILLMENT OF

THE REQUIREMENTS FOR THE DEGREE OF

DOCTOR OF PHILOSOPHY

in

THE FACULTY OF GRADUATE AND POSTDOCTORAL STUDIES

(CHEMICAL AND BIOLOGICAL ENGINEERING)

THE UNIVERSITY OF BRITISH COLUMBIA

(Vancouver)

The following individuals certify that they have read, and recommend to the Faculty of Graduate and Postdoctoral Studies for acceptance, the dissertation entitled:

Design, Fabrication and Evaluation of Photo-activated Gas Sensors based on Semiconducting Nanostructures

submitted by   Ehsan Espid   in partial fulfillment of the requirements for

the degree of   Doctor of Philosophy

in   Chemical and Biological Engineering

Examining Committee:

Fariborz Taghipour, Chemical and Biological Engineering

Supervisor

John Madden, Electrical & Computer Engineering

Supervisory Committee Member

David Wilkinson, Chemical and Biological Engineering

Supervisory Committee Member

Peyman Servati, Electrical & Computer Engineering

University Examiner

Előd Gyenge, Chemical and Biological Engineering

University Examiner

Abstract

In this research, UV-LED-activated metal-oxide gas sensors were studied, where the electrochemical properties of the sensing material were enhanced by manipulation of sensor operating parameters as well as material structure and composition.

In the first phase, the sensing characteristics of several favorable metal oxide semiconductors were investigated under different wavelengths, irradiances, and pulsation frequencies. The results showed that UVA-LEDs (i.e. 365 nm) could result in better responses due to resonant absorption. At a constant photon energy (i.e. 3.4 eV), increasing irradiance enhanced the photo-desorption of adsorbed components and reduced the response. Pulsed UV irradiation could significantly enhance the response as a result of increased residence time of adsorbates.

Also, a set of strategies were applied to investigate and modify the sensing layer structure and composition. Firstly, Ag was incorporated into ZnO nanoparticle structure which resulted in an increase in sensor response toward 5 ppm NO_2 ($\Delta R/R = 0.98$), compared to pristine ZnO (0.5) potentially due to layer charge carrier enhancement. Secondly, a sensing material structure was designed based on ZnO nanowires decorated with Pt nanoparticles, as metallic co-catalytic sites. The ZnO nanowires showed an increased response (1.6) compared to nanoparticles due to their higher surface area. Furthermore, decorating the surface of ZnO nanowires with Pt nanoparticles remarkably enhanced the sensing performance, whereas 0.1 wt% Pt decorated ZnO nanowires sensor exhibited nearly 4-times higher and 50s faster response compared to ZnO nanoparticles, in identical photo-activation settings. Thirdly, ZnO nanowires were used as a core for a thin layer of a secondary semiconductor to develop ZnO-In_2O_3 and ZnO-SnO_2 core-shell gas sensors. The relative responses of the ZnO-In_2O_3 (2.49) and ZnO-SnO_2 (2.21) sensors were higher than that of pristine ZnO NWs (1.6), possibly due to the improved photon absorption, and increased active sites on the surface of the nanowires.

Lastly, carbon mesoporous materials (CMMs) with various ZnO loading concentrations were tested against NO_2 and NH_3, where the sensors responded 1.91 (NO_2) and 1.35 (NH_3) in optimal loading concentrations. This improvement in response could be attributed to the high surface area, extended separation, and more oxygen vacancies (O_{Vac}) induced by C-dopant in ZnO_x/CMM sensors.

Lay Summary

Detecting and monitoring hazardous gases and gas pollutants in industrial and urban settings is of increasing importance. Chemical gas sensors are one of the most promising devices for gas detection. However, a drawback of conventional chemical-resistive gas sensors is the high operating temperature (200°C to 500°C), which results in high cost and high power consumption, and most importantly limits their technical applicability in the detection of flammable gases. UV-LED activated gas sensing is a new technological field that can address these challenges and provide significant cost, energy, and space savings.

In this research, we studied UV-LED activated metal oxide semiconductor gas sensors, where the electrochemical properties of the sensing material were significantly enhanced by the manipulation of material structure and composition, as well as the optimization of operating parameters and identification of suitable design features.

Preface

This dissertation is original and is co-authored with my research supervisor, Prof. Fariborz Taghipour. All of the work presented henceforth was conducted in the Photoreaction Engineering Laboratory in the Chemical and Biological Engineering Department at the University of British Columbia, Vancouver campus. The experimental apparatus used in this research was designed, fabricated and programmed by the Author.

E. Espid was the contributor of preparation, characterization and analyzing the sensors and writing of the manuscripts. Prof. Fariborz Taghipour largely contributed to the development of experimental plans, the discussion of the results, and the revision of the manuscript drafts. The experiments on the gas sensing performances of the developed sensors under different radiation conditions, presented in Chapter 3, were mainly performed by Alice Satomi Noce, from State University of Maringá (UEM) in Brazil, during a time that she was a fellow of the Science without Borders program at the University of British Columbia. The basic idea of the research work presented in Chapter 5, and some of the materials were prepared in collaboration with Dr. Babak Adeli, during his Ph.D. study in the Chemical and Biological Engineering Department at the University of British Columbia. The research work presented in Chapter 7 was performed with the help of Dr. An-Ya Lo from National Chin-Yi University of Technology, Taichung, Taiwan, during his sabbatical stay at the University of British Columbia. Dr. An-Ya Lo contributed in presenting the idea and the preparation and characterization of the sensing materials.

By the time of submitting this thesis, 5 research papers have been published in international journals, 2 submitted, and 1 is under preparation.

1) **Ehsan Espid**, Aline Satomi Noce, Fariborz Taghipour, "The effect of radiation parameters on the performance of photo-activated gas sensors", J. of Photo-chemistry and photobiology A: Chemistry, 374, 95-105, (2019) – **Related to Chapter 3**

2) **Ehsan Espid**, Fariborz Taghipour, "Facile synthesis and UV-Activated gas sensing performance of Ag:ZnO nano-ellipsoids", Journal of Solid State Science and Technology, 7 (7), 3089-3093, (2018) – **Related to Chapter 4**

3) **Ehsan Espid**, Babak Adeli, Fariborz Taghipour, "Enhanced gas sensing performance of photo-activated, Pt-decorated, single-crystal ZnO nanowires", Journal of Electrochemical Society, 166, 5, H3223-H3230, (2019) – **Related to Chapter 5**

4) **Ehsan Espid**, Babak Adeli, Fariborz Taghipour, "UV-LED activated semiconductor sensors with tailored structure", SPIE Optics + Photonics 11086-40 (2019) – **Related to Chapter 5**

5) Babak Adeli, **Ehsan Espid**, Fariborz Taghipour, "Selective Sensing Performance of Metal Nanoparticles Decorated ZnO Nanowires Induced by Ultraviolet Light Emitting Diodes", *submitted* – **Related to Chapter 5**

6) **Ehsan Espid**, Fariborz Taghipour, "Synthesis of ZnO-In$_2$O$_3$ and ZnO-SnO$_2$ core–shell nanowires and their application in photo-activated gas sensing", *to be submitted* – **Related to Chapter 6**

7) **Ehsan Espid**, An Ya Lo, Fariborz Tahipour, "ZnO nanoparticles on ordered carbon mesoporous materials as highly efficient UV-LED activated gas sensors", *submitted* – **Related to Chapter 7**

8) **Ehsan Espid**, Fariborz Taghipour, "UV-LED photo-activated chemical gas sensors: a review", Critical Reviews in Solid State and Materials Sciences, Taylor & Francis, (2017) – **Review Paper**

And 6 presentations have been made in international conferences:

1) **Ehsan Espid,** Fariborz Taghipour, "Semiconducting nanostructures for photo-activated gas sensing application", Sensors Europe 2019 and IDETechX Exhibition, Berlin, April 10-12 (2019)

2) **Ehsan Espid,** Fariborz Taghipour, "Synthesis and application of UV-LED activated "metal-oxide+metal-naonparticle" Gas Sensors, International UV Association (IUVA) World Congress, Sydney, Australia, February 10–13 (2019)

3) **Ehsan Espid,** Fariborz Taghipour, "Design, fabrication and performance evaluation of photo-activated micro gas sensors based on semiconducting nanostructures", CMC NanoTEC for Smart Communities, Toronto, October 20–24 (2018)

4) **Ehsan Espid**, Fariborz Taghipour, "UV-LED activated semiconductor composites: a leading technology towards gas sensing application", 68th Canadian Chemical Engineering Conference, Toronto, October 28–31 (2018)

5) **Ehsan Espid,** Fariborz Taghipour, "Development and application of UV-LED gas sensing devices", International Conference on UV LED Technologies & Applications, Berlin, April 22–25 (2018)

6) **Ehsan Espid**, Fariborz Taghipour, "Application of UV-LED in photo-activated chemical gas sensors", IUVA World Congress & Exhibition, Vancouver, January 31–February 03 (2016)

Table of Contents

x

List of Tables

List of Figures

List of Acronyms

BET	Brunauer-Emmett-Teller
CVD	chemical vapor deposition
CB	conduction band
E_g	band-gap energy
eV	electron volt
EBPVD	e-Beam Physical Vapour Deposition
EDX	energy-dispersive X-ray spectroscopy
FE-SEM	field emission scanning electron microscope
FWHM	full width at half maximum
GC	gas chromatography
LED	light-emitting diode
MOS	metal oxide semiconductor
PCB	printed circuit board
PECVD	plasma-Enhanced chemical vapor deposition
ppm	part per million
RH	relative humidity
RGTO	rheotaxial growth and thermal oxidation
SEM	scanning electron microscope
TEC	thermo-electric cooler
TLV	threshold limit value
UV	ultraviolet
VB	valence band
VIS	visible
VOC	volatile organic compound
XPS	X-ray photoelectron spectroscopy
XRD	X-ray diffraction

Glossary

- **Detection Limit:** The lowest concentration of the analyte that can be detected at any given condition.

- **Dynamic Range:** Total range changeable parameter in a sensor from the smallest possible values to the largest quantity.

- **Intensity:** The quantity of light that is emitted in unit time per unit solid angle.

- **Irradiance:** The rate of light actually striking the surface of objects per unit area. It depends upon the intensity and distance of the light source.

- **Response Time:** The time that it takes for sensor to respond to ambient gas going from 10% to 90% of the maximum resistance variation.

- **Recovery Time:** The time that it takes for the sensor signal to return from 90% to 10% of its maximum value.

- **Resolution:** The smallest change in concentration that can be distinguished by sensor.

- **Response:** The change in output resistance signal per background resistance in pure air.

- **Sensitivity:** The change in sensor response per measured gas concentrations.

- **Selectivity:** The ability of the sensor to discriminate between various components of a gas mixture and provide signal for the component of interest.

- **Sensing Range:** The specified range which sensor is designed to work over.

- **Stability:** The reproducibility of the sensor measurements for a certain period of time. This includes retaining the sensitivity, selectivity, response, and recovery time.

- **Working Temperature/irradiance:** The temperature/irradiance at which the sensor can operate in fully efficient mode.

Acknowledgements

First and foremost, I would like to express my deep gratitude to my supervisor, Prof. Fariborz Taghipour who supported me to work in this field. He kindly monitored my progress, discussed my results and supported me with his highly valued advices and suggestions.

I also would like to express my deep gratitude to Prof. David Wilkinson and Prof. John Madden who served in my committee, for their constructive questions and advices during the project.

And thanks to my friends, lab-mates and all CHBE community for their support and the wonderful environment.

Finally, but certainly no less important, I greatly thank my parents, my sisters, and my wife whose continuous love, sacrifice, support and encouragement have allowed me to pursue my ambitions.

This work is dedicated to my family.

Chapter 1: **Introduction**

The increasing amount of atmospheric pollutants is one of the main problems that the world is facing today, specifically in urban and industrial areas. Air pollutants can come from both natural sources such as forest fires, volcanoes, bacteria, or chemicals released by plants and animals, and pollutants attributed to the sources made by humans [1]. The latter is mainly related to industrial activities and enormous injurious smoke emissions by cars, trucks, trains, and factories.

Several methods have been proposed for detecting hazardous gases. Gas chromatography (GC) and mass spectrometry (MS) are the most commonly used systems developed for gas analysis. Although GC and MS provide high accuracy and reliability, they are bulky, expensive, and time-consuming, and require highly skilled personnel. Thus, the need for miniaturized gas sensor devices has been increased significantly, motivating researchers to manufacture gas sensors with high performance and reliable stability.

The schematic of different parts of a gas sensor device is depicted in Figure 1-1. Four components of the gas detection instrument are as follow:

1) Delivering the target gas to be detected to the chamber where the sensor array is located

2) The reaction of the gas molecules with the sensing material, resulting in electrical signals

3) Amplification and recording of the electrical signals using an interface circuit

4) Analyzing the data, extracting the features from the signals, and recognizing the pattern of each signal (using different pattern recognition techniques), resulting in gas mixture detection
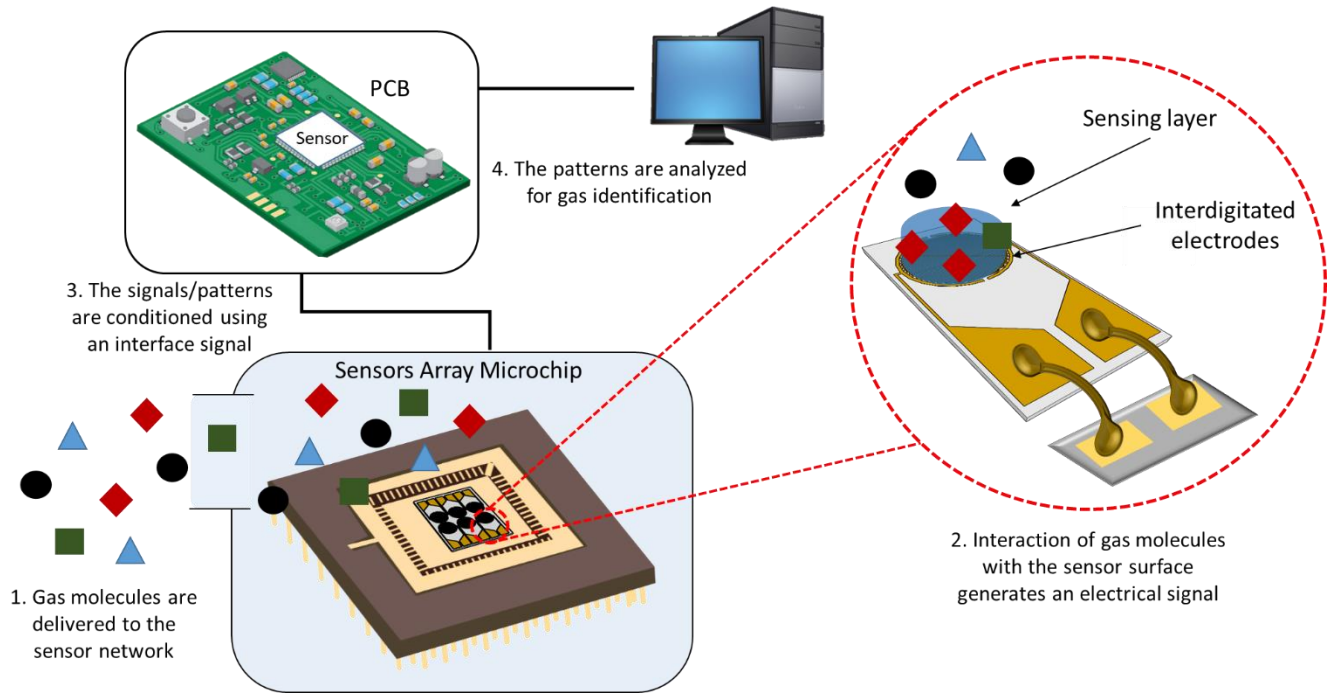
Figure 1-1: The components in different stages of smell detection using e-nose devices

1.1 Demand-controlled ventilation

Air pollutants may enter the building with outside air or may be generated internally. According to the Health Canada Organization, indoor air pollutants can lead to the onset/worsening of lung cancer, asthma, allergies, heart attacks, strokes, and various breathing problems [2]. Ventilation is one method to maintain good indoor air quality. Buildings without proper ventilation will have high indoor pollutant concentrations, which can cause adverse health effects (resulting in broad impacts, such as 'sick building' syndrome, in some cases).

Currently, in many commercial spaces such as offices, retail stores, and institutional departments, the buildings are continuously ventilated based on the assumption that they are always at peak pollutant concentrations (including significant safety factors). This will ensure to keep the indoor air quality (IAQ)

within acceptable limits for both the health and comfort of the occupants. However, most buildings never even get above standard concentrations. Over-ventilation increases heating and cooling loads, as well as fan usage, all of which contribute to increased energy consumption, especially in cities where humidity is high. It has been noticed that over 30% of the annual heating and cooling cost is spent in handling the fresh air in a typical office building [3], and 40-100% energy savings can be achieved, versus a fixed ventilation strategy, depending on climate and building type [4]. Therefore, the use of operationally cost-effective ventilation control systems, known as demand-controlled ventilation (DCV), is essential in buildings to estimate the concentration of the pollutant gases and adjust the ventilation rate accordingly.

In recent years, CO_2 concentration has been widely used to measure the building occupancy as it is an excellent surrogate gas for the levels of occupant-related contaminants [5,6]. Based on the actual occupancy, the outdoor air supply rate per person recommended in the industry standards such as American Society of Heating, Refrigerating and Air-Conditioning Engineers (ASHRAE) volume 62-1999 [7] can be met, and over-ventilation can be avoided.

However, the CO_2 based DCV can only guarantee that the fresh air intake is enough to dilute the occupant-related pollutants, and it does not take into account the non-occupant-related pollutants. ASHRAE 62-1999 points out that using CO_2 as the indicator of bio-effluents does not eliminate the need to consider other contaminants, several of which have received increasing attention in recent years such as NOx, SOx and VOCs. Common residential indoor pollutants have been shown in Figure 1-2. Therefore, there is a need for a new demand-controlled ventilation strategy that takes some of the occupant-related and non-occupant-related indoor air pollutants into consideration. The new approach must rely on novel micro-gas sensing networks that can detect low concentrations of several pollutant gases.
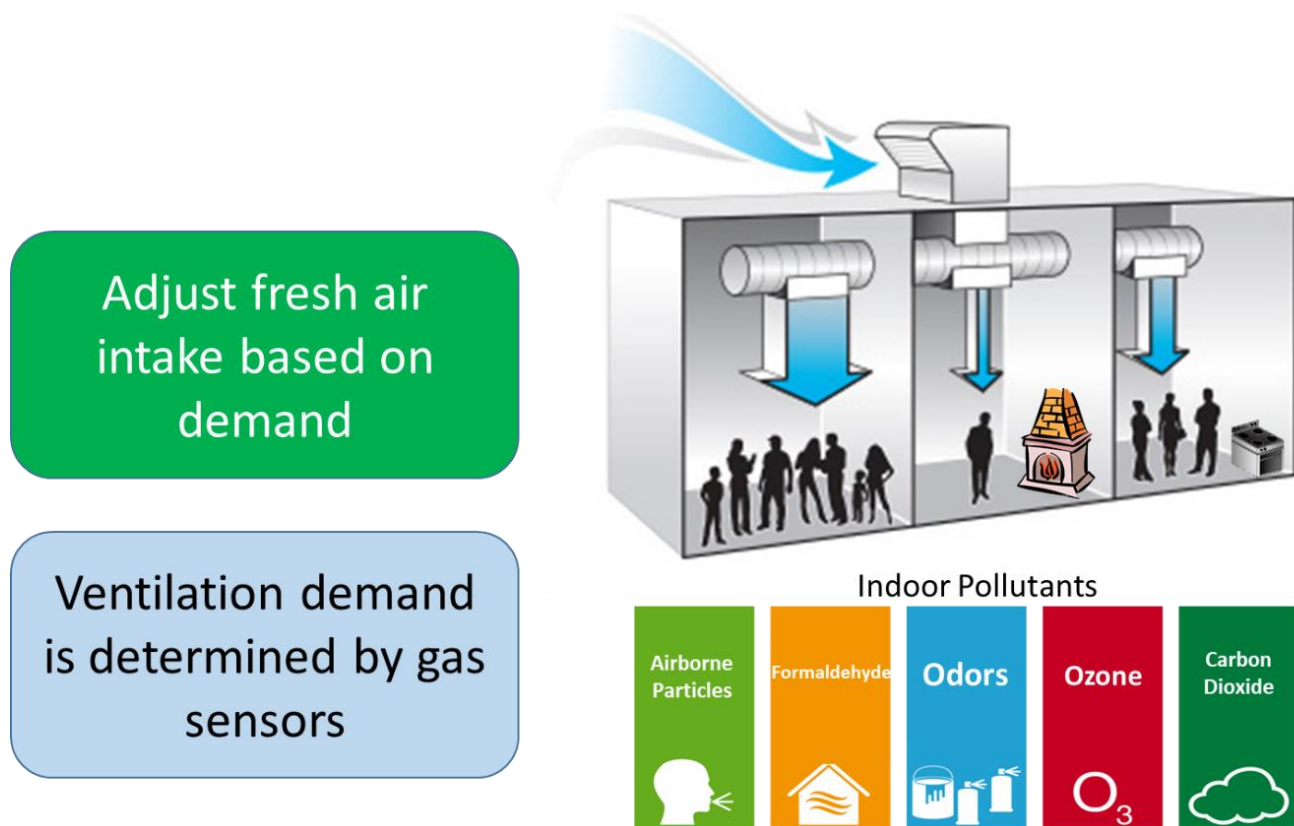
Figure 1-2: Indoor air monitoring and smart demand control ventilation based on gas sensor networks

1.2   Hazardous gases

Increasing amounts of atmospheric pollutants, specifically in urban and industrial areas, has been a major concern recently. Hazardous gases in the atmosphere include toxic materials such as H_2S, CO, and NH_3, greenhouse gases such as CH_4 and CO_2, and some special gases such as NO_2 and NO, which are both toxic and greenhouse gases and may emanate from both natural and human sources. Among the released atmospheric pollutant gases, Nitrogen Dioxide which is produced substantially through chemical combustion plants and automobiles, significantly contributes to human and environmental problems.

1.2.1   Nitrogen dioxide (NO_2)

Nitrogen dioxide, a reddish-brown gas, is part of a highly reactive family known as "oxides of nitrogen" that includes several gases that are composed of oxygen and nitrogen.

Fuel combustion for energy production, home, and industrial use, accounts for approximately 94% of the emissions of nitrogen oxides produced by human activities in Canada (Health Canada, 2015). It causes severe respiratory infection diseases through irritating and impairing lung function. In the atmosphere, it contributes to the formation of ground-level ozone and turns into nitric acid that is the main component of acid rain.

Exposure to NO_2 from outdoor sources strongly depends on the proximity to the source. Given that mobile sources (i.e. automobiles) are the main contributors to ambient NO_2, the NO_2 levels may vary considerably between buildings. As discussed earlier, these emissions may become significant in indoor environments if the area is poorly vented.

The threshold limit value (TLV) is considered as the maximum concentration of a chemical allowed for long time exposure without making health problems. The TLV of NOx compounds is 5 ppm; thus, exposure to higher levels must be avoided.

Exposure to 50 ppm NO_2 results in pulmonary edema, and it is fatal if being inhaled at concentrations above 100 ppm. Recently, epidemiological scientists revealed that the development of chronic lung disease and respiratory symptoms are related to exposure to NO_2. Although the effects of short-term exposure are still unclear, long term exposure to concentrations that are higher than those generally found in the ambient may cause an increased incidence of acute respiratory illness in children [9]. Therefore, NO_2 continuous monitoring provides indices of exposure over time.

1.3 Overview of gas sensing technologies

Gas sensors perform based on a change in a physical characteristic (such as mass, conductivity, transmittance, or capacitance) upon exposure to gas. Depending on the sensing mechanism, gas sensors are divided into several categories, optical sensors, piezoelectric sensors, electrochemical sensors, and solid-state resistive gas sensors are four of the commonly utilized classes [10,11]. Figure 1-3 shows various types of available gas sensors. Every sensor has some pros and cons, so depending on the sort of the facility, the appropriate gas detection system must be selected. Among all, solid-state chemical gas sensors have some distinct advantages such as simplicity, fast response, and low cost. They have shown promise in detecting a broad range of gases including toxic and combustible vapors.
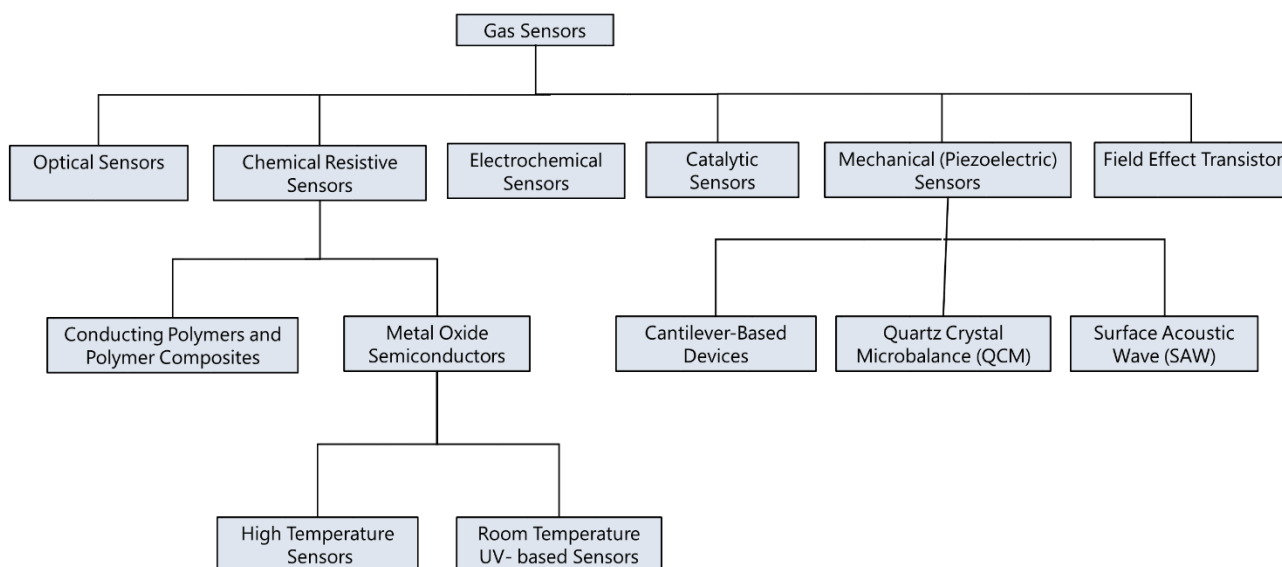
Figure 1-3: Various types of gas sensors available in the market [12]

1.3.1 Metal oxide semiconductor (MOS) gas sensors

Solid-state chemical resistive gas sensors typically consist of semiconductors as the sensing material to detect gases. The interactions of the surrounding gas to be identified with the sensing layer in resistive sensors result in resistance variations of the thin film layer due to the difference in the flow of electrons involved in the sensing reactions.

The beginning of metal oxide semiconductor (MOS) gas sensors production backs to 1957, following to a vital work triggered by Bielanski et al. [13] that showed a relation between the electrical conductivity and catalyst activity of semiconductors. Seiyama et al. [14] revealed that the gas-semiconductor interactions cause a marked change in electrical conductivity and suggested the idea of having a thin film gas chromatographic detector instead of the ordinary thermal conductivity cells.

The first commercial MOS gas sensor was manufactured by Taguchi, in 1962 (Figure 1-4), capable of detecting low concentrations of combustible and reducing gases based on thick films of SnO_2 [15].
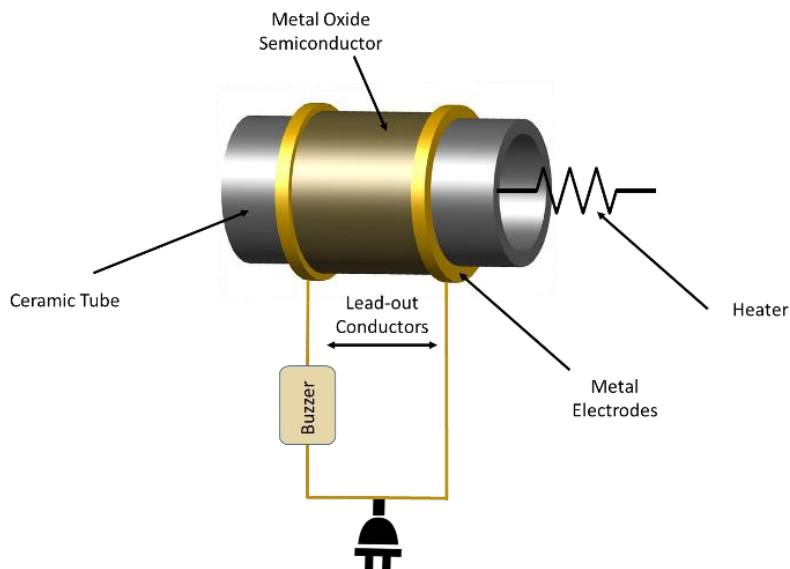
Figure 1-4: A schematic illustration of the first manufactured MOS gas sensor [12]

In developing resistive gas sensors, the efforts were mainly directed to reversible oxidation/reduction reactions in which excited electrons induced by thermal activations played a crucial role in the sensing process. The mechanism of these sensors is based on the reaction of the generated electrons within the sensing layer with the ambient oxygen or surrounding gas. Adsorption of oxygen molecules on the surface of metal oxides is accompanied by an electron extraction from the conduction band, leading to the formation of an electron-depleted region and band bending. Removing oxygen ions by their reaction with the surrounding gases or replacement of the adsorbed oxygens by other molecules can reverse the band bending, resulting in an increased conductivity that could indicate the amount and type of the gas to be detected [16].

1.3.2   Basics of semiconductor electron structure

Based on the Bohr model, the electrons of a single, isolated atom travel in circular orbits around the nucleus. These orbits, also known as energy shells or energy levels, are associated with definite energies (quantum rule). However, the electrons in a molecule are not only affected by their own nucleus, but also by other atom's nuclei (attraction) and electrons (repulsion). Band theory, explains the physical properties of solid-state devices, such as electron arrangements, electrical resistivity, and optical absorption. Based on the band theory, as atoms are brought together to form a molecule, their atomic orbitals combine and form molecular orbitals, each of which forms at a discrete energy level. A molecular orbital can specify the electron configuration of a molecule, the spatial distribution, and the energy of one (or one pair of) electron(s). Like single atoms, the orbitals are filled starting with the lowest energy. The states and the difference of the energies of the two highest orbitals play a determining role in the solid physical behavior. The valence band (E_v) in a molecule is the highest occupied band level by electrons, while the conduction band (E_c) is the lowest unoccupied band level. The energy difference

8

from the top of the valence band to the bottom of the conduction band is defined as the band-gap energy (E_g). For an electron to become free to conduct, it must be promoted to an empty available energy state. For metals, these states are adjacent to the filled states. Thus, a low energy supplied even by an electric field is enough to stimulate electrons into an empty state. For insulators, the valence band and conduction band are separated by a large (>4 eV) energy gap, which is extremely far for the electrons to pass. However, in the semiconductors, the energy gap is $2<E_g<4$ eV, which relies somewhere on between metals and insulators. Therefore, the semiconductors have a resistivity between those of metals and insulators at room temperature.

When a semiconductor receives energy from an external source (heat, photon), the electrons ascend to higher levels. Upon electron excitation, a hole is created in the valence band. Holes and excited electrons are attributed to the electrical conductivity of the semiconductor. Generated electrons then pave the way for either adsorption or direct gas-phase reactions of the target gas. These subsequent physical/chemical processes will change the flow of surface electrons, which is measured as film resistance.

1.4   State of the art of photo-activated gas sensors

As discussed earlier, conventional thermally activated metal oxide semiconductor gas sensors show sensing responses around the temperature range of 200–500 ◦C [17,18]. At high temperatures, the electrons gain adequate energy to jump from the valence band into the conduction band.

The necessity of heating the device to reach a suitable temperature makes some technical limitations in the application of these gas sensors in the environments containing explosive species since high temperatures could trigger an explosion. Heating also requires high energy and frequent maintenance and will affect the stability and economic aspects. Although miniaturization helped to develop efficient types of sensors recently, the preparation time and cost are still significant concerns. Besides, the drift issues or contamination which is very likely in high-temperature sensors introduces spurious measurements and shortens the useful lifetime of the sensor [19].

The aforementioned problems of high-temperature MOS gas sensors and the sophisticated heater design and fabrication required to maintain accurate temperature control motivated investigators toward developing sensors that are able to work at lower temperatures. For instance, they capacitively coupled nanostructures to a nearby gate electrode and applied a high electric field across the sensor terminals [20]. They also tried to utilize conducting polymer as room temperature sensors, but the materials reluctance for organic vapours limited their applications [21]. A significant breakthrough occurred in this way in 1994 by Saura [22], who described the gas sensing properties of UV radiated SnO_2 films towards trichloroethylene and acetone.

The main idea of having photo-activated gas sensors was initiated from the fact that irradiating UV to the surface of the sensor film could generate the same electron-hole pairs that normally were produced through thermal activation. Indeed, photo-excitation can increase the density of charge carriers throughout the material and can decrease the intergrain barrier height by changing the intergrain state's

charges, leading to an increase in the probability of tunneling by decreasing the depletion layer widths in the adjacent grains [17,23]. Furthermore, poisoning and deterioration of the sensing layer in harsh environments such as exposure to SO_2 or NO_x is a challenge for high-temperature resistive gas sensors [24]. In this regard, UV radiation has shown promise in desorbing surface contaminants and thus can reduce poisoning and elongate the useful lifetime of the sensor [25].

In 1996, P. Camagni et al. [26] employed Xenon UV lamps to perform photoconductivity measurements of rheotaxial growth and thermal oxidation (RGTO) SnO_2 thin films in ambient temperature. The illuminated SnO_2 sensor showed remarkable resistant changes for low concentrations of CO at room temperature compared to dark conditions. In a further study of this group, Comini et al. [23] observed that the 40 min response time of a SnO_2 gas sensor could be decreased to 10 s under UV illumination, and the sensor can return to 80% of its initial value. They then proposed that increasing irradiance (i.e. higher power UV lamp attached with optical fibers) may result in higher gas sensitivity towards NO_2 [27].

In a parallel work performed by K. Anothainart et al. [28] on sputtered SnO_2 samples, they observed that the desorption depends on the radiation intensity, in which increasing the intensity causes decreasing time constants for desorption and thus helps to reduce poisoning by an enhancement in desorption process.

During the last decade, room temperature UV-based gas sensing technology has attracted attention due to its increasing role in human's life [18,28–35]. Until recent years, the primary technique for industrial production of UV relied on energizing mercury vapour with high-voltage electric current. Electrons in the mercury atoms are excited to a higher energy state and emit energy in the form of UV, visible light and heat on the way back to the ground level. However, as will be discussed in the following, using conventional UV lamps for the activation of gas sensors was not the best option.

11

The first drawback of conventional mercury UV lamps was the broad range of emitted wavelengths that could destroy exposed materials. The high voltage applied in UV lamps could deteriorate electrode material and as a result, cause darkening or blacking of the lamp near the terminals, which imposes loss of energy and shortens the useful lifetime of the lamp. The long warm-up time required to reach the operational condition as well as the time required for internal pressure to return to the initial value were other issues associated with UV lamps. The drawbacks mentioned above, along with the harmful environmental effects and severe respiratory problems that may occur by using UV lamps, the need for smaller, greener, and more efficient replacements became progressively more important.

A key trend expected to influence the gas sensor technology and its market is the use of newly emerged ultraviolet light-emitting diodes (UV-LEDs). UV LEDs not only provide the opportunity to fully control operating parameters, but also provide significant cost, energy, and space savings compared to alternate technologies. Further, UV LEDs do not contain toxic material such as mercury often found in UV sources and thus provide major environmental benefits.

In an introductory work by Han et al. [36] on UV-LED based catalytic combustion hydrogen sensors using drop coated TiO_2 doped with palladium and platinum metals on alumina substrate, it was reported that the use of UV-LED can facilitate the oxidation of hydrogen on the surface and improve low-temperature gas sensing characteristics and self-cleaning effects of the developed sensors.

The idea of functionalizing chemical gas sensors at room temperature as well as making them smaller, greener and more efficient has initiated significant progress in the last few years among scientists worldwide. There have been several research reports in the literature in the last few years concerning the photo-activation of sensors by UV-LED. The importance and recent advances in the developments of UV-LED based chemi-resistive sensors have been discussed in a comprehensive review [12].

1.5 Gas sensing mechanism of UV illuminated metal oxide semiconductors

It is well-known that the work function of the photo-activated gas sensors is governed by various electrochemical sensing reactions that involve electrons/holes created by the interactions of photons and metal oxide surface. Although the overall logic of photo-activated gas sensing principle is generally identical, some differences exists in different types of oxidizing/reducing reactions and metal oxide semiconductor layer structures as well as the chemical properties of the gases.

In a gas sensing experiment, when air is introduced to the metal oxide semiconductor at room temperature, oxygen is adsorbed on the surface. At lower temperatures, oxygen is adsorbed molecularly, but as the temperature increases, it tends to be adsorbed in the form of O^{2-} and O^{-} [37]. Adsorption of oxygen is accompanied by an electron extraction from the conduction band, forming negative sites on the surface and positive holes in the conduction band. The separation of charge carriers makes an electric field and leads to the formation of a stable electron-depleted region. The formed potential barrier is usually between 0.5 to 1 eV that acts as a barrier for remaining electrons to be excited [16,38–41]. The negatively charged oxygen ions produce an upward band bending resulting in reducing conductivity [16]. The electrical properties of the sensing layer are determined through the sum of the contributions of the grains and the grain boundaries of the semiconductor. The height of the energy barrier for the electron transport between neighboring grains plays a determining role in the sensitivity of the sensing material.

Irradiation of a metal oxide layer by photons emanating from UV-LED with the appropriate energy changes the occupancy of the defects and thus changes the capacity of adsorption concentration on the surface by enhancing charge carriers [27]. As illustrated in Figure 1-5a, UV irradiation increases the free electron concentration on the surface and results in a decrease in the thickness of the depletion layer. This lowers the energy barrier between adjacent grains, allows the electrons to move easier across the grain boundaries, and leads to decreased film resistance.

Upon exposure to air, oxygen reacts with the excited electrons and is adsorbed molecularly at room temperature. This leads to a slight increase in the layer resistivity. (Figure 1-5b).

$$O_{2(gas)} \leftrightarrow O_{2\,(ad)} \qquad\qquad (1)$$

$$O_{2\,(ad)} + e^- \leftrightarrow O_{2(ad)}^- \qquad\qquad (2)$$
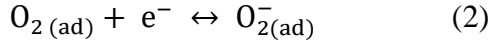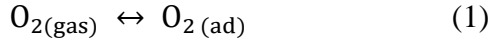
As the photons irradiate to the surface, the photo-induced holes/electrons interact with the adsorbed oxygen causing to desorb oxygen ion species (photo-desorption) simultaneously along with the interaction of the photo-induced electron with oxygen in the gas phase. This phenomenon continues to reach a new equilibrium state in which the rate of arrival of holes and electrons to the surface becomes equal [42,43]. Interaction and recombination of a hole with a binding electron of the layer could also break the bond and provide oxygen atom that can diffuse to the crystal surface, react with oxygen ions and form into $O_{2(g)}$ and leave an oxygen vacancy behind [44].

Upon exposure to an oxidizing gas, such as NO_2, it accepts electron through a reaction with O_2^-, and a stable chemisorbed NO_2^- state is created, which can only be desorbed by radiation (Figure 1-5c). Moreover, under continuous irradiation, it also reacts with photo-generated electrons, all of which result in increasing the layer resistance. The latter restores surface adsorbed O_2^- concentration and broadens the depletion region, resulting in a further increase of the resistance. Eventually, the surface adsorption and desorption processes take place simultaneously to reach an equilibrium state under the constant flow of photons.

$$NO_{2\,(g)} + O_2^- + 2e^-_{(hv)} \leftrightarrow NO_{2\,(ad)}^- + 2O^- \qquad\qquad (3)$$

$$2NO_{2(g)} + e^-_{(hv)} \rightarrow 2NO_{(g)} + O_{2\,(ad)}^- \qquad\qquad (4)$$
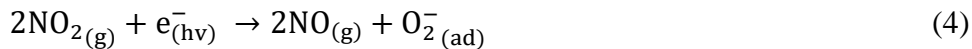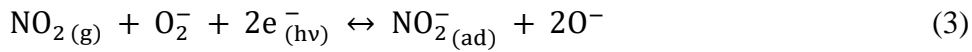
The time that takes for this process to reach an equilibrium, which is known as the response time, varies for each sensing material. The sensor identifies the gas by monitoring the layer resistivity over time, which is a function of the gas concentration.
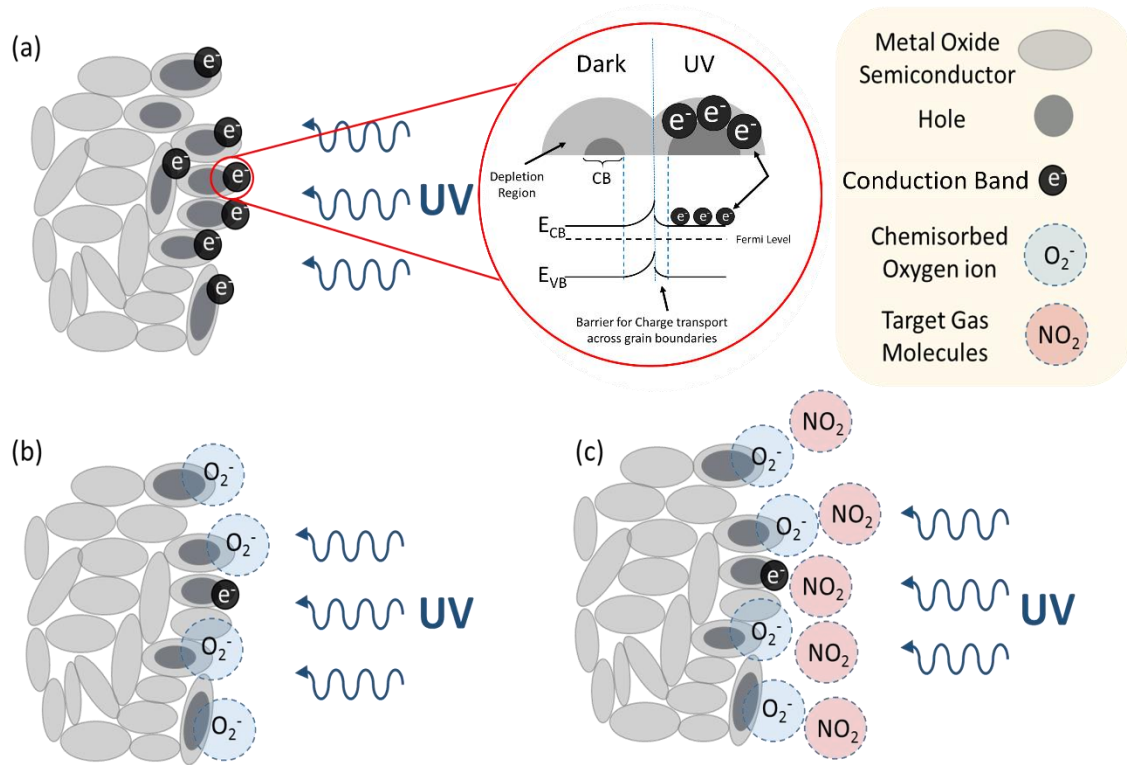
Figure 1-5: A schematic illustration of the detection mechanism of UV-LED activated sensors [45]

As the gas molecules adsorb on the surface and follow the previously described reactions, due to the electron consumption, the resistance of the n-type metal oxide layer increases. In p-type semiconductors, the resistance decreases upon exposure to the gas, because extracted electrons increase the number of holes in the valence band. A quasi-linear decrease is observed following by turning off the target gas exposure. At this step, the equilibrium reactions tend backward to produce more gaseous species. The time that takes for the sensor to recover entirely to its base value is known as the recovery time.

In case of exposure of the layer to reducing gases, the gas participates in a reaction with the adsorbed oxygen releasing and accumulating electrons back to the conduction band and resulting in a decrease of resistance in n-type semiconductors. This change in resistance is due to charge density enhancement and increase in p-type semiconductors because of the reduction in hole concentration. Example of the reactions of a reducing gas, i.e. NH_3, is presented in the following [40,46–49]:

$$4NH_3 + 3O_{2(ad)}^- \rightarrow 2N_2 + 6H_2O + 3e^- \tag{5}$$
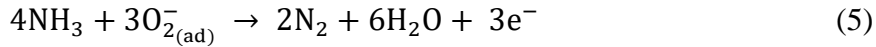
Due to the strong influence of the structural formation and surface states of sensing layer materials, the governing mechanism and sensing reactions could be subjected to alter as a result of a change in film properties such as in the presence of moisture or by addition of any dopant to the structure. For instance, it has been suggested that the possible mechanism in metal-doped semiconductor layers is different from that of pristine samples. For metal doped semiconductors, the mechanism could be explained based on the charge transfer transition of the metal ion by UV illumination, which leads to creating additional holes that react with chemisorbed oxygen ions and desorb oxygen [50].

1.6   Influencing factors on UV activated gas sensor responses

The work function of the photo-activated gas sensors is governed by various electrochemical sensing reactions that involve electrons/holes created by the interactions of photons and sensor surface at room temperature. Therefore, the three main areas that influence the gas sensing reactions, thus the sensor response, are as follow:

1.6.1   UV source parameters

As discussed earlier, UV-LEDs provide the opportunity to fully control operating parameters. This makes them a compelling candidate to replace the conventional activation sources in gas sensor devices

(i.e. heat and UV lamps). UV-LEDs have instant on/off operation and are able to produce an exact wavelength at a specific intensity.

The efficiency of chemical gas sensing in photo-activation mode is highly dependent on the radiation source specifications. The energy (i.e. wavelength) of the photons emitting from the UV source must be adequate to excite electrons within the semiconductor layer. It also has a crucial influence on electron mobility and layer stability. The intensity of the emitted radiation will affect the flow of the photons (or the irradiance on the sensor surface), which in turn influence the excitation ratio and sensing characteristics, due to the change in carriers' density. The pattern in which the photons reach the surface can also be adjusted using UV-LEDs. The frequency of the striking photon streams changes the residence time of the reacting agents and gas molecules on the surface.

While the effect of UV irradiation specifications on surface reaction kinetics has generally been accepted, the correlation between these parameters and the sensor signal has not been compared. Therefore, it is necessary to investigate the performance characteristics of commonly used sensors under various operational conditions to better specify the functionality of any given semiconductor material in practical applications.

1.6.2 Sensing layer specifications

It is well known that the performances of metal oxide sensors considerably depend on the sensing layer material and structure. The sensing performance of any metal oxide resistive gas sensor is attributed to three major independent aspects of the sensitive material: receptor function, transducer function and utility factor (Figure 1-6) [51]. Receptor function refers to the ability of the solid surface to interact with target gas, i.e. oxygen adsorption, water vapor adsorption, and acid or basic properties of the surface. The transducer function in a sensor device belongs to the conversion of the signal produced by chemical

17

interaction into an electrical signal and depends on features such as carrier mobility, grain size, and doping. The utility factor shows the accessibility of inner oxide grains to the target gas and striking photons (i.e. thickness, pore size, and diffusion path). In the latter, if the rate of the reaction is much higher than the rate of the diffusion, then the gas molecules cannot utilize the inner grains, thus lowering the sensor efficiency [51].
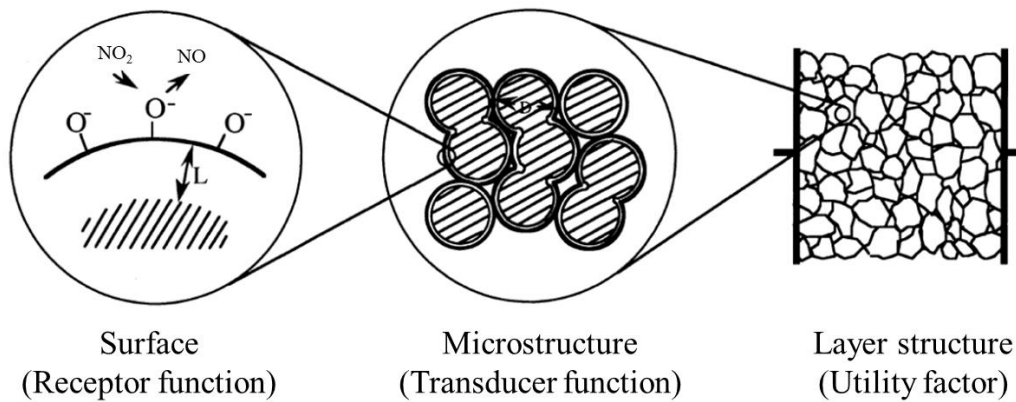
Figure 1-6: Schematic diagram of the receptor, transducer and the utility functions of a semiconducting metal-oxide layer (Reproduced from [52])

Therefore, the properties of semiconductors can be significantly changed by adding impurities (doping) into their crystal lattice, loading with noble metals, developing core-shells as well as mesoporous structures. By implementing any of the aforementioned modifications, the electrical behaviour and reactivity of the surface may vary significantly, which in turn affects the sensor interaction with the surrounding gas. Generally, medication of the surface properties is through increasing the concentration of reactants at the surface, lowering the activation energy of the surface reactions, and enhancing the charge density by reducing the charge recombination rate [16].

The logic of this approach mainly relies on the fact that the synergetic effects of material structure and composition are promising ways to achieve selective and sensitive gas detection.

1.6.3 Sensor geometry and design

The geometrical design of the sensor components contribute greatly to the sensor performance as the whole film must go through a conformal variation in conductivity upon exposure to the photons and the target gas [53]. Chemi-resistive high-temperature gas sensors typically consist of a thin or thick film sensing layer deposited over a back-heated substrate. Working under UV irradiation, however, dictates several important design considerations. A sufficient contact must be ensured among the photons, sensing layer and gas molecules so that maximum efficiency can be achieved. Another concern, especially in short wavelength UV, would be the interaction of light and gaseous components in the medium before reaching the surface. Thus, in order to have a high-performance gas sensor device, the implementation of a sensitive chemistry must be accompanied by optimization of the design features.

There are only a few studies in the open literature that have investigated the design of UV-LED activated sensor devices. Casals et al. [54] and Markiewicz et al. [55] recently reported a miniaturized device, which was a sensor architecture built around a miniaturized custom-made LED. This so-called micro light plate (μLP) configuration showed a minimum power consumption as low as $30\,\mu W$ due to high photon efficiency. Fabrication of custom UV-LED, however, may introduce more complexity to the sensor preparation process, is time consuming and requires advanced equipment.

Wang et al. [56] reported the first full-stack UV-LED activated sensor as shown in Figure 1-7. They integrated a thin layer of In_2O_3 nanoparticle on GaInN/GaN UV-LEDs. The short distance between the sensor and the light source (several hundreds of microns) may offer a significant improvement in photon efficiency and power consumption of the sensor.
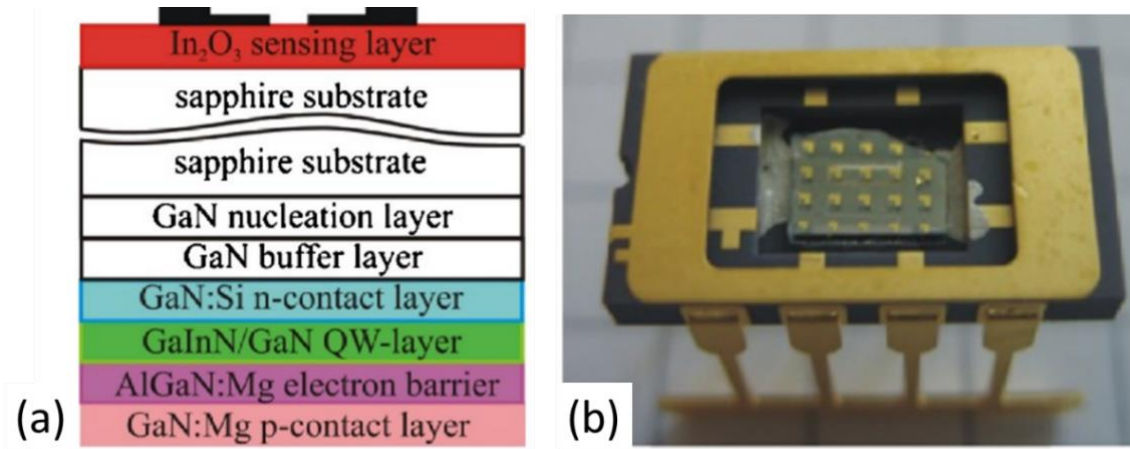
Figure 1-7: (a) Schematic cross section of the sensor integrated onto the a GaInN UV-LED chip (b) Images of the actual sensor inside a ceramic IC package [56]

Similar arrangements to the above sensor were reported by Yu et al. [57] and Hsu et al. [58], whereas the LED and the sensor films were mounted on top of a commercial LED. Gong et al. [59] also developed a design based on a hybrid structure of integrated ZnO nanowires on optical fiber surface, attached to a UV source.

There is still a need for innovative design and fabrication concepts that offer a true solution for large scale production, with good reproducibility and at a low cost using the methods and tools commonly available in microelectronic production facilities. A new basic design concept that can be implemented to improve the sensor performance and fabrication process, and broaden its applicability is the UV-LED integrated sensor network system (with backside-irradiation) which has been explained in the recommendations section (Chapter 8, Section 8.2).

1.7   Thesis objectives

Based on the concepts reviewed in the previous sections, and to meet the increasing need for high-performance gas sensors operating at ambient temperature, the main objective of this research was set to develop highly sensitive sensors with appropriate response time and to evaluate their performance using a model gas (i.e. NO_2). To meet the overall goal, and considering the inspiring works in UV-LED industry and nanotechnology, the main focus was directed toward influencing areas discussed in the previous section, and set the following sub-objectives:

1. Explore the effects of UV radiation parameters such as wavelength, irradiance and irradiation pattern (pulsation) on commonly utilized metal oxide semiconductors (i.e. ZnO, In_2O_3, SnO_2, and WO_3)

2. Investigate the possibility of enhancing electron utilization ratio through adding Ag metal into the lattice of a host semiconductor, such as ZnO.

3. Study the extent to which the sensitivity can be enhanced through utilizing 1D structures and Pt loading, based on the privileged performances of metal loaded nanowires in gas sensing applications, reported in the literature.

4. Apply core-shell structures and utilize the synergistic effects of the combined semiconductors on the sensing performance.

5. Utilize ordered mesoporous materials as supports for metal oxide semiconductors sensors and study the effect on the sensitivity.

1.8   Thesis outline

In this introduction chapter, metal oxide gas sensors in general, and the parameters affecting the performance of a typical gas sensor device have been discussed. A review article has been published in the *Critical Reviews in Solid State and Materials Sciences,* outlining the key parameters, recent advances, and future trends in photo-activated gas sensors.

Chapter 2 demonstrates the experimental setup designed and operated for testing the developed sensors and explains the fabrication process of sensor system components. Chapter 3 is dedicated to a parametric study on the effect of UV source specifications on four common semiconducting materials (Objective 1). The material presented in this chapter was published in the *Journal of Photochemistry and Photobiology A: Chemistry*. Chapter 4 introduces a highly sensitive gas sensor developed by the addition of Ag metal particles to the structural lattice of a ZnO semiconductor (Objective 2). Chapter 5 reports the preparation routes and photo-induced gas sensing performances of Pt loaded ZnO NWs (Objective 3). The studies presented in Chapters 4 and 5 are published in the *Journal of Electrochemical Society*. Chapter 6 discusses two core-shell sensors, ZnO-In$_2$O$_3$ and ZnO-SnO$_2$, and compares the performances versus monolithic sensing materials (Objective 4). This study will be submitted to the *Journal of Sensors and Actuators B: Chemical*. Chapter 7 describes the application of high surface area carbon mesoporous material as the support for the active sensing layer (Objective 5). This research work was submitted to *Journal of Sensors and Actuators B: Chemical*. In each chapter, different characterization methods have been used to analyze the physical and chemical properties of the prepared materials. Further, the gas sensor responses have been investigated and suitable conditions to obtain the optimal response characteristics have been reported. The main conclusions of this research work, and the recommendations for further investigations of key areas to improve sensor efficiency have been discussed in Chapter 8; where a new sensor platform design has also been proposed.

Chapter 2: **Experimental Apparatus**

2.1 Gas sensor setup

The sensor response measurements were performed by a laboratory-made experimental setup. A setup, shown in Figure 2-1 was designed to expose the sensor to the exact concentrations of the target gas, as well as to adjust the operating parameters involved in the sensing process, i.e. UV source parameters. In this setup, NO_2 was introduced to the semiconductor layer, which was enclosed in a stainless steel chamber, in the dark and under continuous UV irradiation generated by UV-LEDs. The experimental setup was made of three parts: gas delivery, chamber, and electronic section. Each sensing experiment was repeated at least two times to make sure that the data are reproducible. Images of the actual experimental setup have been presented in the Appendix A.1.
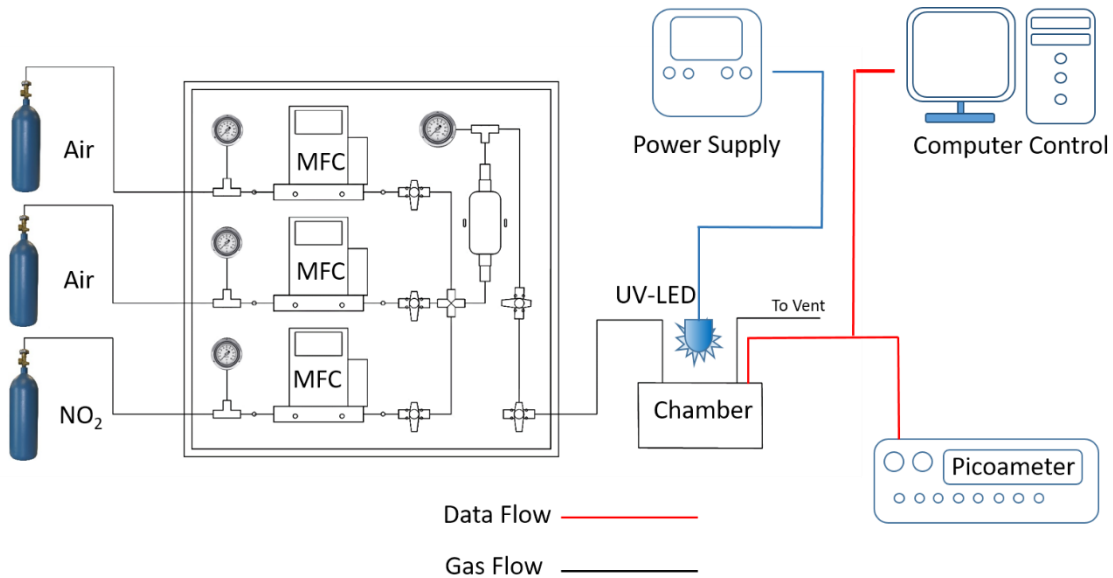
Figure 2-1 : Schematic view of the experimental setup for gas sensing measurements

2.1.1　Gas delivery

This section consists of several mass flow controllers (MFCs) to precisely measure and control the flow rates of target gases (Figure 2-2). The board adjusts the flow rates of different gases and mixes them at specific ratios to obtain the desired concentration. To thoroughly mix gases, a pressurized cylinder is accommodated just before the chamber, and a needle valve located by the exterior of the cylinder controls the inside pressure. Three safety pressure gauges are positioned just before the mass flow controllers to make sure of the flow and that the pressure is not exceeding the maximum allowable operating pressure of MFCs. The third pressure gauge mounted at the top of the pressurized cylinder determines and controls the pressure inside the cylinder.
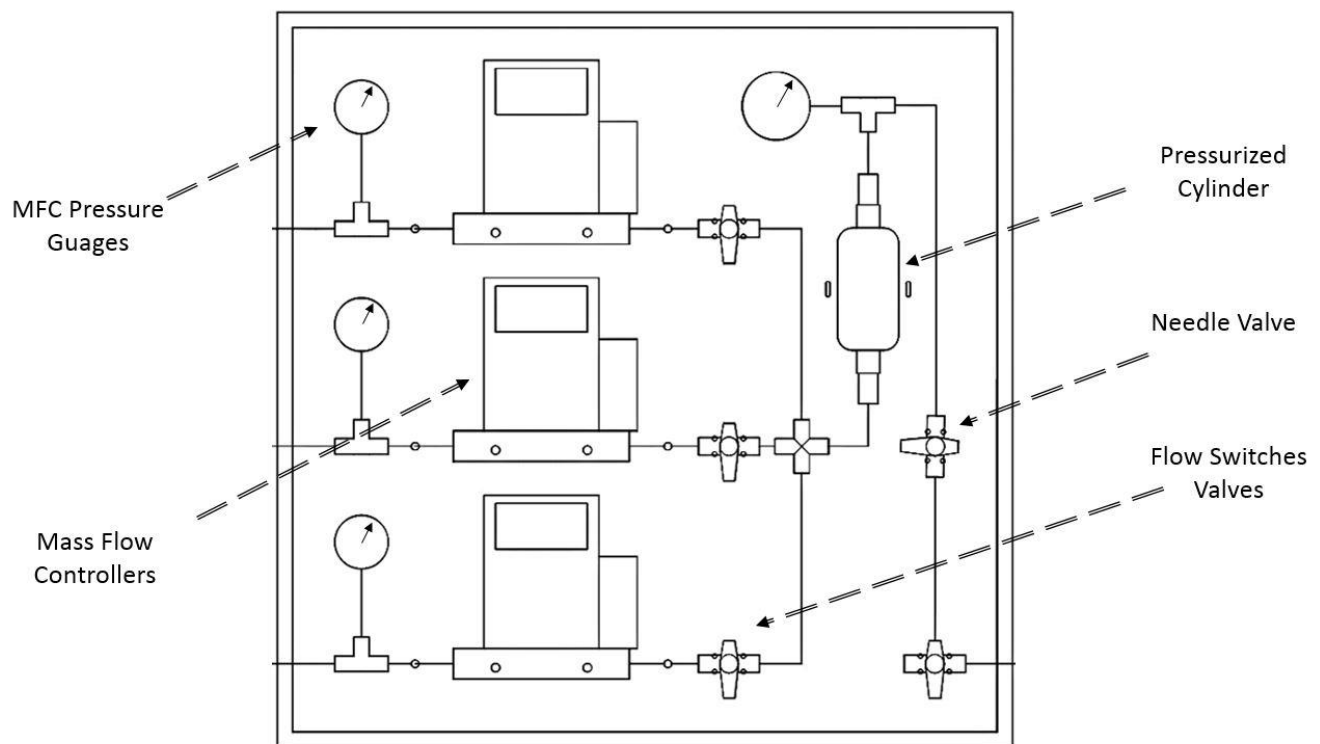
Figure 2-2: Details of channeling board implemented to produce low concentrations

2.1.2 Reaction chamber

The chamber where the sensing material, gas molecules, and photons meet is presented in Figure 2-3. The stainless steel gas-testing chamber is the house of the electrical connectors and wires and needs to be sealed. Chamber design is also very important to ensure that the whole surface, receives adequate irradiation from the UV source and is fully exposed to the transient gas.
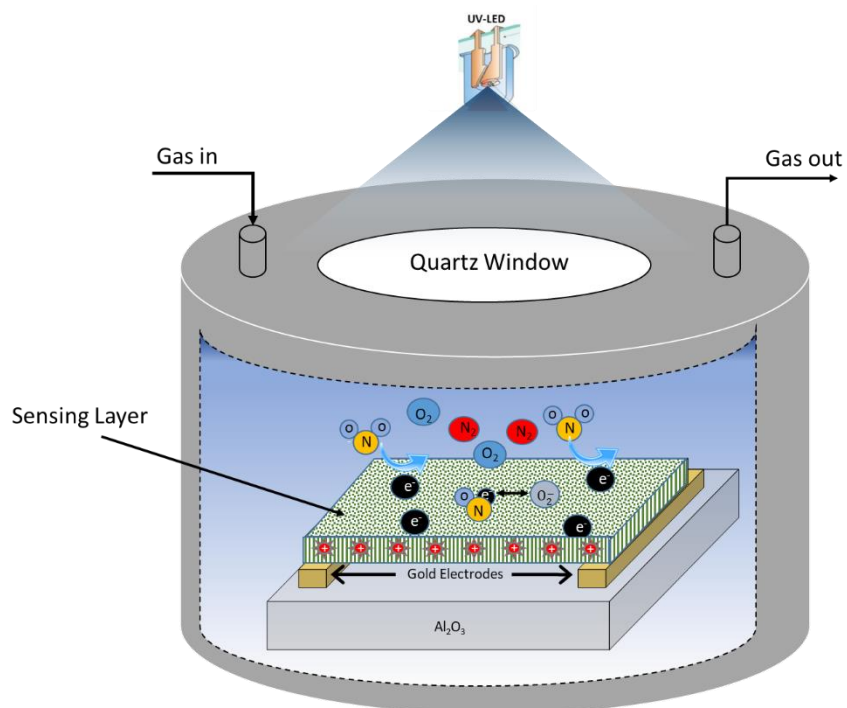
Figure 2-3: Schematic view of the reaction chamber used for sensing measurements

2.1.3 Data acquisition

The performances of the developed sensors were continuously monitored by a volt-amperometric technique in which the sensors were biased by 5 V and film resistance was measured over time. The electrical measurements were carried out using Keithley digital 6487 Voltage source picoameter. The designated built-in power source in the instrument makes a more accurate and more stable current. A

LabView program was developed to control the whole process remotely. Due to the small current flow in the circuit, standard insulate cables were used to connect sensor electrodes to the multimeter. Figure 2-4 shows a schematic illustration of the implemented electrical circuit.
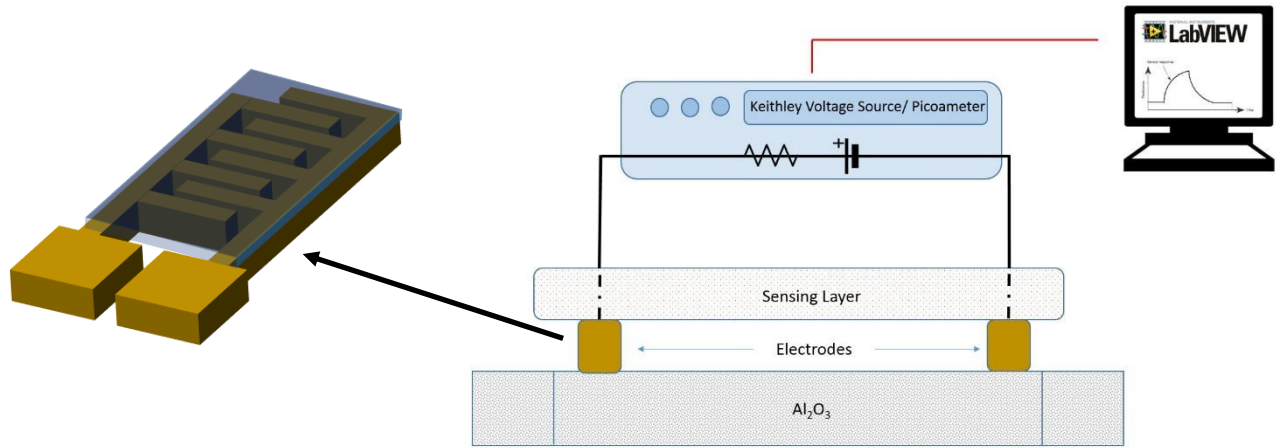
Figure 2-4: Electrical measurements in gas sensor setup

2.1.4   UV-LED

The use of recently developed UV-LEDs enables the optimization of the sensor output by controlling the irradiation parameters. The UV-LEDs that were used in this research have been shown in Table 2-1. The power of UV-LEDs was adjusted by controlling the operating current. The actual incident irradiances on the surface of the sensor were measured by Ocean Optics USB2000+ spectrometer equipped with a Sony ILX511B CCD detector.

The pulsed UV irradiation was generated by using a dual-channel arbitrary function generator (Instek AFG-2225). Although the temperatures of the UV-LED sources were controlled using a thermo-electric cooler (TEC) attached to a circular heatsink, they were also mounted outside a quartz window to avoid any unwanted interference of temperature changes.

Table 2-1:A summary of specifications of the UV-LEDs used in the research

Specification / Model	Manufacturer	Wavelength (nm)	Lens	Total Radiant Power (mW)	View Angle $2\theta\frac{1}{2}$ (°)	Appearance
-	Dowa Electronics	270	Flat	80	Collimated	
CUN6AF1B	Seoul Semiconductor	365	Flat	690	110	
CUN6AF4A	Seoul Semiconductor	365	Flat	2750	116	
NVSU233A	Nichia	385	Flat	1400	120	
NVSU233A	Nichia	405	Flat	1400	120	

2.2 Gas testing procedure

Before each test, the sensors were blown with dry purified air for 1 h at a constant flow rate of 100 mL/min to stabilize the sensors and to remove moisture or any adsorbed molecules from the surface. The sensors were then biased by 5V and exposed to the target gas for a limited time (to reach a plateau value in resistance). They were then recovered by exposure to purified air until the resistance returned to its initial value. In this report, the sensor response indicates the maximum change in relative resistance of thin films at different conditions. It is defined as $R_{ox} = \frac{|R_g - R_a|}{R_a}$ or $R_{re} = \frac{|G_g - G_a|}{G_a}$, where R_a/G_a, and R_g/G_g are the electrical resistance/conductance of the sensor measured in the presence of pure dry air and target gas, respectively. The response time (τ_1) and recovery time (τ_2) are defined as the time that takes for the sensor resistance to change from 10% to 90% of its total variation.

2.3   Fabrication process

2.3.1   Electrode deposition

For the electrical measurements, a thin layer of gold was deposited over a ceramic sheet through an interdigitated comb shape shadow mask. The shadow mask was initially designed in AutoCAD and built using laser micromachining. Prior to any deposition, the substrates were cleaned by oxygen ion bombardment using Plasma-Enhanced Chemical Vapor Deposition (PECVD) to improve the adhesion of the film to the substrate by removing moisture and any organic contaminants on the surface.

For the deposition, E-Beam Physical Vapour Deposition (EBPVD) method was selected. The 2000 e-beam evaporator system (located in UBC Nano-Micro Fabrication Cleanroom) was used to deposit the electrode materials. The setup consists of a control cabinet, chamber, electron-beam power supply, cryo-pump compressor, and mechanical vacuum pump. The control cabinet houses a microprocessor, operation control panel, thermocouples gauges and controllers, film thickness monitor, CTI cryo-pump temperature monitor and electron beam control module.

In the physical vapor e-beam deposition method, target anode is bombarded with huge numbers of high energy electrons given off by a charged tungsten filament under a high vacuum. The electron beam causes atoms to transfer from the target into the gaseous phase. These atoms precipitate into solid form, coating everything inside the vacuum chamber with a thin layer of the anode material. Multiple types of materials can be used simultaneously in a single EBPVD system in designated source areas. Figure 2-5 shows the e-beam process as well as the actual e-beam setup.
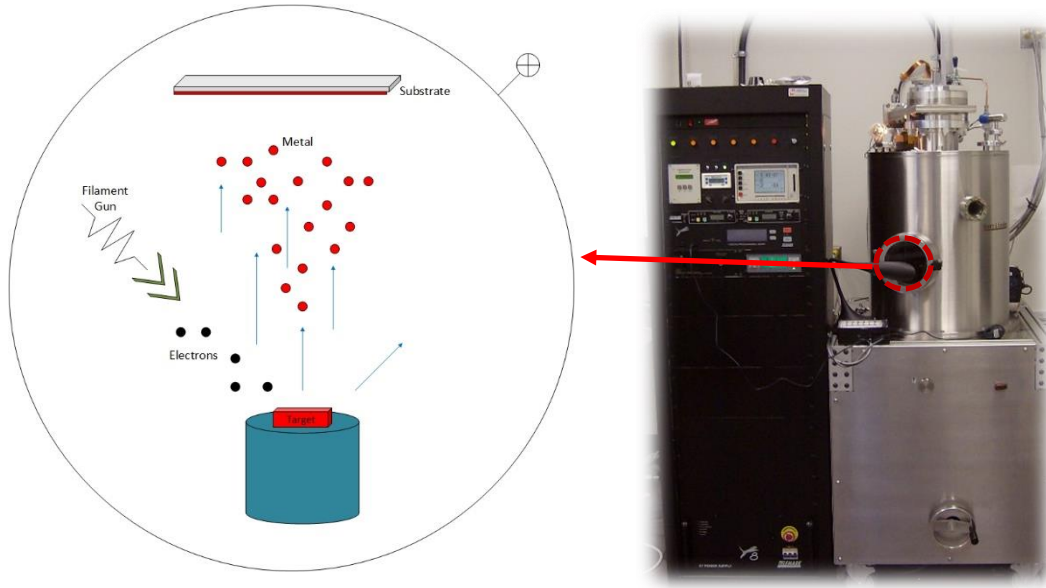
Figure 2-5: A schematic illustration of the electron beam physical vapor deposition technique (left), and the DeeDirectors electron beam evaporator used in the cleanroom (right)

In this study, a thin layer of titanium with a thickness of 25 nm was firstly deposited to enhance the stability and adhesion strength of the gold materials. Then, gold thin layer (~400 nm) were deposited over titanium using a pure gold target source. All thickness measurements were certified by ex-situ characterization using ALPHA STEP 200 Profilometer. The width, spacing, and length of the deposited first electrode design are shown in Figure 2-6a. Figure 2-6b shows, a new electrode pattern that was designed and prepared with a lithography technique for miniaturized applications.
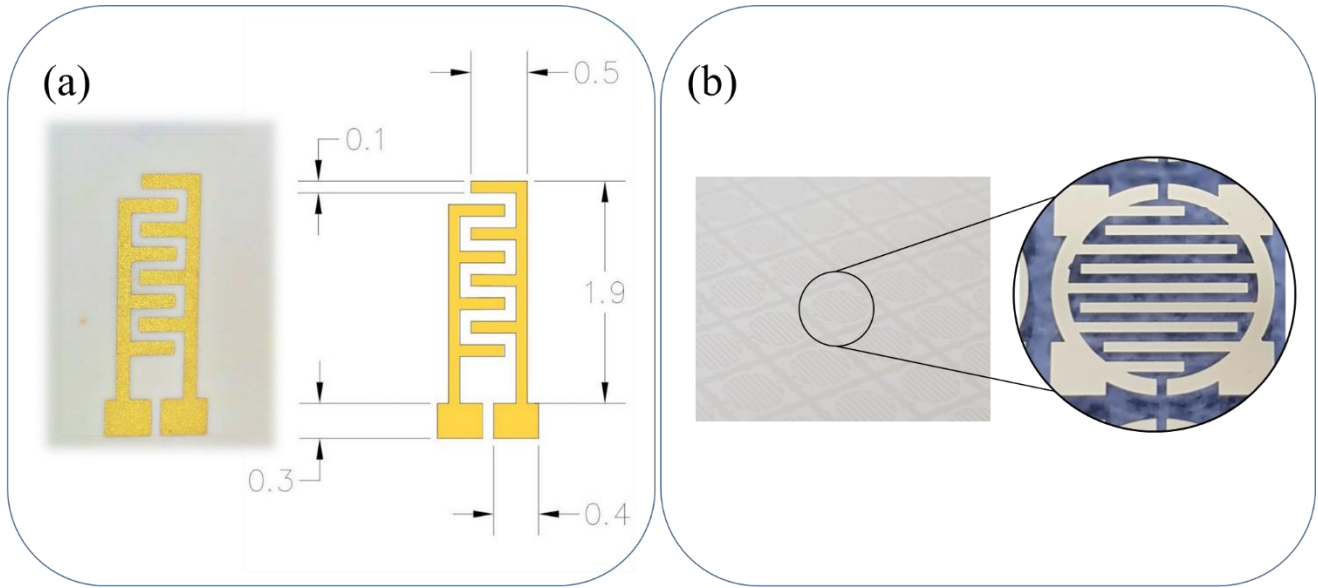
Figure 2-6: The dimensions of fabricated interdigitated electrodes a) first electrode design for lab experiments with dimensions (in centimeters) b) second design for miniaturized devices (the dimensions are 5mm×5mm)

2.3.2 Material deposition

Sensing materials were deposited using spin-coating method or direct growth. Initially, a known amount of solution (5 ml) was taken by a pipet and poured dropwise over the substrate while rotating at 800 rpm. Then, the rotating speed was set to 2000 rpm to dry the layer in each stage of development. This process was repeated 10 times, followed by a 3 min heating at 80 °C in the middle of the coating to let the trapped water evaporate, followed by high-temperature calcination. Figure 2-7 and Figure 2-8 show the deposition and synthesis process of the prepared semiconductor layers, respectively.
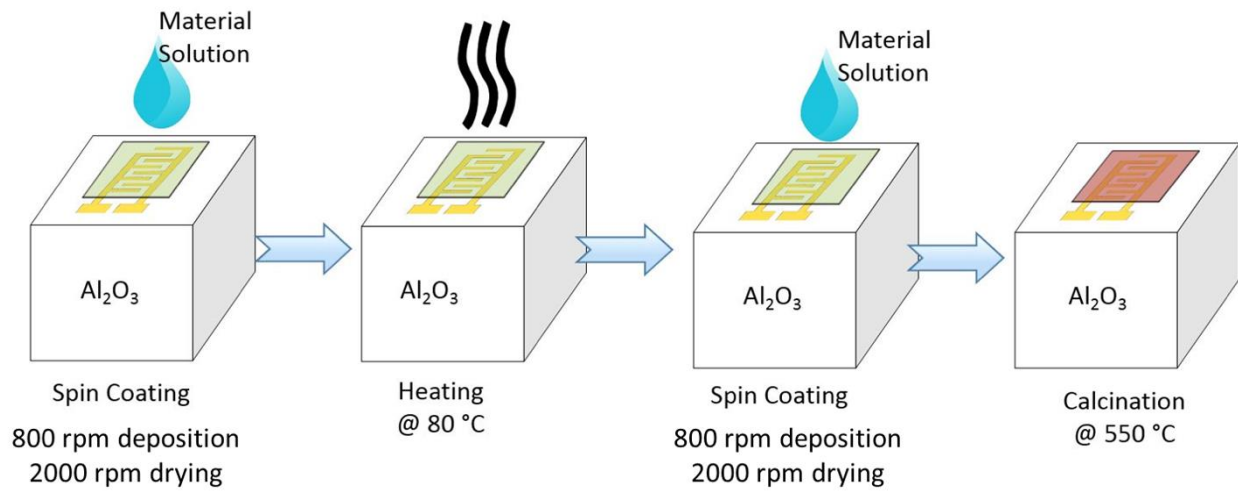
Figure 2-7: The consecutive steps in sensing layer deposition process
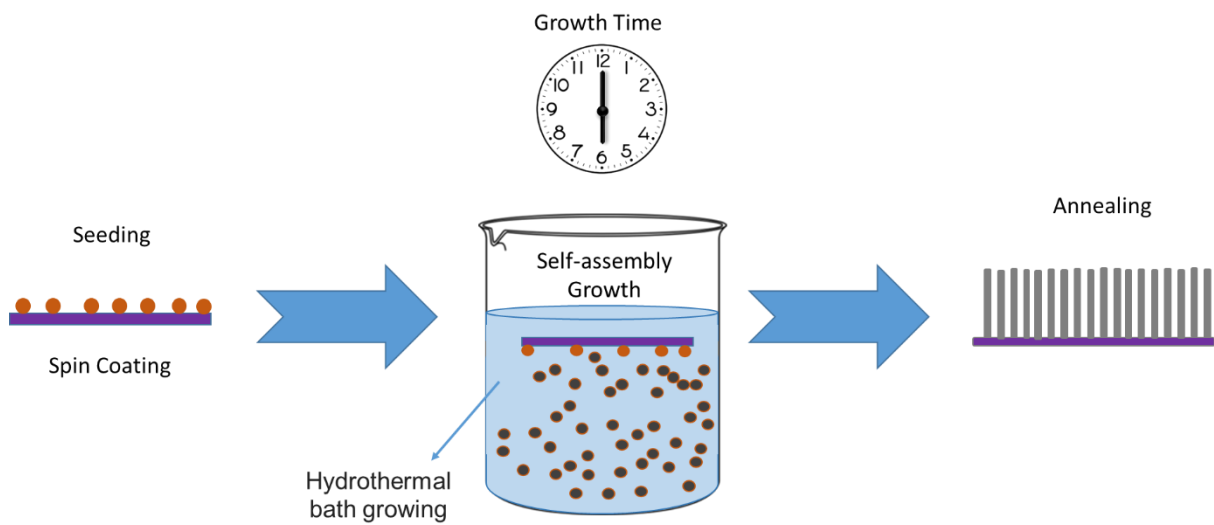
Figure 2-8: The steps to prepare ZnO NWs using self- assembly chemical bath growth at 93 °C

2.4   Characterization

To investigate the morphology, particle size and nano-structure of compounds on the surface, scanning electron microscopy (SEM) has been performed. The FEI Helios NanoLab 650 dual beam SEM machine was employed to perform high-resolution imaging and nano-structure analysis.

In order to investigate the surface topography, the composition of the prepared sensor layers and surface elements, X-ray photoelectron spectroscopy (XPS) was performed. Energy-dispersive X-ray (EDX) spectroscopy was utilized to characterize the chemical composition as well as to measure elemental containments. The crystal structure of prepared samples and the atomic structure diffraction patterns were obtained in X-ray Diffraction (XRD) analysis. The structural properties were investigated by 2θ method of XRD with a Cu Kα1 ($\lambda = 0.15406$ - $\lambda = 0.154439$nm) source at 40 kV and 40 mA.

Finally, to certify the UV wavelengths used in the experiments as well as the photo-reduction behaviour of prepared sensors, UV-Visible spectroscopy was carried out by Ocean Optics USB2000+ spectrometer equipped with a Sony ILX511B CCD detector.

Chapter 3: **The effect of radiation parameters on the performance of photo-activated gas sensors**

3.1 Introduction

Several studies in the literature have employed photonic energy with different specifications to promote surface reactions at lower temperatures [23,60,61]. These room temperature sensors are in high demand for the Internet of Things (IoT) applications. Among the groups of metal oxides, ZnO [62–65], In_2O_3 [66–68], SnO_2 [69–71], and WO_3 [39,72,73] have been extensively investigated for photo-activated operation because of their high electron conductivity features.

In terms of activation wavelength, it has been shown that a wavelength-resonant excitation can maximize the photo-response [22]. In other words, the maximum response corresponds to the photons with energies close to the bandgap of the sensing material, which is mainly around 3 electron-volts (eV). Therefore, radiation sources with similar energies, which lie in the ultraviolet region (≤ 400 nm), are the most promising candidates to activate the aforementioned semiconducting materials. Ultraviolet (UV) radiation can be produced by using recently emerged ultraviolet light-emitting diodes (UV-LED) that not only provide the opportunity to fully control operating parameters but also significantly reduce the energy consumption in photo-activated gas sensors. The developments of UV-LED based chemi-resistive sensors have been discussed in a comprehensive review [12].

While the effect of UV irradiation specifications on the surface reaction kinetics and sensor responses have generally been accepted, the correlation between these parameters and the sensor signal has not been compared. Therefore, it is necessary to investigate the performance characteristics of commonly used sensors under various operational conditions to better specify the functionality of any given semiconductor material in practical applications.

In this study, the sensing performances of four different sensing materials in various irradiation conditions, such as different irradiation wavelengths, irradiances, and irradiation patterns, at room temperature were characterized. Moreover, we determined the optimal operating conditions to achieve the highest sensor response with the shortest response time and complete sensing recovery. The as-fabricated ZnO, In_2O_3, SnO_2, and WO_3 nano-structures were examined to detect low concentrations of NO_2 as a model gas contaminant. NO_2 was selected because it greatly contributes to environmental and human health problems, and there are still some challenges associated with its detection using traditional techniques.

3.2 Material preparation

All chemicals used were of analytical grade and purchased from Sigma-Aldrich Canada Corporation.

Preparation of ZnO: Zinc nitrate hexahydrate $(Zn(NO_3)_2.6H_2O)$ and 2.0 M ammonia (NH_3) solution in ethanol (CH_3CH_2OH) were used as source materials. 0.89 gr of zinc nitrate powder was dissolved in 100 mL of a solution containing 85% ethanol and 15% methanol. The solution was vigorously stirred for 30 min at 50 °C in a water bath under a fume hood. Drops of the ammonia solution were then added to zinc-containing solutions at a speed of 1 drop/s at the same temperature while measuring the pH value continuously to reach pH $\geq$ 9. The solution was then stirred for 4 h and slowly cooled to room temperature. The resulting precipitates were washed, centrifuged, and calcined at 550 °C for 2 h.

Preparation of In_2O_3: Indium nitrate hydrate $(In(NO_3)_3.xH_2O)$ and 2.0 M ammonia (NH_3) solution in ethanol (CH_3CH_2OH) were used as precursors. In a typical synthesis process, 0.9 gr of indium nitrate hydrate was prepared in 100 mL of a solution containing 85% ethanol and 15% methanol at 50 °C. The solution was then stirred for 30 min at 50 °C to fully mix the dissolved material. Then, the reducing agent

was added dropwise to the solution until reaching pH $\geq$ 9. The precipitates were then collected by centrifugation and calcined at 550 °C for 2 h.

Preparation of WO₃: WO$_3$ was synthesized by precipitation technique using solutions of ammonium (para) tungstate hydrate ($H_{40}N_{10}O_{42}W_{12}$-xH_2O) and nitric acid (HNO_3). In this process, 60 mL of 10 mM ammonium tungstate solution was prepared in deionized water and stirred at 80 °C for 15 min. Then, 40 mL of 2.5 mM nitric acid solution was added dropwise to the tungstate solution under vigorous stirring at the same temperature. The obtained solution was aged for 60 min to precipitate the synthesized material. The resulting precipitates were centrifuged, washed several times, and dried at 80 oC for 4 h. Finally, the WO$_3$ powders were ground and calcined at 550 oC for 2 h.

Preparation of SnO₂: The synthesis was carried out using $SnCl_2$ and NaOH as precursors. In a typical synthesis process, 0.05 M of $SnCl_2$ solution was prepared in 50 mL of deionized water. Under vigorous stirring, 0.5 M of NaOH solution, prepared in 50 mL of deionized water, was added dropwise to the $SnCl_2$ solution until reaching pH $\geq$ 9. The solution was then put into a microwave oven and treated at a power of 300 W for 20 min. The solution was aged to cool down to room temperature, and the resulting precipitates were washed with distilled water, dried at 80 °C for 24 h, and calcined at 400 °C for 2 h.

Sensor fabrication: For the material deposition, 5 mL of the solution was taken using a pipette and poured dropwise over the substrate while rotating at 800 rpm. Then, the rotating speed was set to 2000 rpm to dry the layer in each stage of development. This process was repeated 10 times followed by 3 min of heating at 80 °C in the middle of the coating to let the trapped water evaporate. The material synthesis and sensing layer deposition of all semiconductors were performed simultaneously to avoid any possible changes in conditions that may affect the fabricated sensors.

3.3   Results and discussion

3.3.1   Morphology and crystal structure

Figure 3-1a represents the morphology of the ZnO sample, showing randomly oriented ZnO particles in variable lengths. The FE-SEM images more or less confirm agglomerated ZnO particles with distinct boundaries with an average grain size of about 40 nm. The representative SEM photographs of In_2O_3 nano-particulates (In_2O_3 clusters) are presented in Figure 3-1b. Compared to the ZnO film, the surface of the In_2O_3 film was much smoother with possibly smaller crystallites and mostly without distinguishable grain boundaries. The average grain size of In_2O_3 particles is estimated to be 25–35 nm. As shown in Figure 3-1c, the SnO_2 nanoparticles formed a uniform structure of hollow spheres with a diameter of approximately 15 nm. The morphology of the nano-sized WO_3 particles, presented in Figure 3-1d, is mainly in pseudo-spherical shapes, and the average particle size is approximately 60 nm.

Improved gas-sensing properties can be achieved at high surface-to-volume ratios. A large number of grains, which is more likely when grains are small, will result in high porosity and a large surface area for effective adsorption of gas species. In contrast, the agglomeration of minimal nanoparticles prevents gas molecules from accessing the internal surface. Hence, the morphologies of the prepared materials, especially ZnO and In_2O_3, suggest that the sensing layers have grain features suitable for gas sensing.
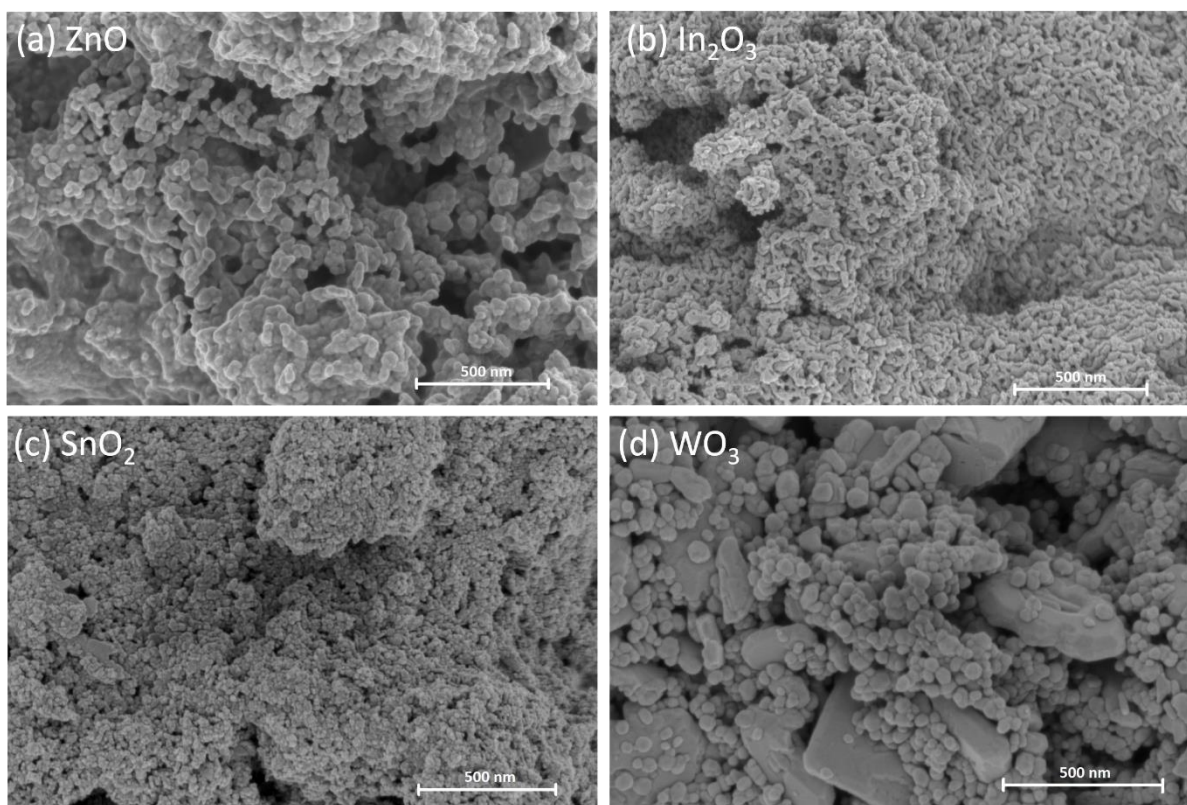
Figure 3-1: FE-SEM images of prepared materials, (a) ZnO (b) In_2O_3 (c) SnO_2 (d) WO_3 nano-particles

XRD analysis was performed to analyze the material structure and crystallinity (Figure 3-2). The XRD pattern of nano-sized ZnO particles is shown in Figure 3-2a. The crystalline planes located at 31.76, 34.42, and 36.25 represent preferably (100), (002), and (101) crystalline shapes of hexagonal ZnO, respectively, and address wurtzite phases (JCPDS no. 36-1451). For the In_2O_3 nano-particles, the peaks in the XRD analysis are attributed to the cubic structure of In_2O_3 with JCPDS no. 06-0416 (Figure 3-2b). Using the Scherrer equation, the average crystallite sizes of the ZnO and In_2O_3 samples are 34 nm and 12 nm, respectively. As shown in Figure 3-2c, all diffraction peaks of SnO_2 in the XRD pattern, which coincide well with JCPDS file no. 41-1445, can be indexed to the rutile phase. The average crystallite size of the SnO_2 deduced from Debye Sherrer's equation is calculated at 10 nm.

For the WO$_3$ sample, the sharp and intensive peaks of the XRD pattern indicate a highly crystalline structure (Figure 3-2d), where the corresponding crystal planes are shown (JCPDS no. 43-1035) with an average crystallite size of 53 nm. The absence of impurity diffraction peaks in the XRD patterns represents the existence of pure phases in the synthesized materials. The predominant orientation of the active surface affects the energy of the adsorption/desorption processes, and consequently, changes the response characteristics.
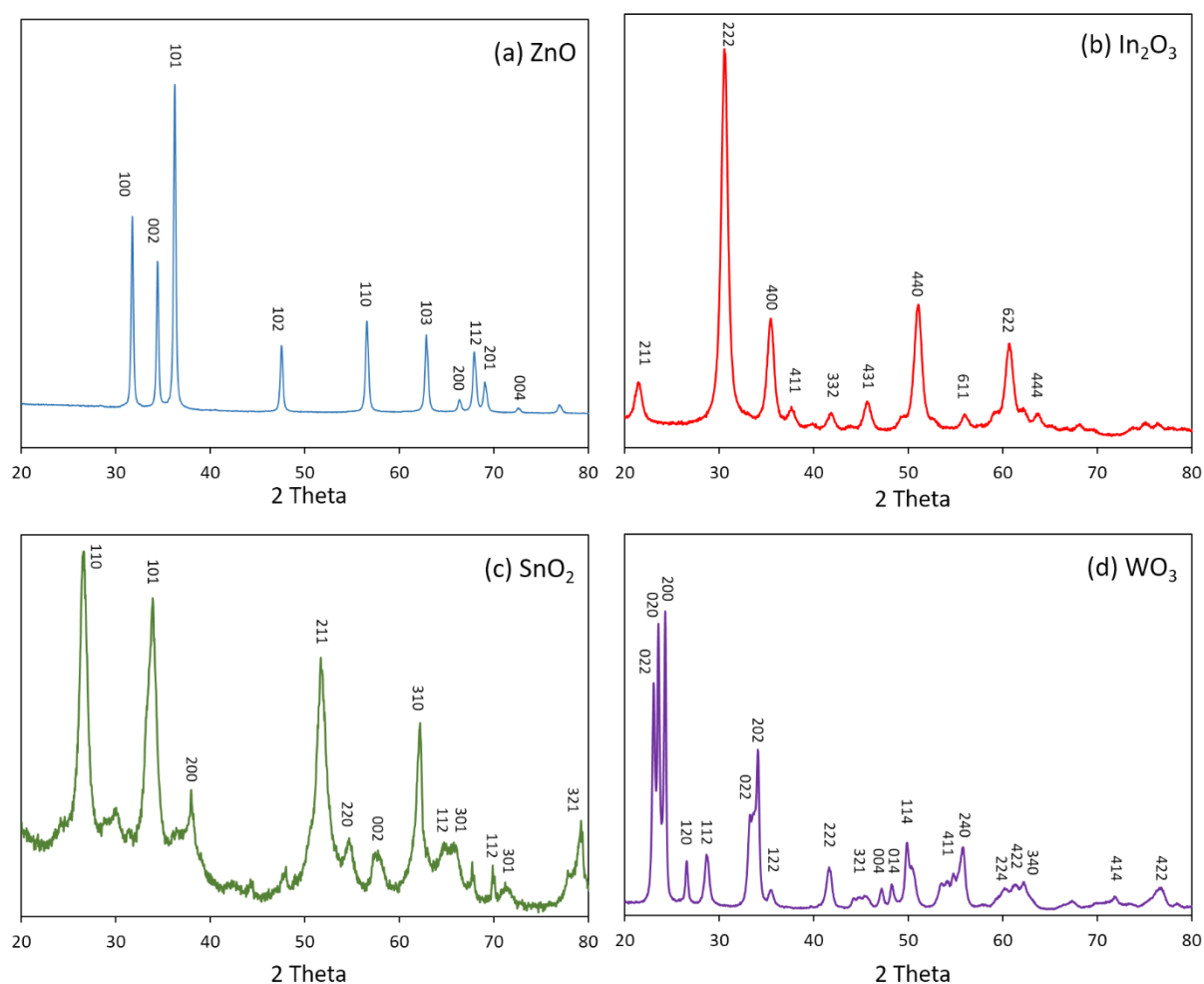
Figure 3-2: XRD plot of the (a) ZnO, showing well-crystalline wurtzite phase, and (b) In$_2$O$_3$, showing cubic structure, (c) SnO$_2$, showing rutile phase (d) WO$_3$, monoclinic

3.3.2 Optical properties of sensing materials

Optical analysis of thin films is a useful method to understand their quality, thickness, and material properties, such as band-gap and dielectric constants. In this analysis, the reflectance/absorbance spectra are investigated in the 200–900 nm spectral range. These data are confirmed through various repetitions. In optical measurements, photons from the light source irradiate the surface from a small opening nearly opposite to the sample port, illuminating the sample evenly. The reflected light gets scattered around the stage and is precisely sampled by an optical fiber at the connector.

The Kubelka-Munk theory is used to theoretically estimate the absorbance of thin films from the acquired diffuse reflectance measurements [74]. In this method, the band-gap energies are determined using Kubelka–Munk function:

$$F(R) = \frac{(1-R)^2}{2R} \qquad (12)$$

where (R) is the absolute percentage value of reflectance and $F(R)$ is equivalent to the absorption coefficient. The band-gap analysis was performed for the as-prepared materials using Tauc plot, as shown in Figure 3-3. The calculation procedure for determining band-gap is explained elsewhere [74]. The band-gap of the materials are estimated by plotting $[F(R) \cdot h\nu]^m$ vs. $h\nu$ (eV). The linear part of the Tauc plot is extrapolated to $[F(R) \cdot h\nu]^m = 0$ to get the band gap energy, while the point of inflection is found by taking the first derivative of the curve. If the plot of $(F(R) \cdot h\nu)^{(m=1/2)}$ vs. $h\nu$ gives a straight line, it is indirect bandgap material, and if a plot of $(F(R) \cdot h\nu)^{(m=2)}$ vs. $h\nu$ yields a straight line, it is a direct bandgap material. For the synthesized materials, the appropriate m values in the Tauc function have been used.

The ZnO band gap was estimated to be 3.2 eV while the In_2O_3 band gap was 3.42 eV, both in positive agreement with those reported in the literature [75,76]. The band-gaps of SnO_2 and WO_3 were estimated

to be 3.35 eV and 2.95 eV, respectively. According to the UV-Vis analysis, the sensing materials used in this research reflect light mainly at wavelengths above 400 nm. This confirms that the energy of the photons that reach the surface at wavelengths below 400 nm (UV region) is enough for complete absorption and to excite valence band electrons of the layer.
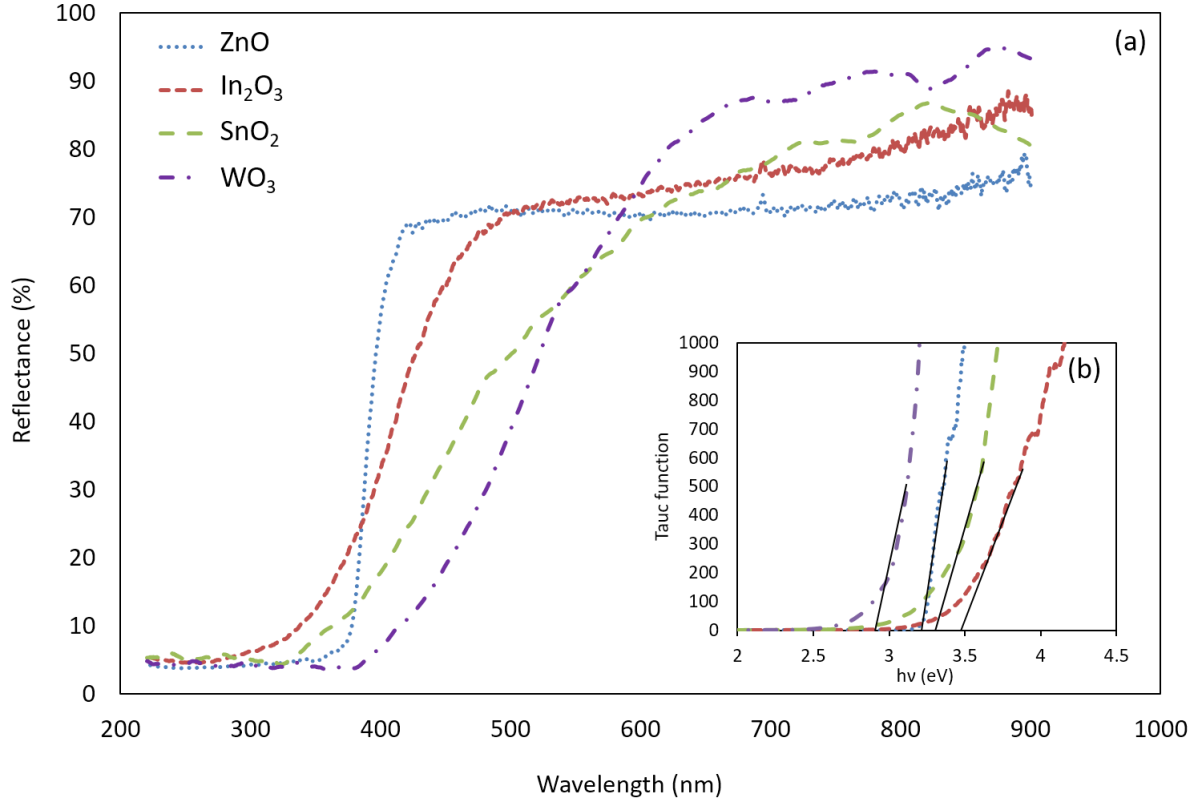
Figure 3-3: UV-Vis spectra of samples prepared by spin coating method (a) Reflectance spectra, (b) Tauc plot for band-gap determination

3.3.3 Photo-response of the fabricated sensors

To evaluate the photo-induced behavior, the time-dependent UV response of the prepared chemi-resistive sensors was studied. As shown in Figure 3-4, the sensing layers yield a significant photocurrent under periodic illumination (resistance decreases). A switching behavior, which is the photocurrent

increase under illumination and decrease in a dark environment, is clearly observed. The decrease change in resistance upon irradiation occurs in a relatively short time, while the recovery time in dark conditions takes longer. Such a slow recovery is attributed to the trapping centers, which are formed due to the materials' inhomogeneity, that prevent charge-carrier recombination [77]. Similarly, the fast response can be attributed to the rapid change in carrier concentration.

During the multiple illumination cycles for ZnO, In_2O_3, and SnO_2, the photocurrent responds similarly to the incident light with no significant variations in the signal amplitude. However, for the WO_3, both the dark and the illuminated resistance levels increase after repeated exposure. This behavior of WO_3, along with the low responsivity (Table 1), confirm the creation of radiation-induced disorders in the material structure. The unrecoverable resistance value in the dark that occurs following the first exposure to irradiation has been reported previously [23]. This behavior can be attributed to structural defects in the lattice, which are induced by illumination.

The resistance variations before and after the first UV illumination can represent the intra-layer specifications of the prepared sensors. For example, the observed initial dark resistance for In_2O_3 is lower than those of the other sensors, indicating that the In_2O_3 homo-nanostructure interfaces are not highly resistive. The lower resistance can be attributed to the higher mobility of valence electrons throughout the material, as a consequence of more oxygen ion vacant sites[78].

The resistance variation in the air upon UV radiation is attributed to the radiation-dependent oxygen ion chemisorption. It is generally accepted that oxygen is chemisorbed on oxygen vacant sites in the form of an ionized oxygen atom or molecule. This oxygen adsorption reduces the surface free electrons and results in higher base resistance. In other words, the higher charge mobility of In_2O_3 provides a better inventory of adsorbed oxygen, even in dark conditions. Hence, upon the initial UV exposure, the changes in resistance (ΔR_a°) for In_2O_3 are much smaller than those of other sensors, as the number of charge

carriers is not significantly affected by irradiation. On the other hand, irradiation excites a significant number of electrons in other metal oxide sensing layers and considerably increases the oxygen ions' surface occupancy.
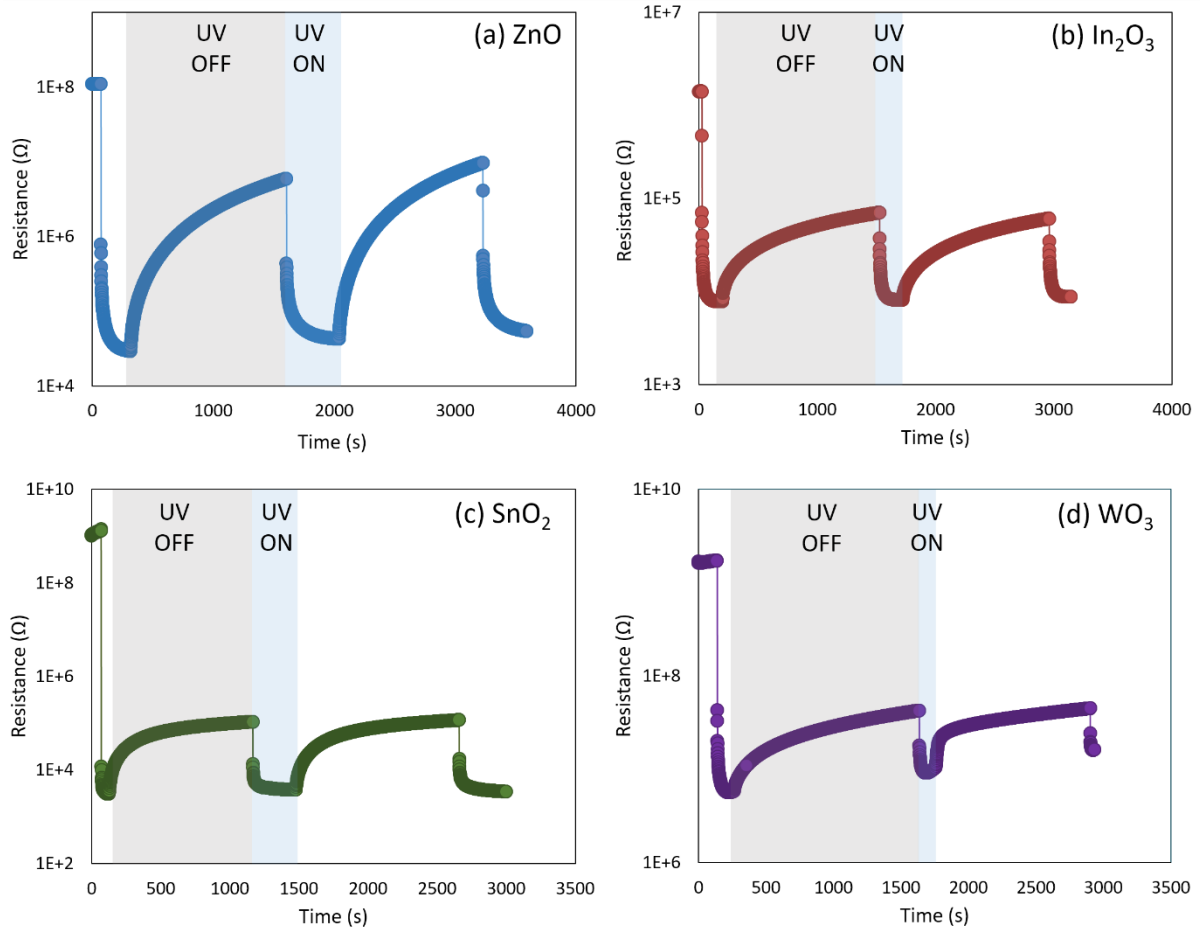
Figure 3-4: Time-dependent resistivity measured at 5 V bias, showing photo-response upon 365 nm UV-LED ON/OFF illumination (25 mW/cm^2 irradiance) (a) ZnO (b) In$_2$O$_3$ (c) SnO$_2$ (d) WO$_3$

3.3.4 UV activated gas sensing performance

3.3.4.1 Effect of irradiance

For proper sensing performance in UV-based gas sensors, exposure to the right irradiance for a sufficient amount of time is required. Irradiance is defined as the rate of photons striking the surface of objects per unit area. It is dependent upon the intensity and distance of the radiation source and mostly affects the gas adsorption/desorption processes, resulting in higher/lower reaction rates. An appropriate irradiance is one in which the sensor provides a high response, complete recovery, and reasonable response time. Selectivity can also be taken into consideration to determine the best operating irradiance. Optimal irradiance indicates that the equilibrium state of diffusion/adsorption of the gas molecules as well as subsequent reaction/desorption processes in the sensing layers, are fast enough and have adequate surface coverage percentages.

Figure 3-5 shows the effect of irradiance on the sensors' responses. At constant photon energy with a 365 nm wavelength (3.39 eV), increasing irradiance enhances the photo-desorption rates of adsorbed components and reduces the sensor response. In a high irradiance condition, equilibrium reactions shift toward producing more gas-phase oxygen and desorbing more target gas molecules, leading to lower resistance variation and a lower response. However, the reaction kinetics become faster with increasing irradiance, leading to faster responses and shorter recovery times.

The optimal irradiance within the experimented range for ZnO to achieve the highest response signal and shortest response time while completely recovering was 25 mW/cm^2. Please note that ZnO showed almost similar responses in 8 and 25 mW/cm^2. However, the response and recovery time constants under 25 mW/cm^2 irradiance were faster and more stable than that of 8 mW/cm^2. In contrast, In$_2$O$_3$, SnO$_2$, and WO$_3$ responses failed to recover completely at irradiances lower than 65 mW/cm^2. For instance, the unstable response for In$_2$O$_3$ sensor can be found in the Appendix A.2 (Figure A2-1). The appropriate

light irradiance for the In_2O_3, SnO_2, and WO_3 sensors was estimated to be 65 mW/cm^2, which gives a reasonable response time while having a stable sensor response. Optimal irradiance is highly dependent on layer specifications and is subject to change for any other target gases.

The response time (τ_1) values for each sensor material varies with working irradiance. For ZnO samples, the range of response time variations was observed to be from 166s at 251 mW/cm^2 to 197s at 8 mW/cm^2 while the complete recovery was observed for all irradiances. For In_2O_3 sensing material, the response time varied from 254 s at 251 mW/cm^2 to 300 s at 65 mW/cm^2. All ZnO recovery time values (τ_2) were around 300 s approximately, while for In_2O_3 sensors, the shortest τ_2 was observed to be 480 s at 251 mW/cm^2. By decreasing the irradiance to 65 mW/cm^2, τ_2 increased slightly to 500 s, and then the slop of changes increased significantly.

The observed response time for WO_3 to 5 ppm NO_2 under 8 mW/cm^2 was over 40 min, and decreased to about 20 min under 251 mW/cm^2 irradiance. SnO_2 showed similar response time at 251 mW/cm^2 irradiance, but the response was not stable at low irradiances. The recovery time for SnO_2 and WO_3 was around 30 mins at 65 mW/cm^2.
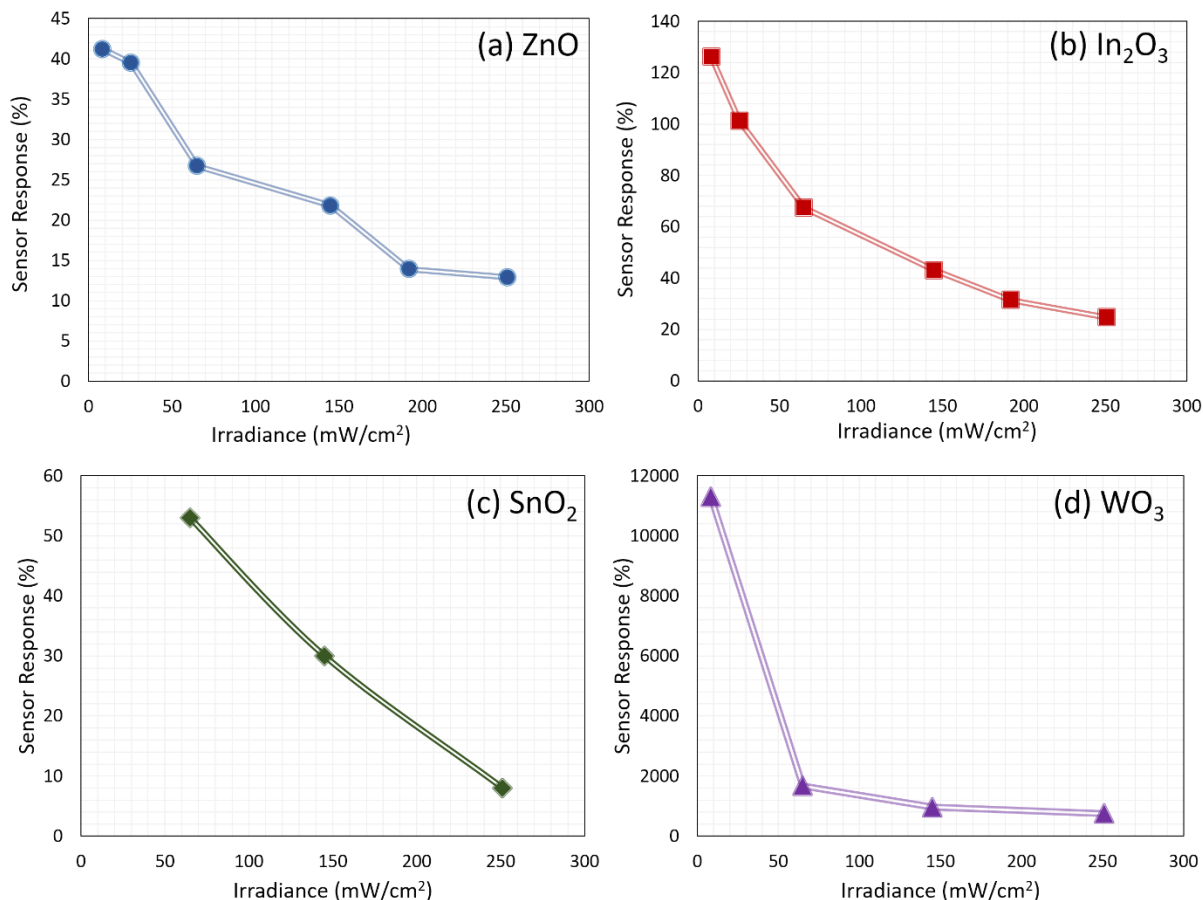
Figure 3-5: Sensors responses to 5 ppm NO$_2$ under 365 nm UV-LED irradiation at different irradiances

A representation of the sensing performance of prepared sensors to 5 ppm NO$_2$ under 365 nm UV-LED irradiation at values around their optimal irradiance is presented in Figure 3-6. The differences in sensor responses to NO$_2$ can be explained based on the number of active sites that are available on the surface. When the photons strike the semiconductor nano-particulates, a part of the grain will be depleted upon electron excitation. If the grain size is comparable to the depletion region (i.e., smaller than twice the depletion region), a significant portion of the grain will be depleted. Thus, when the conduction path of the electrons is narrower, large rapid variations in sensor responses will occur [52]. The homo-interfaces between particles (i.e., ZnO–ZnO, In$_2$O$_3$–In$_2$O$_3$, SnO$_2$–SnO$_2$, and WO$_3$–WO$_3$ interfaces) and the grain boundary potentials (double Schottky barrier) can play a determining role in the amount of

45

successful electrons/holes that can reach the surface. Therefore, the size of the particles, the thickness of the depletion layer, and the interface barriers significantly influence the electron/hole path to the surface and affect the sensing response.
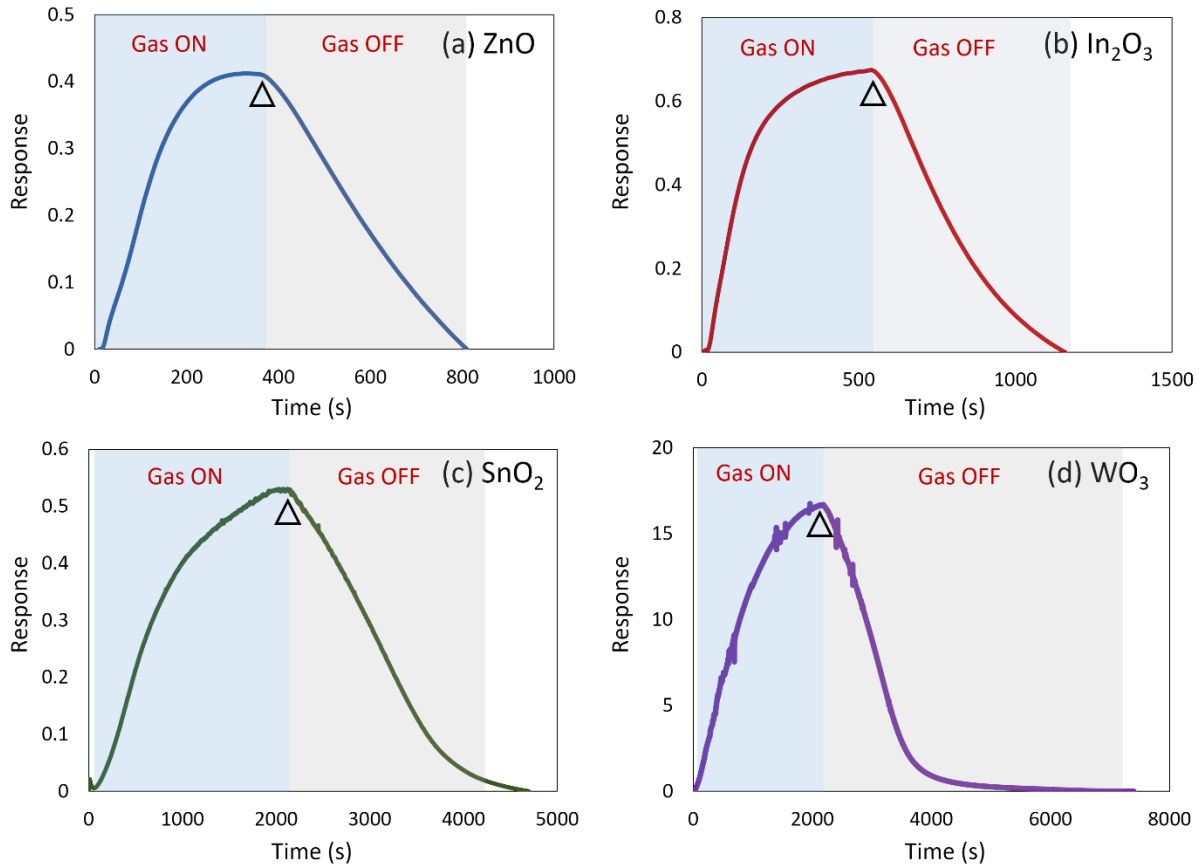
Figure 3-6: Typical response of prepared sensors towards 5 ppm NO_2 at their appropriate irradiances (a) ZnO (at 8 mW/cm^2), (b) In_2O_3 (at 65 mW/cm^2) (c) SnO_2 (at 65 mW/cm^2), (d) WO_3 (at 65 mW/cm^2). The NO_2 gas flow started at time near zero and stopped at t=Δ

3.3.4.2 Effect of wavelength

Separation of the charge carriers is necessary for a sensing application as it proceeds surface electrochemical reactions. The energy of the photons that reach the surface must be high enough to excite valence electrons. The sensing layer can also be activated when photons with lesser energies irradiate the surface. The latter may occur through several mechanisms such as indirect band-gap, disturbed crystal

46

structures or defect states on the surface, and multi-photon excitation [28]. Thus, in UV-Vis analysis, the reflectance signal starts decreasing in visible light or even infra-red regions. However, in this case, the number of generated charge carriers would be far less than that of using radiation in the UV region. As discussed previously, the maximum response is achieved when photons with the same energy as that of the band-gap of the material are applied. The actual wavelength that is appropriate for gas sensing is calculated by $\lambda = 1.24/E$, where λ is the wavelength in μm and E is the band-gap energy of the semiconducting material in eV. Therefore, the corresponding wavelengths for ZnO, In_2O_3, SnO_2, and WO_3 are calculated as 387 nm, 362 nm, 370 nm, and 420 nm, respectively.

The experiments were performed in the 365–405 nm wavelength range to study the sensors' behavior at different photon energies. The actual irradiance was maintained at 65 mW/cm^2 in all experiments to enable comparisons. Figure 3-7 represents the sensors' responses at different irradiation wavelengths. The results show that UV-LEDs with short wavelengths can result in better responses due to an improvement in the efficiency of semiconductor activity [62]. The response time of the sensors did not change significantly with the radiation wavelengths. For instance, the observed response time values of ZnO and In_2O_3 at 405nm were 200s and 280s, while their response times at 365nm were 197s and 254s, respectively.

Under irradiation at an energy level greater than the band-gap of the semiconductor material, electrons in the valence band (VB) are excited and migrate to the conduction band (CB). Therefore, given the band gaps of the synthesized metal oxide semiconductors (i.e. WO_3), overall semiconductor activation can ideally be achieved by photons with wavelengths of about 400 nm. However, there is an activation barrier in the charge-transfer process between the semiconductors and air molecules that requires photon energy levels slightly greater than the band-gap of the semiconducting material and band edge, with the

overpotential of oxygen reduction to drive the NO_2 reaction with reasonable reaction rates. This might better explain efficiencies at shorter wavelengths.

Although wavelengths below 365 nm have not been examined in our experiments, the literature demonstrates that using photons with excessive energies would enhance the inelastic scattering of electrons and reduce the charge mobilization efficiency [79]. Besides, from the light-source perspective, UV-LEDs with short wavelengths have short lifespans, limited availability, and high costs. Also, the efficiency of UV-LEDs is significantly reduced at shorter wavelengths. Therefore, UV-A (365 nm) LED systems may still achieve optimal performance due to their higher efficiency, higher power, and sufficient energy, which meets gas sensor device requirements. Therefore, the appropriate wavelength must be selected from an optimal window to achieve the best sensing performance.
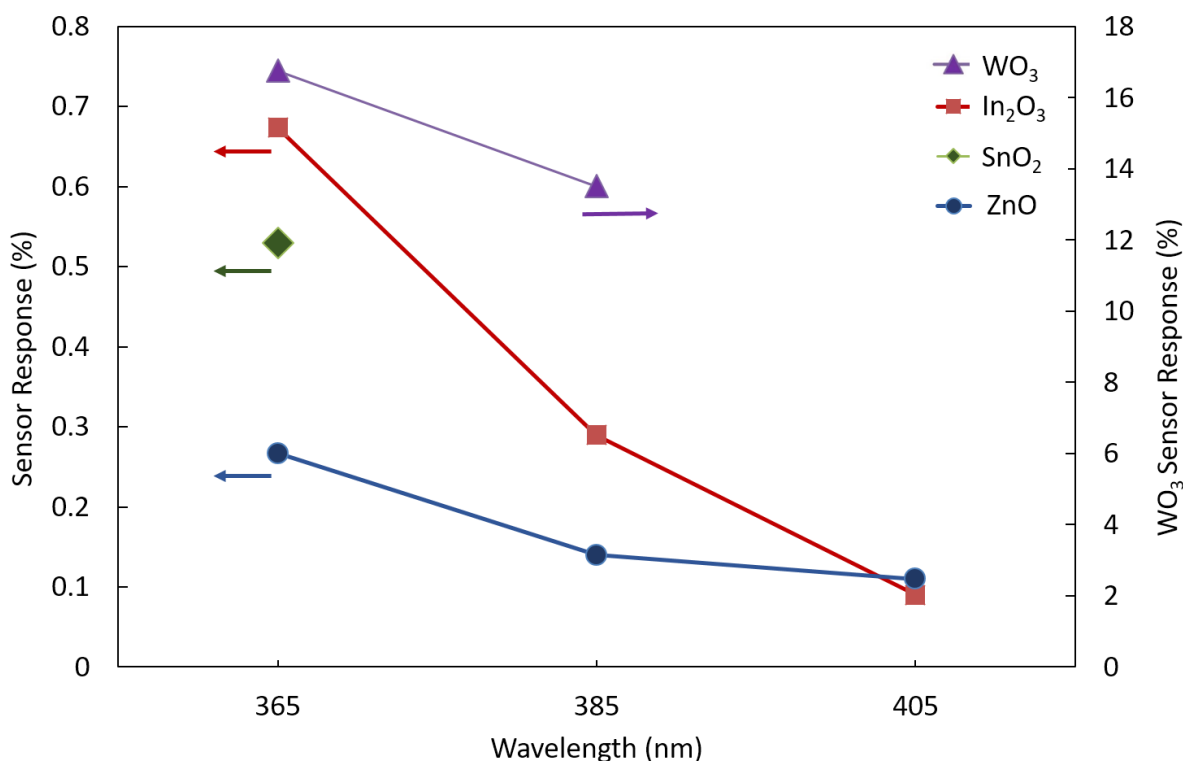
Figure 3-7: Effect of light source wavelength on the sensors responses to 5 ppm NO_2 at 65 mW/cm^2 irradiance. The decrease in responses at longer wavelengths is greater for semiconductors with higher band-gap. SnO_2 and WO_3 did not respond at wavelengths higher than 365 nm and 385, respectively, meaning that the photons did not have enough energy to generate charge carriers.

3.3.4.3 **Effect of irradiation pattern**

In addition to the amount of energy that reaches the surface per unit time, the pattern in which the surface is irradiated also changes the charge mobility features. The waveform of the LED emission can be adjusted electrically by controlling the applied LED current with an external modulation source such as a function generator. This unique feature of UV-LEDs makes them desirable for potentially enhancing sensing performance through pulsed irradiation. Driving UV-LED activated gas sensor systems in pulsed mode reduces heating and prevents damage of UV-absorbing surfaces while lowering the overall emission time of UV-LED, which results in improved yield, reduced scrap costs, and longer LED lifetime.

However, no studies exist in the open literature on the effect of pulsed mode irradiation on sensor behavior. To evaluate the potential of the shaped irradiation on the sensing performance of the prepared materials, the sensors' responses to 5 ppm NO_2 were measured under 365 nm UV-LED irradiation in various pulsation frequency modules (Figure 3-8). The applied voltage and the injection current to the LED were adjusted to obtain the irradiance of 65 mW/cm^2 in continuous operation. The duty cycle (the ratio of the pulse width to the period between pulses) was set to 50% for all experiments, and the irradiation frequency was altered from 0 (continuous) to 100 Hz.

The results confirmed that pulsation could significantly enhance the response of ZnO and In_2O_3 sensors. This can be demonstrated by irradiance-pulsation analogy: decreasing irradiance would reduce progressive desorption of the surface material and increase the gas sensor response. Similarly, pulsation would enhance the residence time of adsorbed materials, allowing for more efficient interactions of adsorbed molecules with the gas phase components. Thus, as a result of pulsation, a new equilibrium state between (photo)-adsorption and (photo)-desorption of surface and gas molecules is formed, leading to higher reaction yields.

49

However, SnO$_2$ and WO$_3$ responded quite differently in pulsed mode, and the pulsation resulted in a continuous increase of the response without reaching a plateau value. The SnO$_2$ and WO$_3$ sensor responses at 10 Hz frequency are shown in Figure A3-2. Although the WO$_3$ sensor showed a response of 19.2 at 100 Hz frequency, the response time and recovery time were over 2 h, which are significantly greater than those for continuous illumination. These behaviors can be attributed to the substantial contribution of surface processes, rather than inter-band transitions, to the conductance change under illumination/darkening [30]. More studies on UV-LED pulsed illumination are needed to confirm the enhanced gas sensing effect and reveal the exact mechanism. Table 1 summarizes the sensor responses in different operating conditions. The results reported in the present work confirms that a significant increase in the response of the UV-activated NO$_2$ sensors can be achieved if optimal operating conditions applied.
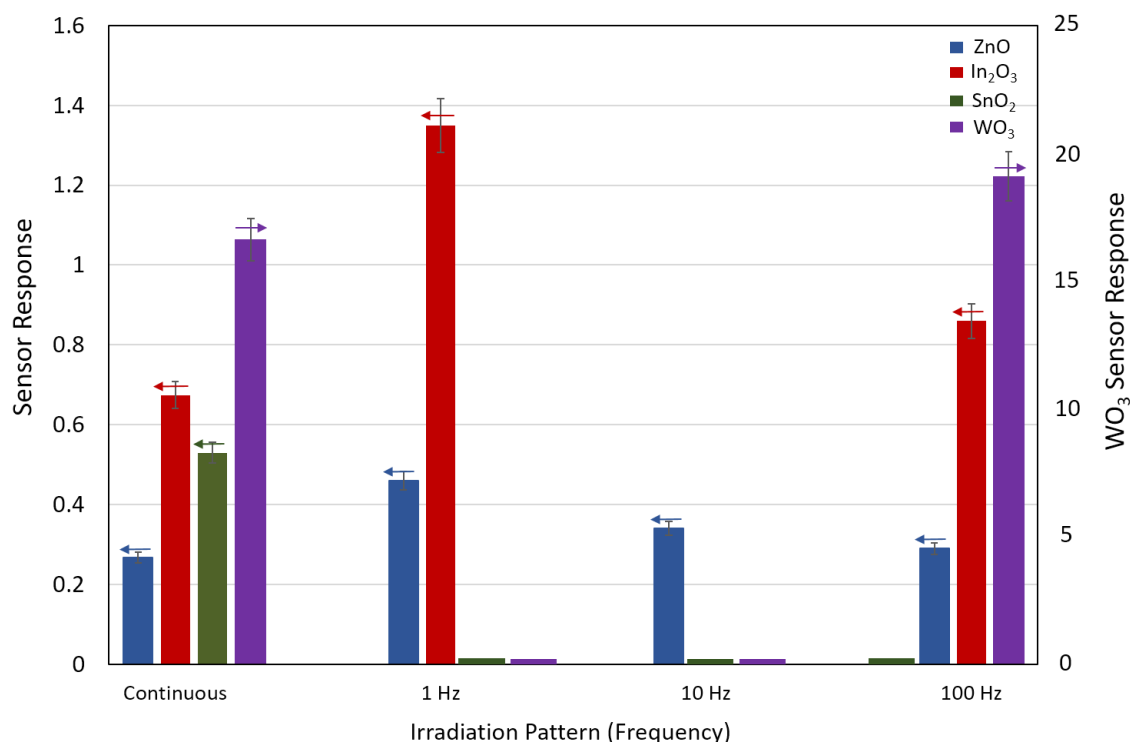
Figure 3-8: The effect of irradiation pattern (pulsation frequency) on the performances of the sensors under 365 nm UV-LED irradiation. The error bars represent 95% confidence intervals for the results.

Table 3-1: A summary of the responses of the prepared sensors to 5 ppm NO_2 under UV-LED irradiation in different operating conditions

Sensor Response ($\Delta R/Ra$)

	Irradiance (mW/cm^2) *at 365 nm*				Wavelength (nm) *at 65 mW/cm^2*			Pulsation Frequency (Hz) *at 365 nm and 65 mW/cm^2*		
	8	65	145	251	365	385	405	1	10	100
ZnO	0.412	0.267	0.218	0.129	0.267	0.16	0.12	0.46	0.34	0.29
In$_2$O$_3$	1.261	0.674	0.431	0.247	0.674	0.31	0.19	1.35	-	0.86
SnO$_2$	-	0.53	0.3	0.08	0.53	-	-	-	-	-
WO$_3$	113	16.7	9.6	7.5	16.76	10.51	-	-	-	19.2

3.3.4.4 Effect of concentration

Among the prepared sensors, ZnO and In$_2$O$_3$ were selected for concentration measurements. Figure 3-9 shows the responses of ZnO and In$_2$O$_3$ sensors to 5–100 ppm of the target gas under UV-LED irradiation at their optimal performance. The sensing results were found to be stable and repeatable in all experiments. The responses increased in higher gas concentrations, reaching 2.95 and 7.5 at 100 ppm NO_2 for ZnO and In$_2$O$_3$, respectively. This trend is due to the involvement of more electrons in relative reactions at higher concentrations.

For ZnO sensors, the recovery time did not change considerably. However, the recovery time constants of In$_2$O$_3$ sensors increased with increasing concentration. At 100 ppm, the sensor resistance did not return to its initial value because of stable adsorption at high concentrations. The response of In$_2$O$_3$ increased more rapidly than ZnO at higher concentrations, which might be due to the inherent capability of In$_2$O$_3$ to adsorb more target gas molecules by providing a higher number of electrons on the

surface. Furthermore, the saturation limit of In_2O_3, which is the maximum detectable amount of target gas, was achieved to be higher than that of ZnO.
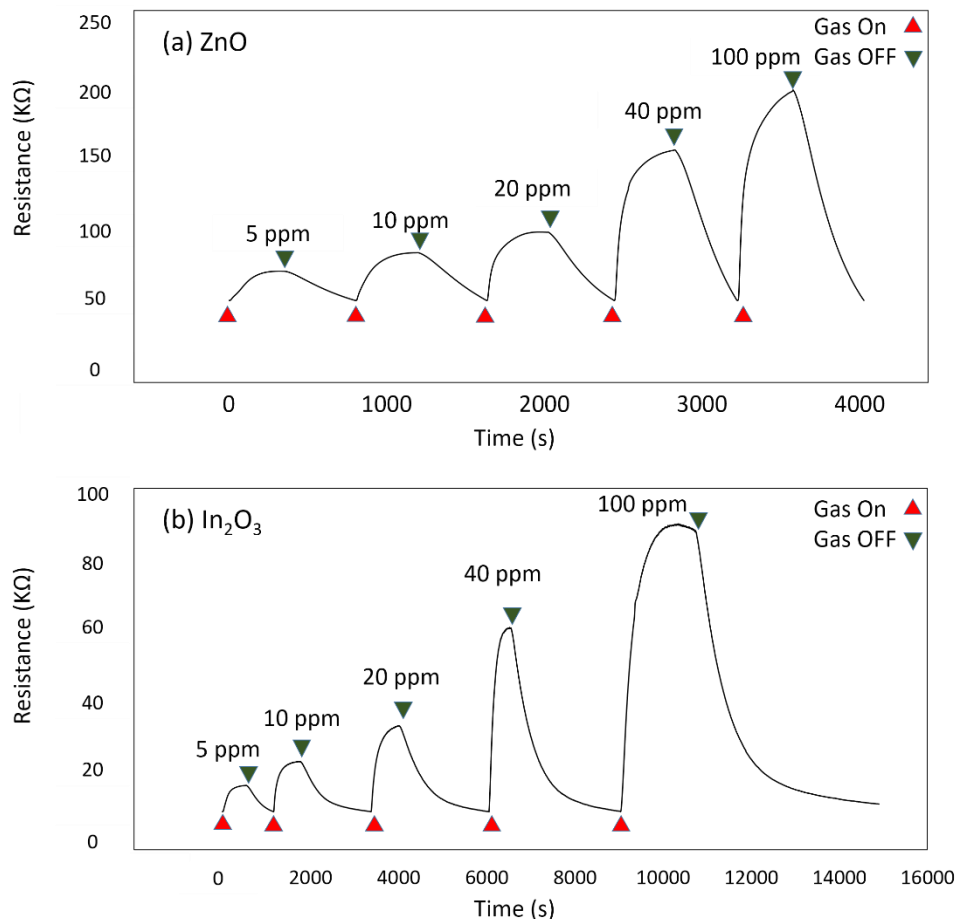
Figure 3-9: Sensor responses at different concentrations of NO_2 gas under UV-LED illumination at their optimal irradiance: (a) ZnO at 25 mW/cm^2, (b) In_2O_3 at 65 mW/cm^2

3.3.4.5 **Stability and selectivity**

To examine the long-term sensing performance, the response of the sensors to 5 ppm NO_2 was examined in about one year after its preparation under the same operating conditions as those when the sensor was originally tested (365 nm UV-LED irradiation and 65 mW/cm^2 irradiance). The results confirmed that the sensors' responses are quite stable and reproducible. This observation is consistent

with the fact that room-temperature UV-activated gas sensing improves the sensor's stability, as opposed to the conventional high-temperature sensing. As shown in Figure 3-10, selectivity analysis was also performed to evaluate the sensors' responses under the same operating conditions against interfering gases such as Ammonia (NH_3) and Carbon Monoxide (CO). Although the concentration of NH_3 (50 ppm) and CO (50 ppm) were significantly greater than that of NO_2 (5 ppm), the UV activated ZnO, SnO_2, and WO_3 sensors exhibited high selectivity to NO_2, while In_2O_3 showed higher response to 50 ppm NH_3 (2.06). Among the semiconductors tested, WO_3 was the only sensor that responded to 50 ppm CO (0.69).
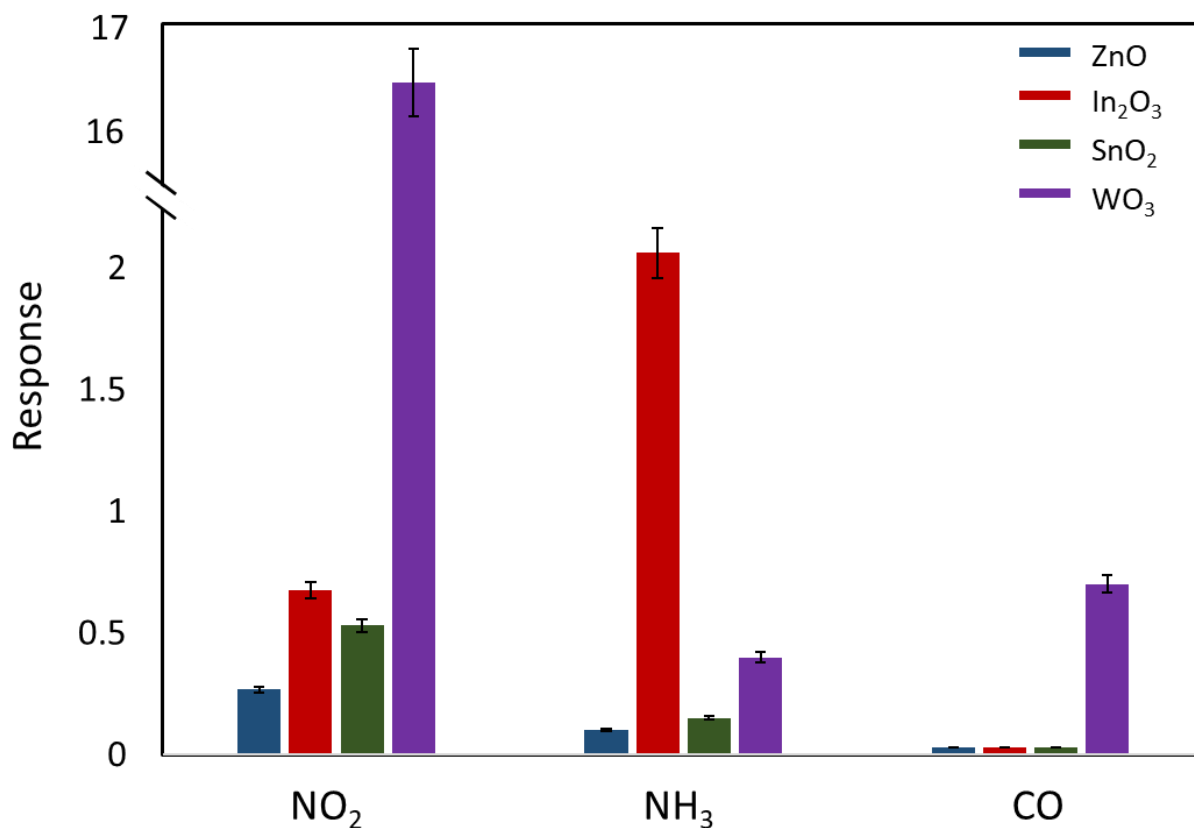
Figure 3-10: The response of prepared sensors to 5 ppm NO_2, 50 ppm NH_3 and 50 ppm CO

The relatively high sensitivity, short response time, and long stability, along with the tunable responses of UV-LED activated semiconductor sensors indicate that they are promising alternatives to conventional high-temperature chemical sensors.

In conclusion, the unique characteristics of UV-LEDs, particularly multiple wavelengths and pulsed illumination, could potentially improve sensing performance under optimal conditions. The radiation source specifications could significantly affect the adsorption/desorption of NO_2 gas molecules at room temperature. Appropriate irradiation conditions are required for each sensor to achieve the highest response and shortest response time while having a complete recovery. The highest response can be observed at an intermediate UV wavelength and optimal irradiance under pulsed irradiation. Further investigations on the influencing parameters and mechanisms are required to apply UV-LEDs more efficiently as the activation source for gas sensing materials.

Chapter 4: Synthesis and performance evaluation of photo-activated Ag:ZnO nano-ellipsoids

4.1 Introduction

Among the groups of metal oxides that have been studied for gas sensing applications, ZnO nano-materials have shown promise because of high electron conductivity features [81–83]. ZnO has strong luminescent properties, broad UV absorption, and a low cost [84]. The photo-activity of ZnO can be improved by combining it with other chemicals. This combination lowers the required activation energy and reduces the recombination rate of photo-generated charge carriers [85,86]. Several noble metals, such as gold, palladium, platinum, and silver, have been reported to act as a co-catalyst to improve the photo-activity [87–90]. It has been reported that the metal oxide morphology and surface properties induced by silver doping facilitates the interfacial charge transfer and modifies the light-absorption ability, resulting in improved gas-sensing properties [86,91–93].

Several methods have recently been proposed to synthesize Ag-loaded ZnO nanoparticles [86,89,94–97]. However, a low-temperature solution-based approach is more desirable for large-scale production [91]. In this research, Ag-loaded ZnO nanostructures were synthesized by a facile co-precipitation method, and the structural properties were determined by several characterization methods. This study reports the sensing performance characteristics of Ag-loaded ZnO nanomaterial activated with UV-LEDs with the appropriate wavelength to enhance the sensitivity of the developed sensors toward NO_2, which is a toxic gas that is produced in large amounts by chemical combustion plants and automobiles and significantly contributes to environmental problems.

4.2 Material preparation

ZnO synthesis: All the chemicals used in this study were obtained from Sigma-Aldrich. Zinc nitrate hexahydrate ($Zn(NO_3)_2.6H_2O$) and 2.0 M ammonia (NH_3) solution in ethanol (CH_3CH_2OH) were used as precursors. To prepare the ZnO layer, 0.89 g of zinc nitrate powder was dissolved in 100 ml of a solution containing 85% ethanol and 15% methanol. The obtained solution was vigorously stirred for 30 min at 50 °C in a water bath under a fume hood. The ammonia solution was then added dropwise at a rate of 1 drop/s at the same temperature to reach pH ≥9. The resulting solution was then stirred for 4 h and cooled slowly to room temperature. The obtained precipitates were used to deposit ZnO layers over Al_2O_3 substrate. The deposited material was annealed at 550 °C for further oxidation.

Ag-loaded ZnO synthesis: Zinc nitrate hexahydrate ($Zn(NO_3)_2.6H_2O$) and silver nitrate ($AgNO_3$) were used as metal precursors. In a typical synthesis process, 0.1 M zinc nitrate hexahydrate solution was prepared in 100 mL distilled water at 50 °C. Silver nitrate was dissolved in the solution to obtain Ag:ZnO with a 1:10 molar ratio. The solution was then stirred for 30 min at 50 °C to fully mix the dissolved material. Then, the reducing agent was added dropwise to the solution until pH ≥9. The precipitates were then collected by centrifugation, and aged at 80 °C for 6 h. The collected precipitates were spin-coated on alumina substrate pre-deposited by interdigitated gold electrodes. The deposited sensing layer was then calcined at 550 °C for 2 h.

4.3 Results and discussion

4.3.1 Characterizations of ZnO and Ag-loaded ZnO sensors

The XRD patterns of the synthesized ZnO and Ag:ZnO nanoparticles are shown in Figure 4-1. The peaks located at 31.76, 34.42, and 36.25 of the undoped sample address the wurtzite phases. As Ag is added to the pure ZnO, a sharp peak at 38.11° is observed in the XRD pattern; this peak corresponds to

metallic Ag, confirming the existence of Ag clusters on the sample. XRD also shows that the intensity of the peaks decreases upon the addition of Ag atoms, suggesting that the crystallinity is reduced in the Ag:ZnO sample. The backward shift in the XRD diffractogram indicates the possible substitution and incorporation of Ag atoms into the ZnO lattice, which induces lattice enlargement. Thus, metallic Ag clusters and incorporated Ag+ ions are simultaneously present in the samples.
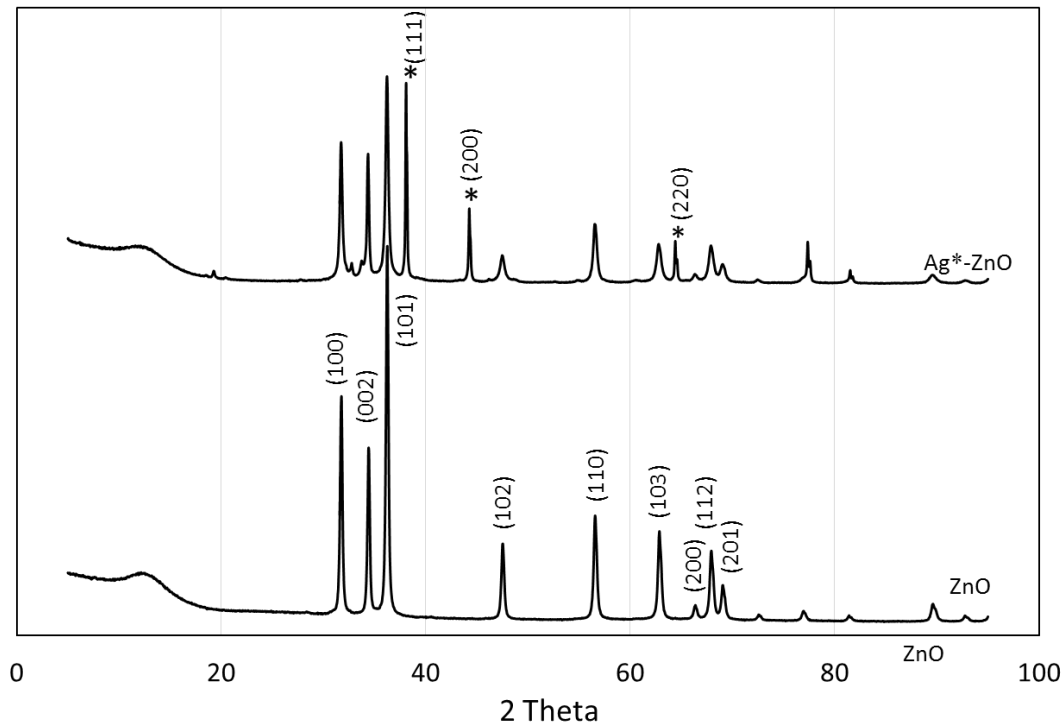
Figure 4-1: XRD analysis of pure ZnO and Ag-loaded ZnO. The figure confirms Ag clusters in the sample and shows lower crystallinity of Ag-loaded ZnO nano-particles

The morphology of the prepared ZnO and the Ag-loaded ZnO were examined by FE-SEM imaging. Figure 4-2a shows the pseudo-spherical nanoparticles of pure ZnO in the form of a porous structure. Figure 4-2b exhibits the ellipsoidal Ag:ZnO nanoparticles that are uniformly distributed in the layer. The width of nano-ellipsoids at the corners is ~20 nm, while the width at the center is ~200 nm; the length is

approximately 500 nm. The shapes and characterization specifications are in good agreement with those reported in the literature [91].
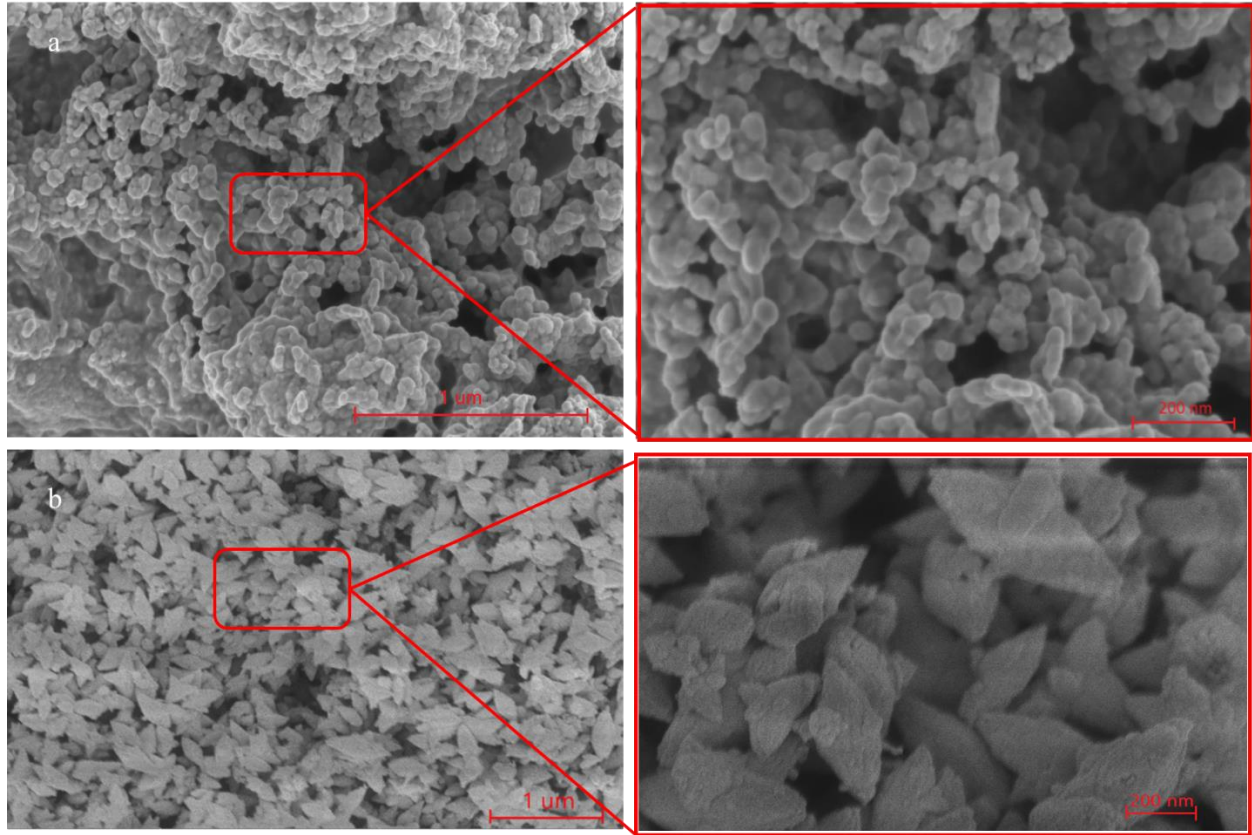
Figure 4-2: FESEM analysis of pure ZnO (a) and Ag-loaded ZnO (b)

4.3.2   Sensing performance

The sensing performances of the synthesized materials were analyzed by studying the resistance variations of the layers at different concentrations of NO_2. Sensitivity, response time, and stability are the three main factors that indicate how well a gas sensor device is performing. Sensor response value addresses the maximum change in the relative resistance of thin films under different conditions. It is defined as the thin film resistance change when exposed to the target gas and pure air normalized by the initial resistance in the air. Initially, to examine the effect of UV irradiation on ZnO resistance, UV-LEDs

were periodically turned on and off, and the photo-induced sensor response was measured over time. When the sample was irradiated with UV, the conductance increased by about an order of magnitude due to the electron/hole pair creation in the material. When the irradiation was stopped, the resistance increased, within a few minutes (Figure 4-3). The irreversible shift in resistance after the first irradiation is attributed to the structural defects and disorders induced by the radiation [27].
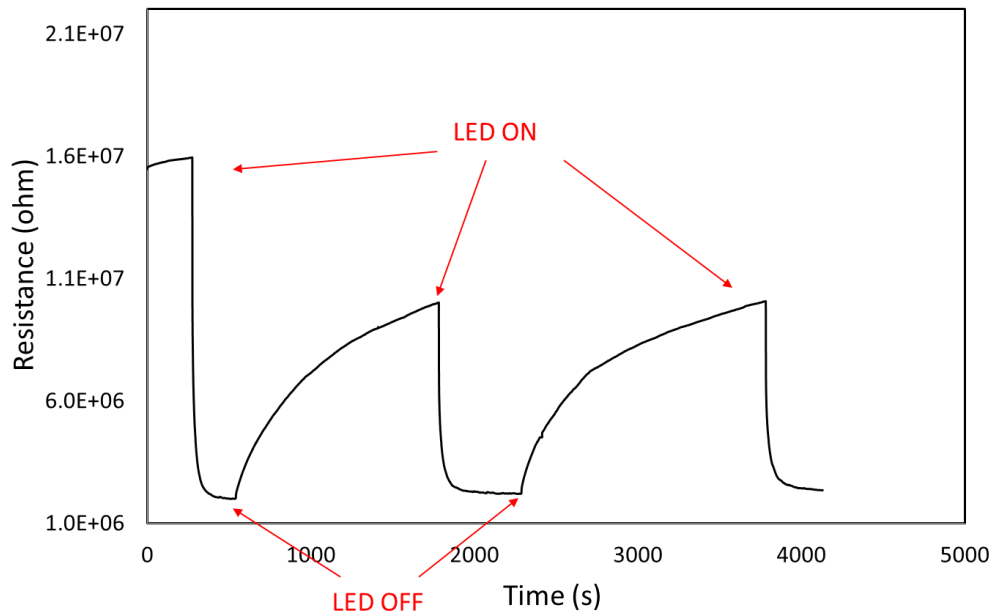
Figure 4-3: ZnO photo-induced response to UV-LED ON/OFF cycle (at 8 mW/cm^2).

The performance of the developed sensors to low concentrations of NO$_2$ was tested in the absence and presence of UV radiation. No resistance change was observed when the sensors were exposed to 5 ppm NO$_2$ in the absence of UV radiation. However, the photo-induced resistance variations under UV-LED illumination were significant upon exposure to NO$_2$. The remarkable resistance changes in UV-assisted sensors can be described based on the increased gas-surface interaction due to the existence of

photo-generated charge carriers. Figure 4-4 shows the sensitivities of pure ZnO and Ag-loaded ZnO when 5 and 10 ppm NO_2 were passed over the sensor under 8 mW/cm^2 of UV illumination. The sensing response of Ag:ZnO to 5 ppm NO_2 was 0.98, while the response of pure ZnO was 0.41, confirming that the sensitivity of Ag:ZnO was enhanced by a factor of greater than 2 compared to pristine ZnO.
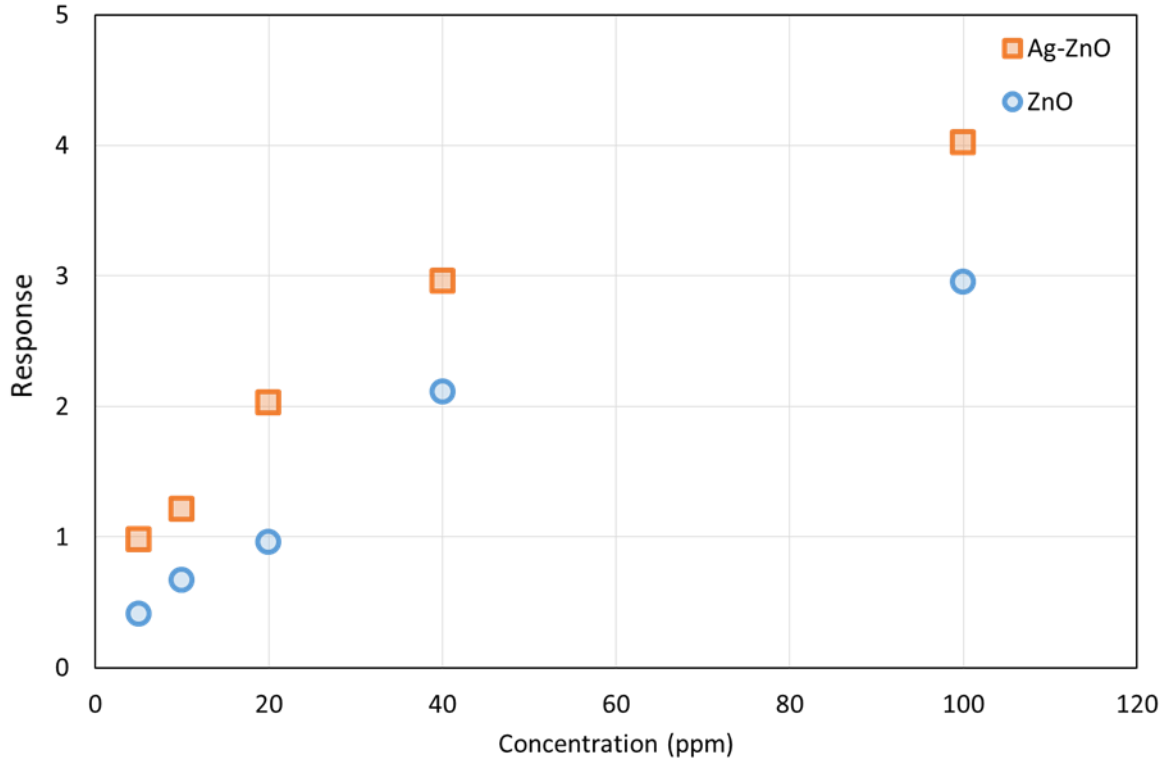
Figure 4-4: Sensing response of pure ZnO and Ag-loaded ZnO at 8 mW/cm^2 toward (a) 5 ppm NO_2 and (b) 10 ppm NO_2. The target gas exposure started at time near zero and stopped at t=Δ.

The experiments at higher concentrations of NO_2 also confirmed that Ag:ZnO responds more efficiently and with higher sensitivity in a wide range of concentrations (Figure 4-5). The increased sensitivity at higher concentrations of NO_2 can be attributed to the higher number of electrons involved in the surface reactions. The response time (τ_{res}) is defined as the time required for the sensor to increase

from 10% to 90% of its total sensitivity. The response time of both ZnO and Ag:ZnO was ~200 s at 5 ppm NO_2.
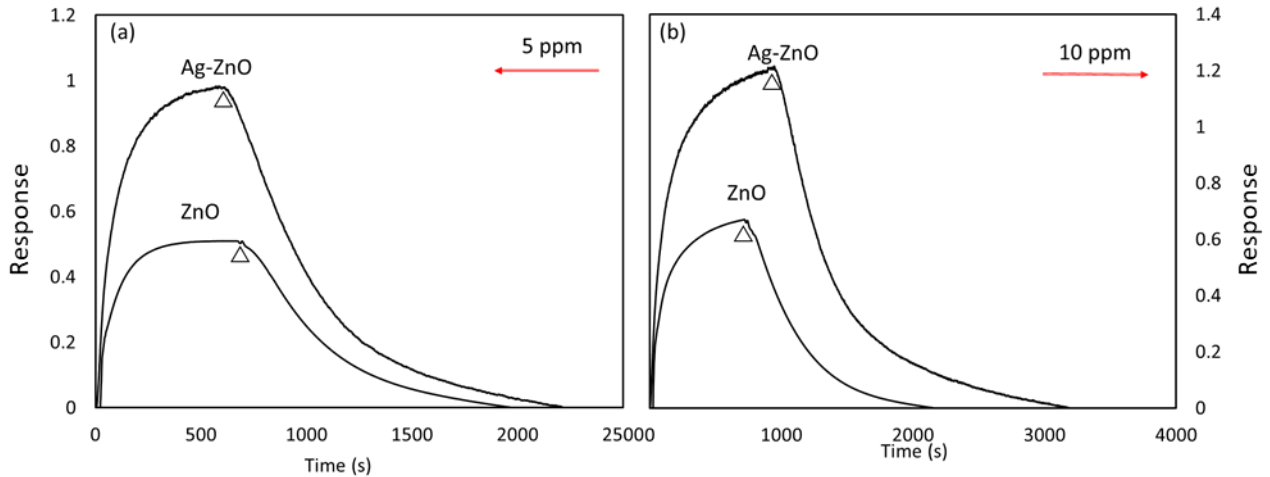
Figure 4-5: Response of pure ZnO and Ag-loaded ZnO at various concentrations of NO_2. The response increases with increased target gas concentrations.

In a typical UV-based gas sensor, UV wavelength and power intensity determine the energy of the photons reaching the exposed surface. This energy affects the equilibrium surface reactions and plays a determining role in the response curve. Irradiance, an indication of the energy received by a surface, is defined as the rate of photons that strike the surface per unit area and depends on the intensity and distance of the photon source. Figure 4-6 shows the effect of irradiance on the sensitivities of the developed sensors to 5 ppm NO_2. Increasing irradiance enhances the photo-desorption rates of adsorbed components, thus reducing the sensitivity. In other words, as the irradiance increases, the higher rate of oxygen ion removal and adsorbed target-gas molecules, which are the primary reactants, limits the ability of surface reactions to fully proceed on the sensor's surface. However, the response time also decreases with increasing irradiance. Therefore, there should be an optimal value that provides high sensitivity and a fast response. Since the range of response time variation was not significant (200 s at 8 mW/cm^2 and

170 s at 250 mW/cm^2) compared to the sensitivity changes of Ag:ZnO (0.98 at 8 mW/cm^2 and 0.49 at

250 mW/cm^2), 8 mW/cm^2 is suggested as the best operating irradiance within the experimental range of

this study.
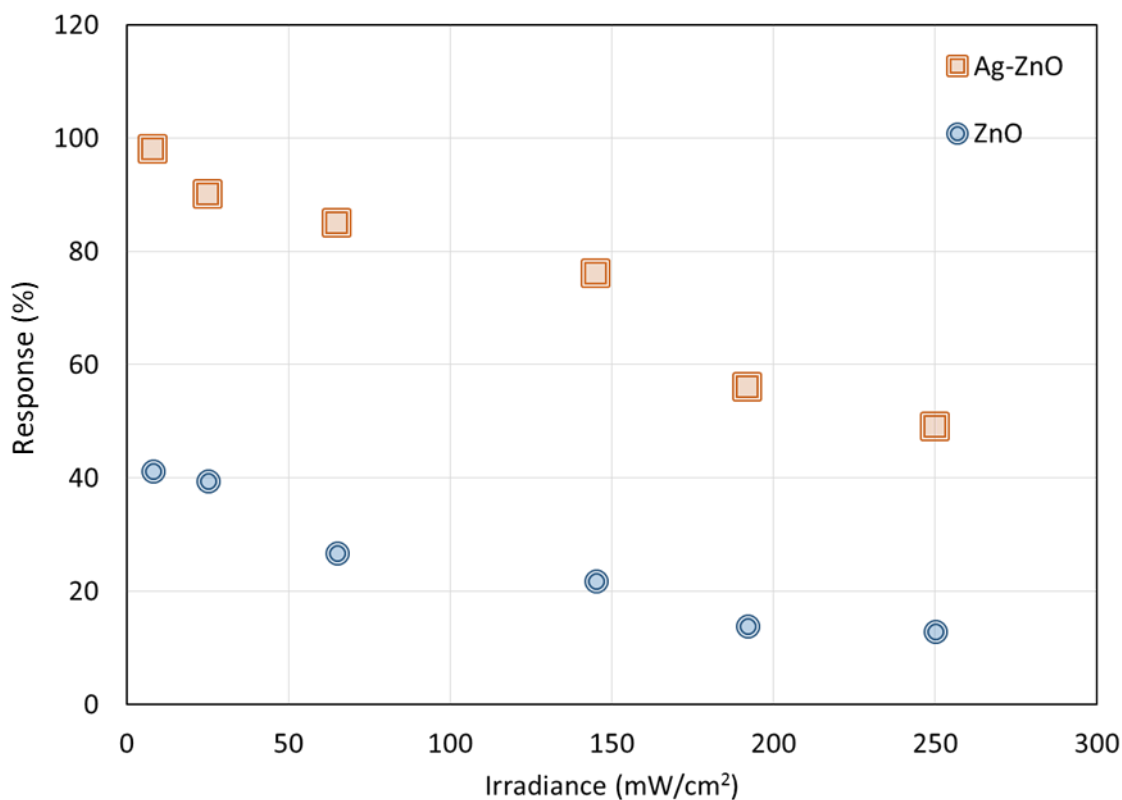
Figure 4-6: Sensitivities of ZnO and Ag-loaded ZnO to 5 ppm NO$_2$ at different irradiances, increasing irradiance reduces the response

4.3.3   Sensitivity enhancement using Ag:ZnO

Improvements in the gas sensing properties of Ag-loaded ZnO nano-ellipsoids are related to the synergetic effects of the semiconductor composite. The suggested mechanism to explain the enhancement in the sensing response of Ag-loaded ZnO nanoparticles is based on the increase in the electron utilization ratio and the reduction in the recombination rate because of the trapped electrons in

the Ag nanoparticles upon excitation [84]. These phenomena can also lead to the injection of more electrons into the active surface area and improve the adsorption capability of the target gas. When a wide band-gap semiconductor is coupled with a narrow one, the conduction band level at the hetero-interfaces shifts to more negative values. The Ag:ZnO Fermi level lies between the conduction band and the Fermi level of pure ZnO. Thus, it can control the charge mobility and enhance sensitivity [86,91]. Also, it has been shown that adsorption capability is directly related to the number of oxygen vacant sites [98]. When Ag is incorporated into the ZnO lattice, oxygen vacancies are created due to charge differences between Ag^+ and Zn^{2+} ions. Figure 4-7 shows the electron mobilizations and the respective reactions of Ag-loaded ZnO sensors in NO_2 atmosphere.

$$O_{2(gas)} \leftrightarrow O_{2\,(ad)}$$
$$O_{2\,(ad)} + e^- \leftrightarrow O_{2(ad)}^-$$

$$NO_{2\,(g)} + O_{2\,(ad)}^- + 2e_{hv}^- \leftrightarrow NO_2^- + 2O^-$$
$$2NO_{2\,(gas)} + e_{hv}^- \rightarrow 2NO_{(gas)} + O_{2\,(ad)}^-$$
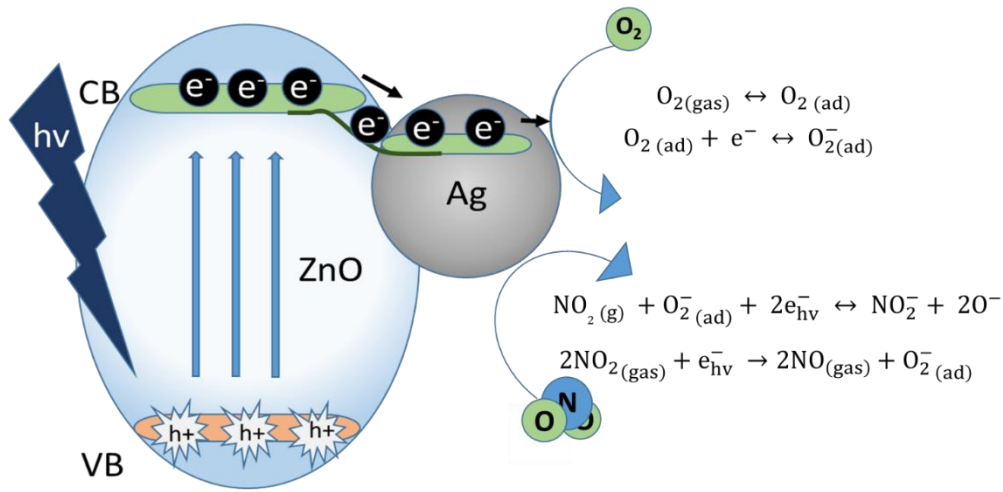
Figure 4-7: Improvements in the gas sensing properties of Ag-loaded ZnO nano-ellipsoids to NO_2 gas.

In conclusion, incorporating silver nanoparticles in the ZnO lattice structure could remarkably enhance the sensor response to NO_2. The improvement can be attributed to the special properties of the Ag-ZnO structure that lead to the increase in the electron utilization ratio and the reduction in the recombination rate because of the trapped electrons in the Ag nanoparticles upon excitation.

Chapter 5: **Synthesis and performance evaluation of photo-activated Pt decorated single crystal ZnO nanowires**

5.1 Introduction

Developing high-performance gas sensors requires highly engineered sensing materials that have effective interaction with the target gas components. Recently, ZnO nanoparticles (NPs) and nanowires (NWs) have been widely studied for photo-activated gas sensing applications, especially for trace NO_2 detection, due to their unique optical and electrical properties [99–104]. Fabbri et al. [62] studied the ZnO nanoparticles under light-emitting diodes (LEDs) with a wide range of wavelengths (365–525 nm) against several gases, such as NO_2, alcohols, and hydrocarbons. Higher response and faster recovery time were observed at shorter wavelengths, while long wavelengths made irreversible responses. Fan et al. [43,64] compared the sensing performance of different patterns of polycrystalline ZnO against NO_2 under 365 nm UV-LED with 25 mW/cm^2 irradiance. No response was observed for ZnO nano-particles, while the response of ZnO nanowires towards 20 ppm NO_2 and 100 ppm H_2 were 0.83 and 1.6, respectively. The improved performance of ZnO nanowires was attributed to the large surface-to-volume ratio and the Joule heating effect imposed by applying continuous bias. Accordingly, Catto et al. [105] showed that one-dimensional ZnO nano-rods are more sensitive to ozone under 351 nm UV-LEDs, compared to ZnO NPs.

It has been shown that the photo-activity of ZnO NWs can be further improved by noble metal loading such as Platinum (Pt) nanoparticles, which has unique optical and catalytic properties [90,106,107] These modifications can lower the required activation energy and reduce the recombination rate of photo-generated charge carriers within the sensing material [108].

Several metal loading techniques have been proposed recently to load noble metals onto semiconductor layers, such as conventional impregnation, photo-deposition, sputtering, and wet-chemical reduction methods [109–114]. However, the gas-phase approaches require expensive equipment and extreme preparation conditions for the metal precursor delivery. Although the impregnation and reduction methods are relatively simple, they suffer from large particle size distribution and lack of control of particle dispersion. In contrast, photo-deposition selectively locates the metal nanoparticles at the reaction sites, and normally no post-activation step is needed. This is due to the direct reduction of a metal salt to its metallic state as the result of the interaction with photo-induced electrons of the sensing layer. Since the photons evenly strike the sample surface, the excited electrons will cover the whole area. As a result, the particles are well-dispersed all over the sample using the photo-deposition technique. The effectiveness of photo-deposition for surface modification has been reported previously in the literature [115,116]. Figure 5-1 represents a schematic illustration of the photo-deposition process on the surface of a semiconductor layer.
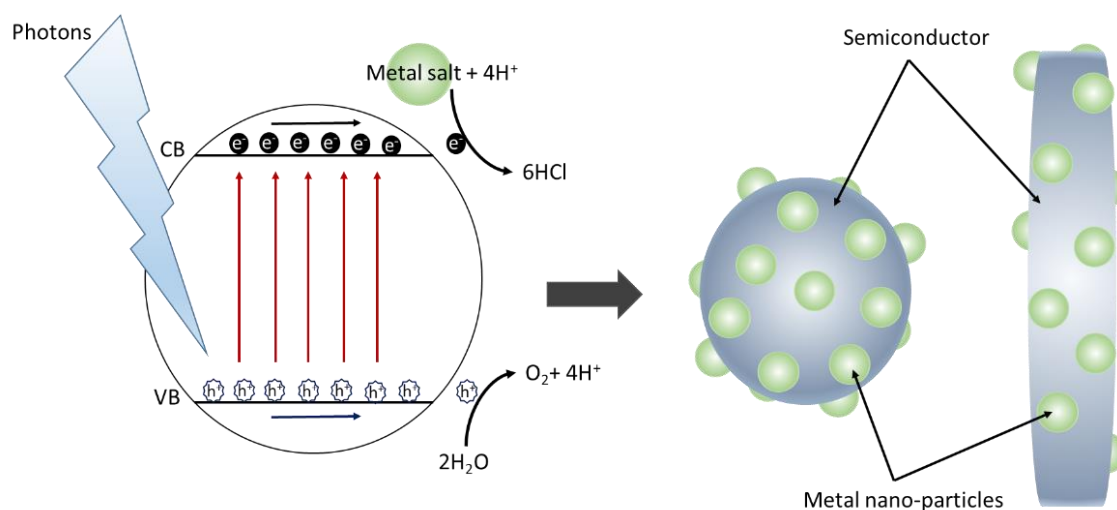
Figure 5-1: Schematic illustration of the photo-deposition technique for metal loading

In this study, the photo-responded gas sensing behavior of ZnO nanostructures is examined. The gas sensing behavior of ZnO nano-particles is initially characterized under different irradiances in NO_2 environment. Then, the response of one-dimensional ZnO structure is studied in the optimum condition. Further, to rule over the energy structure of the ZnO sensing layer, Pt nano-particles in 0.01, 0.1 and 1 wt. % concentrations are loaded on the structure through a photo-deposition technique. The ZnO NPs, NWs and Pt loaded NWs samples are prepared by precipitation, hydrothermal and photo-deposition methods, respectively. The results indicated that the sensor response to 5ppm NO_2 could be significantly enhanced by using ZnO NWs and Pt-loaded ZnO NWs, compared to ZnO NPs.

5.2   Material preparation

All chemicals were of analytical grade and purchased from Sigma-Aldrich Canada Corporation and used without further purification.

5.2.1   ZnO nanoparticles:

Zinc nitrate hexahydrate ($Zn(NO_3)_2.6H_2O$) and 2.0M ammonia (NH_3) solution in ethanol (CH_3CH_2OH) were used as source materials. 0.89 g of zinc nitrate powder was dissolved in 100 mL of the ethanol solution. The solution was vigorously stirred for 30 min at 50 °C in a water bath under a fume hood. Drops of the ammonia solution were then added to the solution at a rate of 1 drop/s, while measuring the pH value continuously to reach pH ≥ 9. The solution was then stirred for 4 h and slowly cooled to room temperature. The resulting precipitates were centrifuged, washed, and calcined at 550 °C for 2 h.

5.2.2 ZnO nanowires (NWs):

5.2.2.1 Seeding

A substrate (pre-deposited with interdigitated gold electrodes) was cleaned with a 50-50 V% isopropanol-ethanol solution and was seeded with ZnO nanoparticles (NPs) by triple spin coating of zinc acetate solution in absolute ethanol. The substrate was thermally treated for 2 min between each coating at 180 $^{\circ}$C, to ensure adequate adhesion of NPs. The coated substrate was annealed in a laboratory muffle furnace at 250 $^{\circ}$C for 20 min.

5.2.2.2 Growth

Single crystal ZnO nanowires were fabricated through the technique described in the literature [117]. The seeded substrate was placed upside-down in an aqueous stoichiometry solution of $Zn(NO_3)_2.xH_2O$ and Hexamethylenetetramine (HMT) in a glass vial. The vial was placed in a laboratory oven at 93 $^{\circ}$C for 6 h. The obtained NWs were washed with pure water and ethanol and subsequently annealed in a furnace at 350 $^{\circ}$C for 30 min.

5.2.2.3 Platinum loading

In a typical procedure, the as-fabricated ZnO NWs coated substrate was placed in a top-irradiated photo-reactor filled with an appropriate amount of hexachloroplatinic acid ($H_2PtCl_6.6H_2O$) in distilled water. The reaction chamber was de-oxygenated with ultra-pure nitrogen for 20 minutes before irradiation. The coated substrate was then irradiated with a high-pressure mercury lamp for 30 min. After this period, the irradiation was terminated, and the Pt-loaded ZnO thin film was taken out, washed with pure water, dried at room temperature and subsequently treated at 350 $^{\circ}$C for 20 min.

5.3 Results and discussion

5.3.1 Microstructure and morphology

Figure 5-2 demonstrates the X-ray diffraction of prepared ZnO nanoparticles and nanowires. Both samples exhibit the prominent pattern of hexagonal ZnO, which are indexed by JCPDS file No. 36-1451. The XRD data in Figure 5-2a suggest the crystalline structure of the synthesized ZnO NPs, with average crystallites size of 53.1 nm, estimated through Scherrer equation ($d_{crystallites} = k\lambda/\beta cos\theta$). The highly crystalline hexagonal structure of the prepared ZnO NWs can be identified from the X-ray diffraction pattern in Figure 5-2b. Treating the acetate precursor at 250 ºC results in exposed crystallographic facets of ZnO seeds to wurtzite c-plane, promoting the crystallization of nanowires towards the (002) direction. The high intensity of the (002) peak at $2\theta=34.5º$ in the XRD pattern of the fabricated NWs, in contrast to its bulk and nanoparticle counterparts, testifies that the one-dimensional growth occurred through the hexagonal c-axis crystallization. Presence of (101) diffraction peak at $2\theta=36.3º$ is likely attributed to the secondary growth direction, particularly in structures where the nanowire arrays are not fully-aligned; while, the (100) peak at $2\theta=31.8º$ refers to the six symmetrical crystallographic planes parallel to the [002] axis with various polarities. As expected, the Pt or PtO diffraction patterns were not observed in any of the samples diffraction data, confirming the formation of heterojunction active sites on the surface of NWs, rather than homogenous doping within the crystalline structure [118,119]. This is important, since metal doping, the so-called homogeneous incorporation into crystallographic structure creates mid-band energy levels within host materials band-gap, and subsequently changes the electrochemical characteristics of the host material and alters its charge transfer mechanism. On the other hand, surface deposition of metal active, as co-catalyst, promotes the rate of redox reaction, while maintains the electrochemical properties of the structure identical to an intrinsic semiconductor.
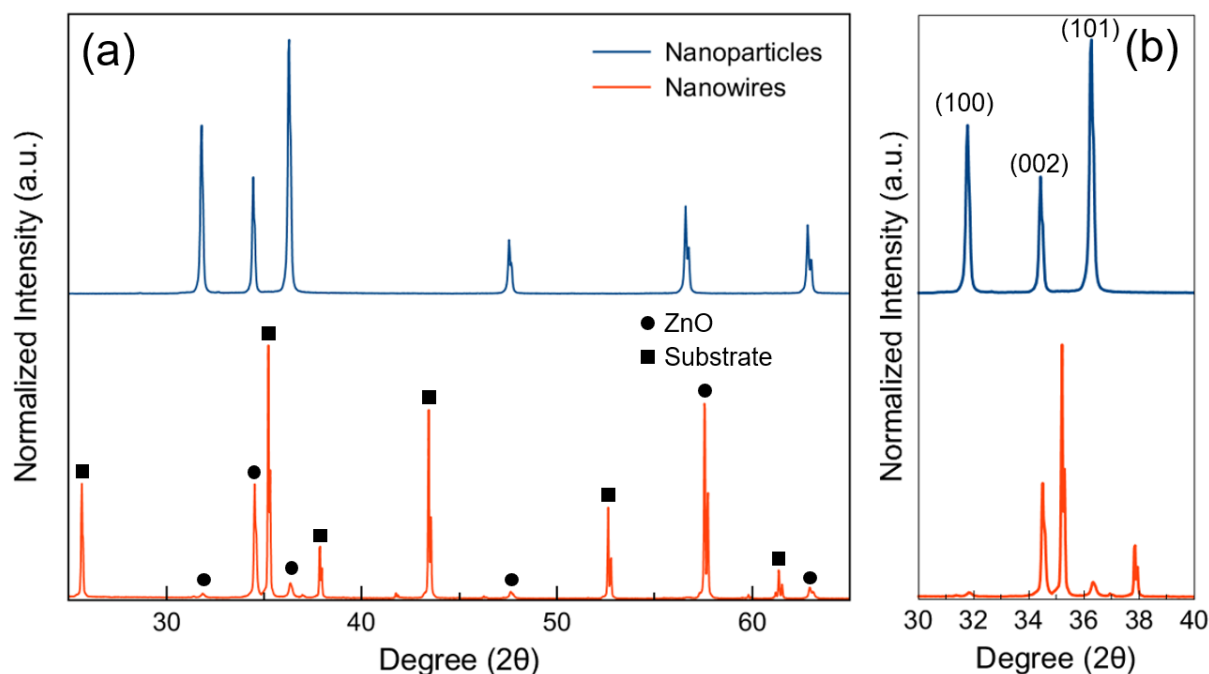
Figure 5-2: XRD analysis of the synthesized sensing material.

Figure 5-3 shows the high-magnification FE-SEM images of bare and Pt-loaded ZnO samples. The ZnO NPs in Figure 5-3a consist of 50-100 nm semi-spherical shape particles, agglomerated, due to high-temperature sintering, to bundles with size up to 200 nm. Comparing the crystallite size estimated from XRD data and particle diameter in SEM data suggest relatively high crystallinity of the synthesized nanoparticles, with a low density of defects and grain boundaries. Figure 5-3b shows the as-prepared ZnO NWs with an estimated density of $0.7 \times 10^8 - 1.4 \times 10^8$ NW/cm^2, diameter between 140–300 nm, and an average length of 4.0 µm. The hexagonal tip of the prepared NWs indicates their single crystal structure with favored growth direction towards the wurtzite *c*-axis, in agreement with XRD data. The high-resolution micrograph of Pt decorated samples revealed that the morphology of thin film is affected by the metallic precursor content during UV-induced photo-deposition. As illustrated in Figure 5-3c, the morphology of NW arrays remained unchanged after 0.01 wt% Pt loading, compared to the pristine ZnO

NWs. However, as demonstrated in Figure 5-3d, increasing the Pt content in photo-deposition solution to 0.1 wt% formed agglomerated regions within the ZnO NWs structure. The density of these regions was further increased for 1 wt% Pt-ZnO NWs sample, as illustrated in Figure 5-3e. Formation of these agglomerates is likely related to the presence of photo-deposited Pt with comparable volumetric-content to NW arrays, and mostly to the residues of the chloroplatinic acid precursor.
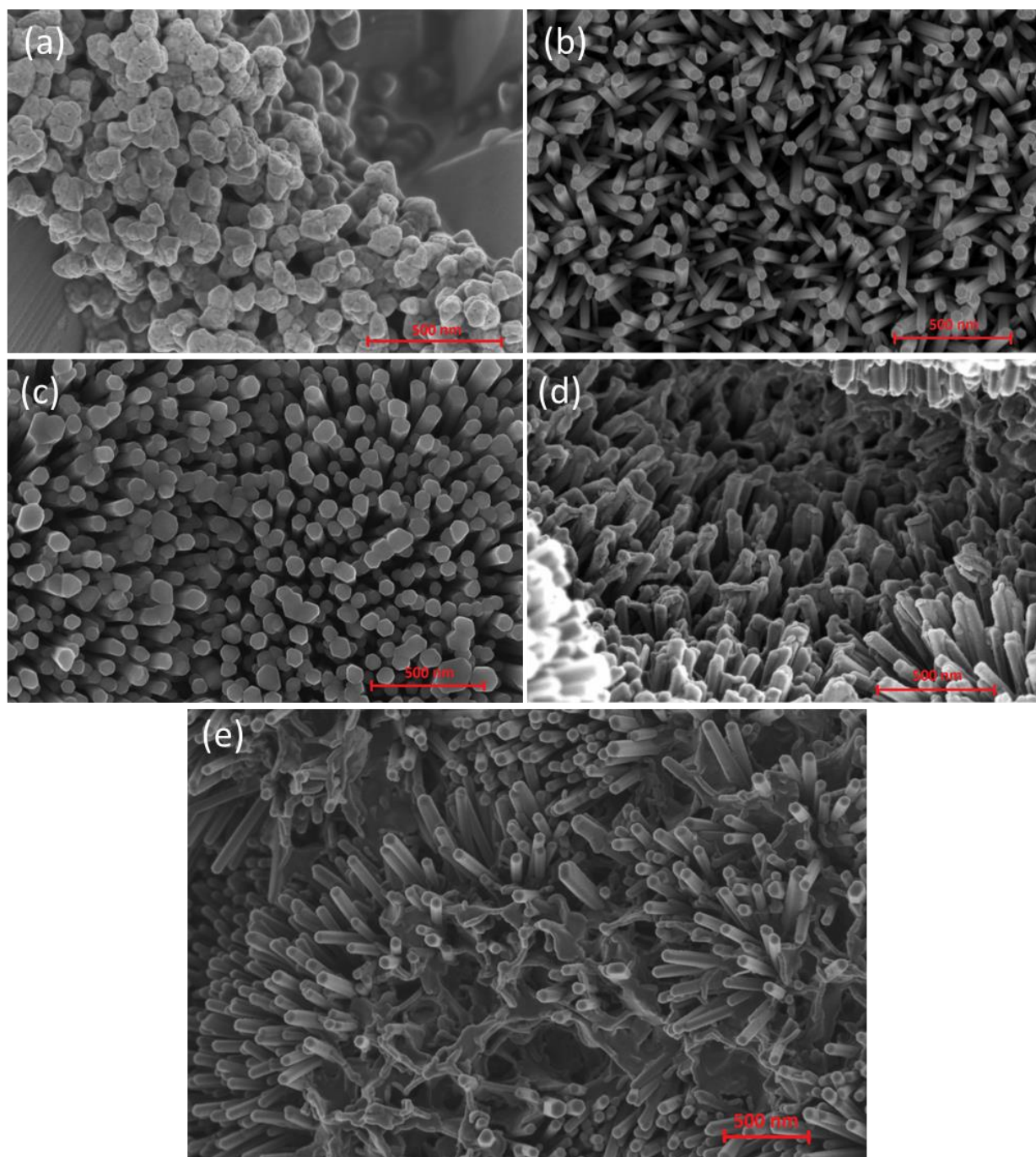
Figure 5-3: FE-SEM images of the prepared sensing material: (a) ZnO NPs, (b) bare ZnO NWs, (c) 0.01 wt% Pt-ZnO, (d) 0.1 wt% Pt-ZnO and (e) 1 wt% Pt-ZnO.

To obtain certain visual evidence of Pt NPs on the surface of ZnO NWs, HRTEM and STEM imaging were employed. The HRTEM image in Figure 5-4 shows the deposited Pt nanoparticles as dark spots for 1 wt% Pt decorated samples, indicated by red circles, dispersed semi-uniformly along the NW. The presence of Pt nanoparticles was further confirmed through HAADF STEM analysis illustrated in the inset of Figure 5-4, where Pt NPs are demonstrated with a distinct bright spot, with estimated size distribution around 1.0–5.0 nm. The advantages of the photo-deposition method for decoration of nanostructured semiconductors and conductive electrodes, compared to conventional methods such as impregnation, are well documented in the literature [120,121]. For photon mediated applications, deposition of active sites at structural defects, where the high electron density is anticipated, is highly desirable [122]. Such effective decoration can be realized through in-situ photo-deposition, resulting in selective deposition of Pt nanoparticles on the surface of ZnO NWs.
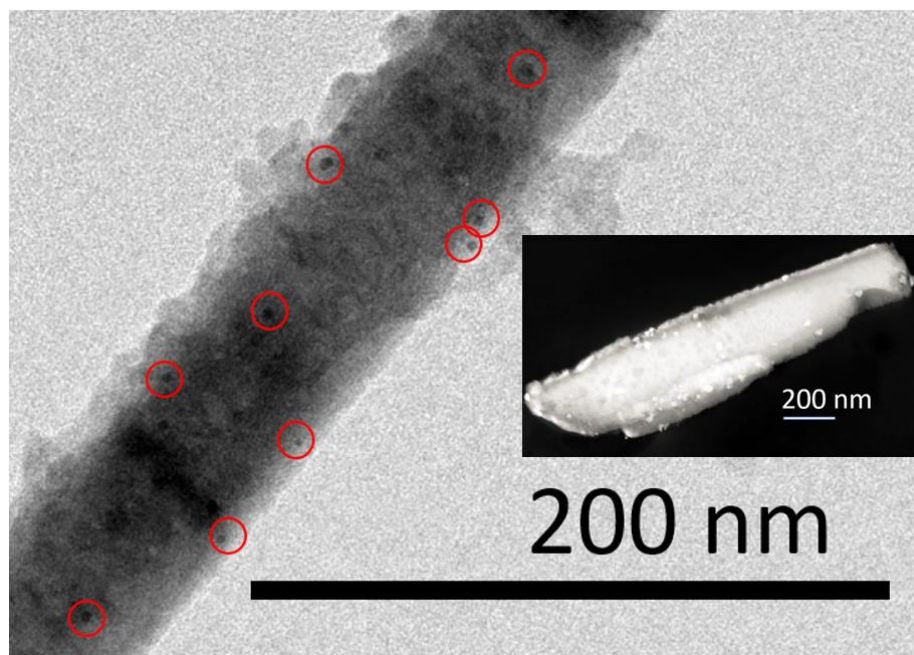
Figure 5-4: HRTEM images of ZnO NW. Red circles shows Pt NPs deposited on the surface of NWs (1 wt% Pt-ZnO NWS sample). Inset displays HAADF STEM image of a ZnO NW fragment loaded with Pt NPs, visible as bright dots.

5.3.2 Electrical properties and UV response

Several studies confirm that the gas sensing response can be affected by Ohmic contact and contacting junctions [123,124]. To understand the contribution of hetero-structural resistivity of nanomaterials in the sensing response, the resistances of the sensors were measured at room temperature before and after UV-LED irradiation in the presence of pure air (Figure 5-5a). The observed initial dark resistance of ZnO NWs was higher than that of ZnO NPs sensor, suggesting the high resistance of NWs, compared to NPs. It should be noted that a significantly large dark resistance is expected from a well-defined nanowire array. However, controlling the exposed crystallographic facets of ZnO seeds in this study results in the formation of disoriented NWs, as illustrated in Figure 5-5a, create ohmic contact over through the NWs tips, and eventually reduces the dark resistance. The higher dark resistance of ZnO NWs, compared to their NPs counterparts is likely attributed to the less electrical contacts among ZnO NWs network that are selectively grown on seeded NPs with a self-assembly technique, compared to the agglomerated regions that exist in the ZnO NPs structure.

The initial dark resistance of pristine ZnO NWs was 9×10^9 Ω. As the Pt concentration on the surface of ZnO NWs increases to 1 wt%, the layer becomes more conductive and the film dark resistance reduces to 4×10^7 Ω. The lower resistance is attributed to the higher mobility of valance electrons throughout the material, as the result of Pt nanoparticles.

Upon UV exposure, a significant resistance change was observed for ZnO NWs sensors ($\Delta R \sim 9$ MΩ), compared to ZnO NPs ($\Delta R \sim 9$ KΩ). This observed resistance change was greater for the samples with higher Pt contents. It has been shown that surface defects, such as oxygen vacancies, dominate the electronic properties and adsorption reactions of metal oxide surface [125]. Therefore, the larger change in R_a before and after UV illumination can be explained based on the number of defects in the layer, which provides suitable nucleation sites for photo-excited electrons diffusion. Thus, Pt deposition

73

increases the oxygen ions surface occupancy and results in a rapid injection of photo-excited charges to surface active sites with larger working function and subsequent reduction on favorable catalytic facets.

I-V characteristics of gas sensors are known to be a promising representative of electron density and oxygen vacant defects of nanostructures [126]. As illustrated in Figure 5-5b, the electrical current proportionally increases with Pt concentration in the samples, confirming the higher number of oxygen vacant sites. Given that the number of adsorbed oxygen ions is an indication of layer capability in adsorbing NO_2 molecules due to a higher number of active sites, we expect to observe enhanced sensing performance in ZnO NWs, especially for the ones that are loaded with Pt.
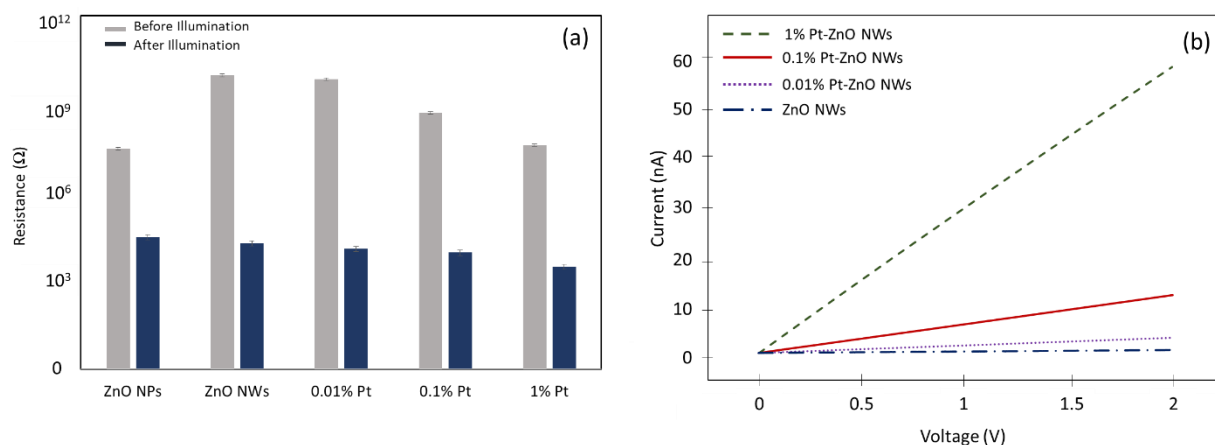
Figure 5-5: (a) Resistances of prepared sensors in the air before and after UV illumination, (b) I-V characteristics of the prepared sensors in dark condition

The photo-induced electrical behavior of ZnO NPs and pristine ZnO NWs (Figure 5-6a) was very stable before and after UV illumination. The resistance decreased 3 and 6 orders of magnitudes for ZnO NPs and ZnO NWs, respectively, and reached a plateau value after some time. However, in 1 wt% Pt loaded sample, a slight increase was observed upon UV irradiation (Figure 5-6b), which is likely related to the electron/hole recombination, and presence of precursor residues. Indeed, irradiation mobilizes the

surface electrons and results in a rapid increase in the density of charge carriers on the surface. These excited electrons are very unstable and some of them react with the available holes, resulting in a slight increase of the layer resistivity. This phenomenon was observed repeatedly in several experiments. The resistance then reached a stable value within an hour.
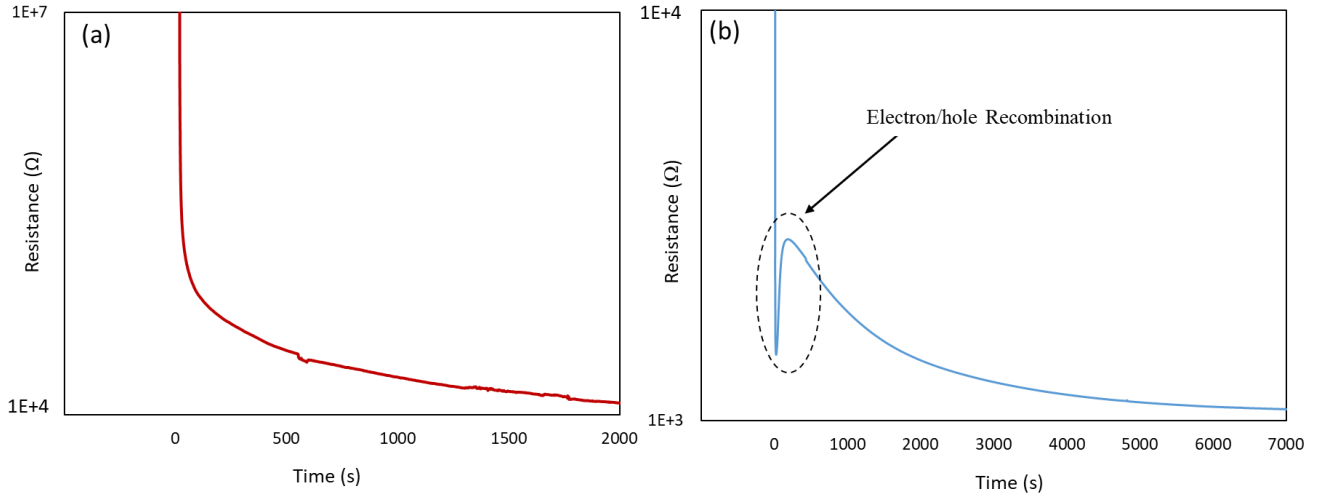
Figure 5-6: The photo-induced behavior upon UV irradiation: (a) pristine ZnO NWs (b) 1 wt% Pt-ZnO NWs. UV-LED was turned on at time near zero.

5.3.3 Photo-induced gas sensing response

The sensing performance of the developed sensors was tested against 5ppm NO_2 in the absence and presence of UV radiation at 365 nm wavelength. This wavelength was chosen based on the fact that the maximum response in UV-activated sensors can be achieved when striking photons have energy close to the bandgap of the sensing material [12,62]. The band-gap of the ZnO semiconductor is about 3.3 eV at room temperature. Therefore, the appropriate UV wavelength for gas sensing calculated by Planck's law $\lambda=1.24/E$ (where λ is the wavelength in mm and E is the band-gap energy) is around 370 nm.

In terms of gas sensing performance, no major resistance change was observed when the sensors were exposed to 5 ppm NO_2 in the absence of UV radiation. This poor response in dark condition can be

ascribed to the low carrier concentration which results in low density of adsorption sites. However, the photo-generated charge carriers under UV-LED illumination lead to a significant resistance change upon exposure to NO_2.

For a proper sensing performance in UV based gas sensors, UV-LEDs must operate at the right irradiance. Irradiance is defined as the rate of light striking the surface per unit area. It depends upon the intensity and distance of the light source and mostly affects the gas adsorption/desorption processes in sensing applications. In this study, to obtain the most appropriate UV irradiance for ZnO, the sensor response to 5ppm NO_2 was measured under several irradiances within 8–145 mW/cm^2 range. The irradiance of the UV-LED must be adjusted to provide the highest response and stability of developed sensors with shortest response time and complete recovery. Figure 5-7a shows the effect of irradiance on the response of the ZnO NPs sample. The ZnO NPs showed almost similar responses in 8 and 25 mW/cm^2. However, the response and recovery time constants under 25 mW/cm^2 irradiance were faster and more stable than that of 8 mW/cm^2. Furthermore, operation higher irradiances (i.e. 65 mW/cm^2 and 145 mW/cm^2) resulted in a lower response values. This could be due to the progressive desorption of reactants at higher irradiances that leads to a saturated surface of generated electrons with fewer numbers of sensing active sites.

Another possible explanation for the lower response values at higher irradiances could be the higher recombination rate when the density of electrons increases in the vicinity of the surface. This may disrupt the electrical double layer at the interface and eventually inject back the electrons to the bulk.

Therefore, we calculate the appropriate UV irradiance for ZnO to be 25 mW/cm^2, which gives a reasonable response time while having a fast sensor recovery. This is consistent with those optimal irradiances reported in the literature [12,43,64].

The gas sensing results under 25 mW/cm^2 against 5ppm NO$_2$ indicated that the response of ZnO NWs is almost four times greater than that of ZnO NPs samples mainly due to the higher surface area, more defect quantity and higher bulk density of charge carriers which enable the sensor to adsorb more gas molecules.

Although, the observed response of the pristine ZnO NWs against 5 ppm NO$_2$ was 1.6 (Figure 5-7b), the response time was around 300s, which is almost twice greater than that of ZnO NPs. The long response time of ZnO NWs can be attributed to the longer migration path of gas molecules to reach the active areas within the NWs structure [71].

We investigated the response of the ZnO NWs sensors loaded with different amounts of Pt to 5 ppm NO$_2$ under 25 mW/cm^2. As shown in Figure 5-7c, the response time decreased significantly to about 150s upon addition of Pt nanoparticles. However, it was revealed that the response values are highly dependent on the Pt concentration. The response of 1 wt% Pt-ZnO sample to 5 ppm NO$_2$ was 0.675 which is lower than that of pristine ZnO NWs sample. The low response can be attributed to the excessive deposition of Pt nano-particles which block of incident photons with opaque Pt nanoparticles [127]. Furthermore, the response of 0.01 wt% Pt-ZnO NWs sample was very similar to that of pristine ZnO NWs, indicating that the low concentrations of Pt would not affect the sensing response. The sensing performance of 0.1 wt% Pt-ZnO NWs to 5ppm NO$_2$ increased remarkably to 4.33, with a fast response time of about 150s. This improved response is attributed to the role of Pt in producing additional NO$_2$ adsorption sites on the ZnO surface, functioning as reduction active sites for sensing reaction. Therefore, the enhanced response to NO$_2$ can be achieved only at an optimum concentration of platinum on the surface. More experiments are required to conclude the optimum concentration with more accuracy.

A summary of the sensor responses to 5ppm NO$_2$ and 25 mW/cm^2 UV irradiation is shown in Figure 5-7d. The obtained results indicate that forming NWs structures along with the addition of appropriate

platinum concentration could result in a significant improvement in the sensor response, more than an order of magnitude, compared to ZnO NPs.
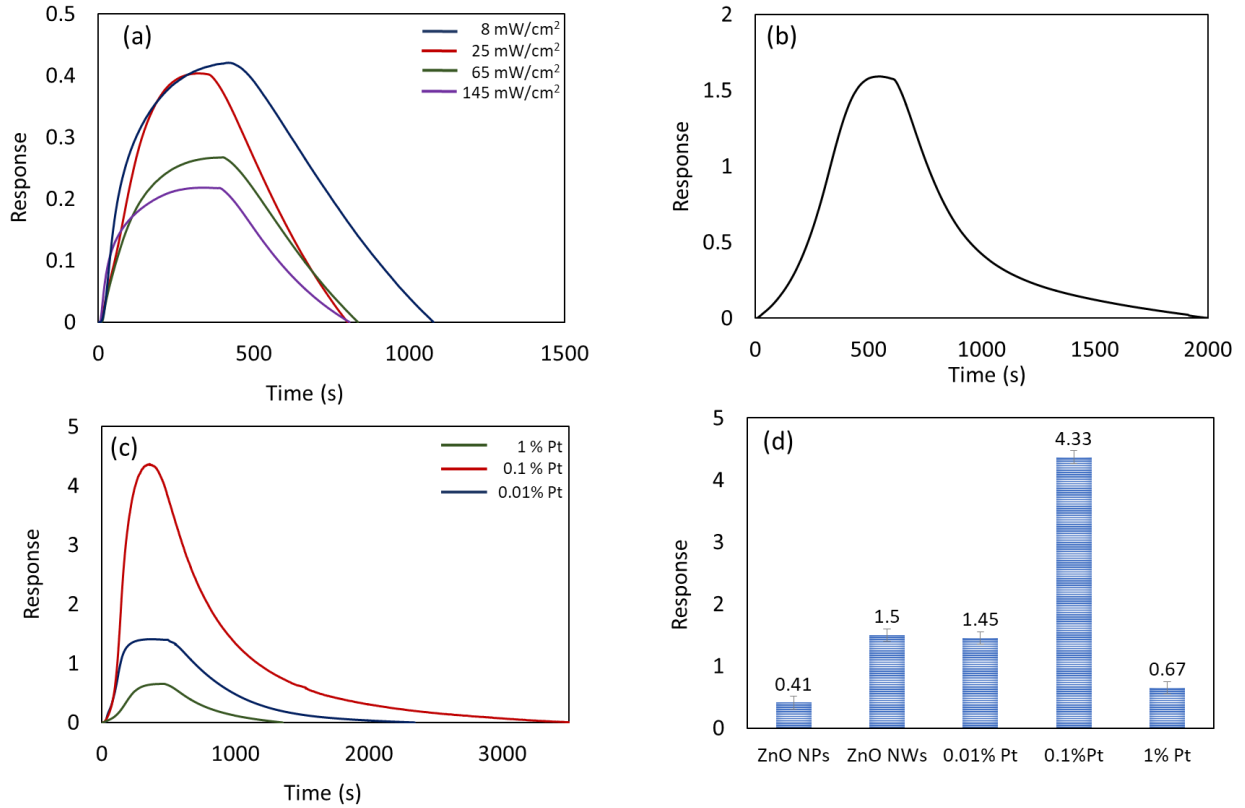
Figure 5-7: The response of the fabricated sensors to 5ppm NO_2: (a) ZnO NPs under various UV irradiances, (b) ZnO NWs under 25 mW/cm^2 (c) Pt loaded ZnO NWs with different platinum loadings and (d) a comparison of the sensors' responses under 25 mW/cm^2

There are several research reports in the literature on the photo-activated NO_2 gas sensing. Table 1 summarizes the highlight of the results reported in the literature and compares the responses with the 0.1 wt% Pt loaded ZnO NWs sensor response of this study. To the best of our knowledge, the sensing material synthesized in the present work shows the highest response under UV irradiation.

Table 5-1: Comparison of the NO_2 response of the 0.1 wt% Pt-ZnO NWs sensor prepared in this study with those reported in the literature under UV-LED irradiation.

Sensing Material	Detection Concentration (ppm)	UV wavelength (nm)	Irradiance (mW/cm^2)	Response $(\Delta R/Ra)$	Reference
Pt-ZnO NWs	5	365	25	4.33	This Study
100 nm wide line ZnO	20	365	25	0.83	[64]
Au–ZnO	5	365	1.2	3.55	[128]
MoS_2	5	400	-	4	[129]
MoS_2–ZnO NWs	0.1	365	-	0.5	[130]
MoS_2	100	365	2	0.3	[131]
Thin film ZnO	5	365	-	0.08	[62]
SnO_2 nanowires	10	338	-	0.8	[69]
Mesoporous In_2O_3	5	400	-	1.9	[132]
Al/TiO_2/Al_2O_3/P-Si	20	365	-	0.11	[133]

To evaluate the sensors' stability, the sensing performances of the sensors to 5 ppm NO_2 were measured repeatedly under the same operating conditions. The results confirmed that the responses are quite stable and reproducible. As illustrated in Figure 5-8, the selectivity of the prepared 0.1 wt% Pt-ZnO NWs and ZnO NPs sensors were also evaluated against interfering gases such as Ammonia (NH_3) and Carbon Monoxide (CO). The experiments were performed under the same irradiation condition (365 nm wavelength and 25 mW/cm^2 irradiance). Despite higher concentration of CO (50 ppm) and NH_3 (50 ppm), compared to NO_2 (5 ppm), the UV activated sensors showed higher selectivity to NO_2. No response was observed against CO for both sensors. Decorating sensing material with Pt nanoparticles

could enhance the response to NH_3 (0.71), compared to ZnO NPs sensors (0.18), but it is still lower than that of NO_2 (4.33).
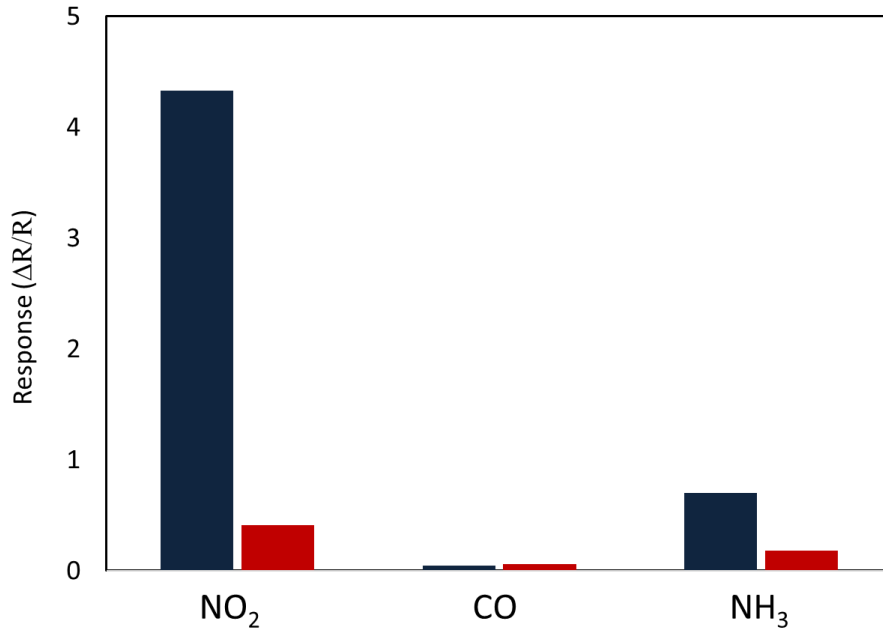
Figure 5-8: The response of the 0.1 wt% Pt-ZnO NWs sensor to 5 ppm NO_2, 50 ppm CO and 50 ppm NH_3

5.3.4   Enhancing gas sensing characteristics using Pt/ZnO NWs

In general, the participation of larger amount of photo-generated electrons in Pt-loaded samples was in charge of gas-surface interaction improvements (Figure 5-9). Also, using density functional theory, it has been reported that the adsorption energy of NO_2 gas molecules on the oxygen-vacant sites of ZnO surface is around $E_{ad}=-0.98$ eV. This energy is three times greater than that of vacant free ZnO layer ($E_{ad}=-0.30$ eV). Therefore, the charge transfer from the oxygen-vacant sites to NO_2 adsorbate is much larger than that of a vacant-free sample [126,134]. This means that oxygen vacancies provide effective bindings with NO_2 molecules through attracting more charges from ZnO surface, compared to the oxygen-vacant-free ZnO surface. Based on this concept, the substantial improvement in the sensor

response of the Pt loaded sensor may be attributed to the more oxygen vacancies that act as preferential adsorption sites for NO_2 molecules.
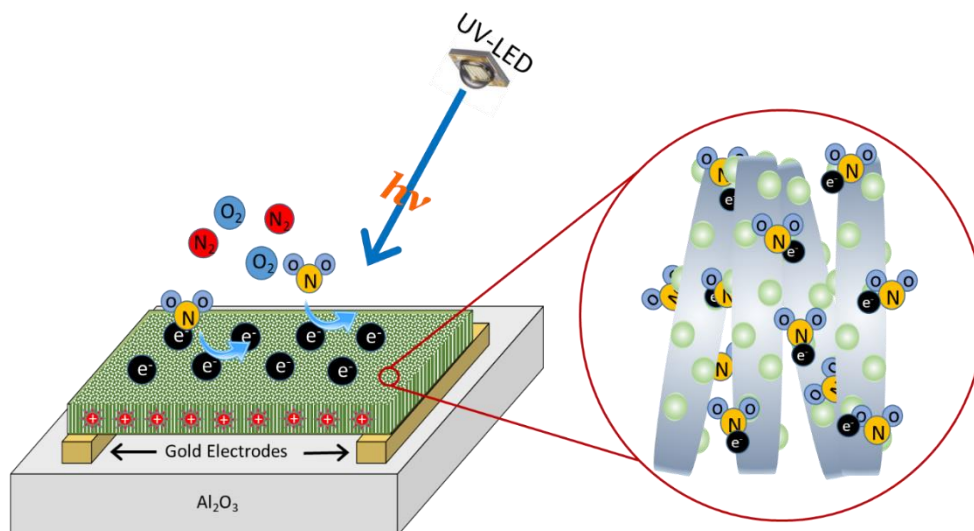
Figure 5-9: A schematic illustration of the detection mechanism of UV-LED activated ZnO NWs sensors. Nano-wires provide higher surface area and enhance the adsorption capability of the sensing layer.

In conclusion, Pt-loading in a controlled concentration (i.e. 0.1 wt%) increases the response of the sensor to about 4.33 against 5 ppm NO_2 response under 25 mW/cm^2 UV-LED irradiation with 365nm wavelength. Metal loading also shortens the response time to about 140s, which is 50s faster than that of bare ZnO sample. This improvement in response characteristic may be attributed to the more oxygen vacancies and larger amount of photo-generated electrons in Pt-loaded sensing materials.

Chapter 6: **Synthesis and performance evaluation of photo-activated ZnO-In$_2$O$_3$ and ZnO-SnO$_2$ core–shell nanowires**

6.1 Introduction

Hetero-structured one-dimensional (1D) nanomaterials, i.e. core-shell nanowires, have received intensive attention in the past years as potential building blocks for catalysts, pharmaceuticals, gas sensors and biosensors [135,136]. This is due to their unique properties arising from the layer structure and the interconnected junctions, which give more versatile functions compared with monolithic nanomaterials [137]. Developing high-temperature chemical sensors based on the core-shell nanowires has been investigated recently [138,139]. Studies confirm that using coaxial nanowire-based gas sensors may enhance both receptor and transducer functions, thus providing a superior response, compared to a pristine nanowires sensor. However, only a few works on the core-shell nanostructures in photo-activated gas sensors have been published.

The improved performance in core-shell 1D structures can be attributed to the intrinsic and synergistic effects of the single-crystalline core nanowires and polycrystalline shell thin films. The rationale of this combination is to maximize efficiency by integrating highly reactive metal oxides and base material with high electron mobility and large surface-to-volume ratio [138]. In other words, the outer shell layer facilitates adsorption through providing more active sites and promoting bonding with gas molecules, thus enhancing the receptor function. While the single crystalline inner core material allows fast transport of charge carriers during the interaction with gas molecules, thus enhancing the transducer function [140]. The high electron mobility within the core material can reduce the charge recombination at the interface.

In the present study, we have prepared single-crystal ZnO nanowires by a hydrothermal method as a base template, and have deposited a thin semiconductor shell layer of In_2O_3 or SnO_2 by dip-coating. The as-prepared core-shell structures were then used as chemical gas sensors in photo-activation mode, and the sensing properties of nanowires with and without shell materials have been compared.

6.2 Material preparation

The synthesis of the core-shell NWs array films was carried out by a two-step process: hydrothermal synthesis of the base ZnO NW arrays and dip-coating deposition of In_2O_3 and SnO_2 shell layers. A schematic illustration of the fabricating process is shown in Figure 6-1.

ZnO NWs: As demonstrated earlier, an alumina substrate was seeded with ZnO nanoparticles (NPs) by spin-coating method. To grow nanowires, the seeded substrate was placed in a solution containing $Zn(NO_3)_2.xH_2O$ and Hexamethylenetetramine (HMT). The hydrothermal growth process was conducted at 93 ^{o}C for 6 h. The obtained NWs were washed with pure water and ethanol and subsequently annealed in a furnace at 350 ^{o}C for 30 min. After the preparation of the core ZnO nanowires, the shell layer was deposited by dip-coating method.

ZnO-In$_2$O$_3$ Core-shell nanowires: To prepare the precursor solution of In_2O_3, 1.5 ml ammonium hydroxide solution (25%) was added dropwise to a solution containing 0.01 mol indium (III) chloride hydrate ($InCl_3 \cdot 5H_2O$), 2 ml acetylacetone and 50 ml ethanol [141]. The amount of the incorporated In_2O_3 was controlled by the number and speed of dip-coating cycles. The ZnO NWs were dip-coated by submerging the sensor once, with a speed of 5 cm/min, in the as-prepared shell material sol, and subsequent calcination at 500 °C for 1 h.

ZnO-SnO$_2$ Core-shell nanowires: The SnO_2 precursor colloid was prepared by refluxing a mixed solution of 0.5 M tin dichloride in 100 mL ethanol at 90 °C for 10 h. The yellowish SnO_2 colloid was

83

then coated on the ZnO nanowires through the same dip-coating process, followed by annealing at 500 °C for 1 h [142].

Figure 6-1: Schematic illustration of the core-shell nanowires synthesis process

6.3 Results and discussion

6.3.1 Composition, morphology and crystal structure

FE-SEM images shown in Figure 6-2 demonstrate the typical morphology of ZnO NWs which serves as core in the hetero-structure as well as ZnO-In$_2$O$_3$ and ZnO-SnO$_2$ core-shell samples. The as-prepared ZnO nanowires (Figure 6-2a) were found to be single crystalline hexagonal shapes with an average diameter of ~100 nm and a length of 1–2 μm, evenly distributed on the alumina substrate. A grainy polycrystalline In$_2$O$_3$ and SnO$_2$ shell layers covering the nanowire core can be observed in Figures 6-2(b) and 6-2(c), respectively. The presence of Zn, In, Sn and O were confirmed by the broad area energy dispersive X-ray spectroscopy (EDS) on the as-grown samples.

Several attempts were carried out, with various dipping cycles and speeds, to deposit the shell materials. Initially, the samples were dipped into the shell solution at a slower rate and for several times, which resulted in excessive loading of the shell material. Some of the FE-SEM images and XRD results of the initial trials have been presented in the Appendix A.3, showing the buried ZnO NWs in the second semiconductor.
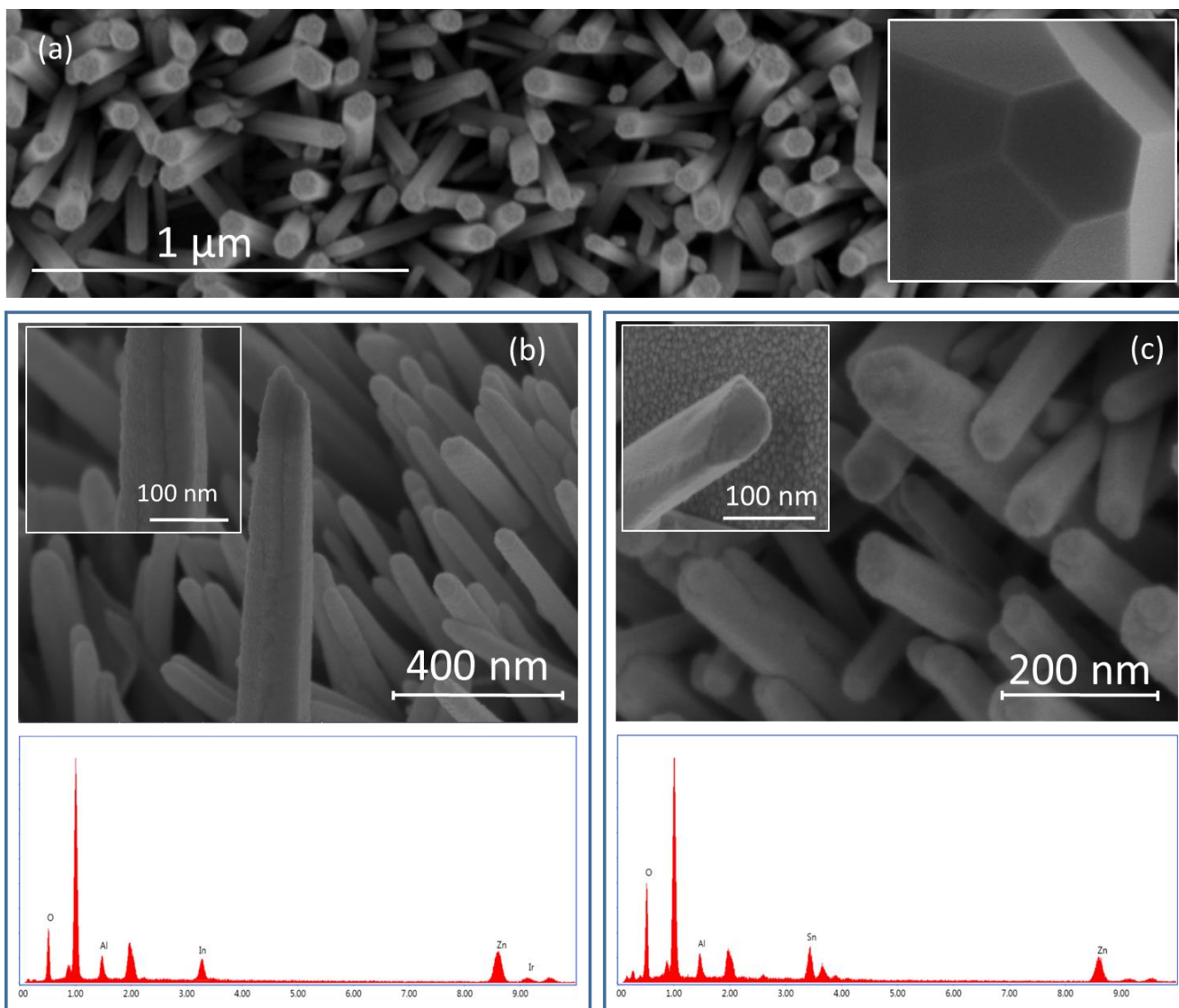
Figure 6-2: FE-SEM and EDS analyses of the prepared (a) hexagonal ZnO NWs, (b) ZnO-In$_2$O$_3$ and (c) ZnO-SnO$_2$ core-shell nanowires

Detailed studies of the crystal structure and morphology of the core-shell nanowires were performed by TEM analysis. Figure 6-3(a) and Figure 6-3(b) depict the HRTEM images of ZnO-In$_2$O$_3$ and ZnO-SnO$_2$, respectively.
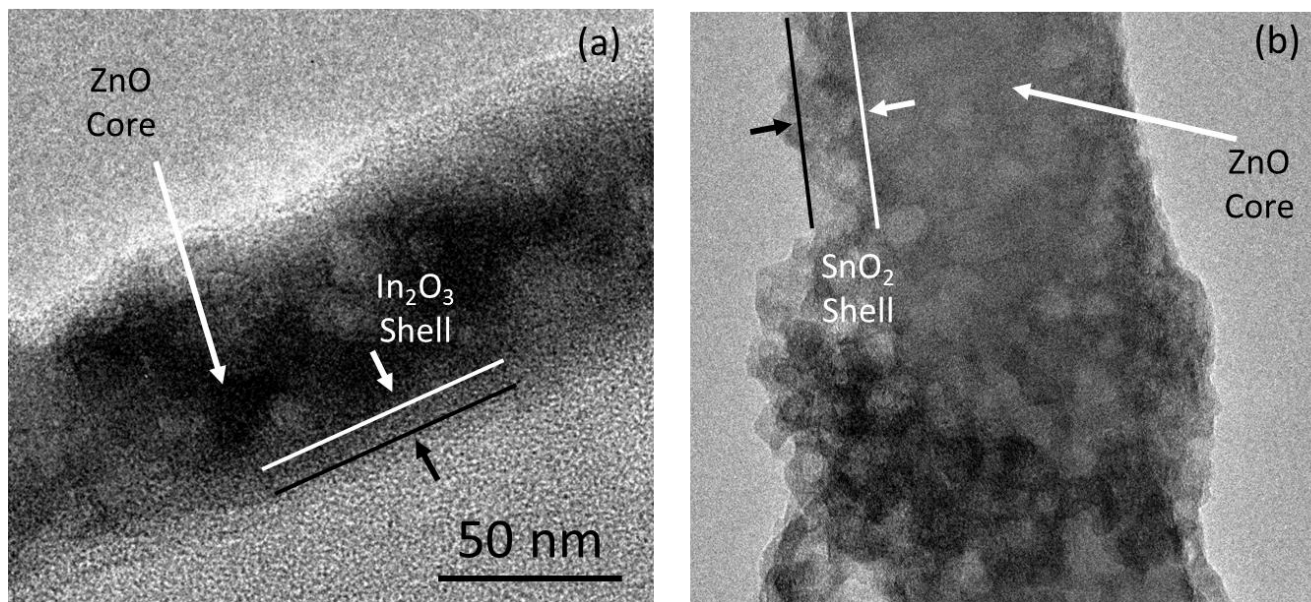
Figure 6-3: HRTEM images of the as-prepared ZnO-In$_2$O$_3$ and ZnO-SnO$_2$ core/shell nanowires

The phase composition, purity, and crystallinity of the as-synthesized samples were analyzed by XRD. Figure 6-4 shows the XRD patterns of the ZnO NWs, ZnO-In$_2$O$_3$, and ZnO-SnO$_2$ core-sell structures. It can be observed that the ZnO nanowire arrays are preferentially oriented along the c-axis direction (002). The peaks associated with In$_2$O$_3$ (222) and SnO$_2$ (110 and 101) shell layers have relatively lower intensity, compared to base ZnO NWs peaks.
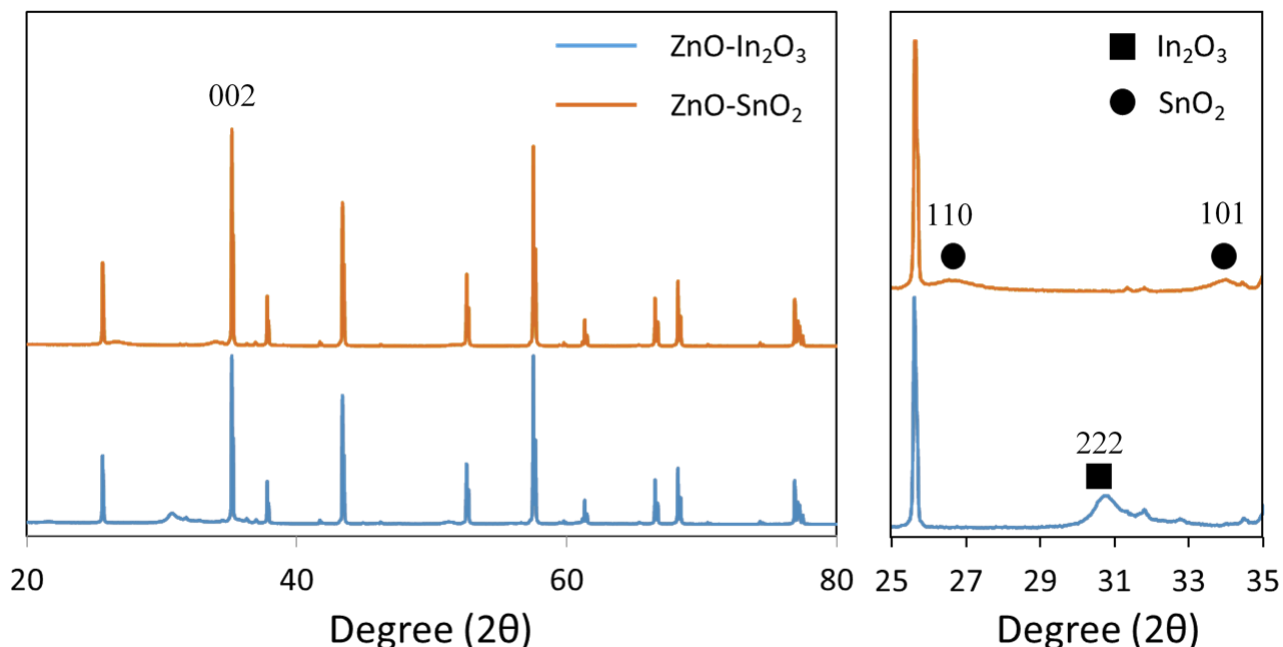
Figure 6-4: XRD patterns of ZnO-In$_2$O$_3$ and ZnO-SnO$_2$ NWs sensors, confirming a thin layer of crystalline In$_2$O$_3$ (222) and SnO$_2$ (110 and 101) layer

6.4 Sensing performance

Figure 6-5 shows the sensing performance of the developed core-shell structure sensors to 5 ppm NO$_2$ at 25 mW/cm^2 UV irradiation. As the sensors were exposed to the continuous flow of NO$_2$, the response increased until it reached a nearly plateau value. When the chamber was evacuated from the target gas, the resistance decreased to its initial value in the presence of pure air. As shown in Figure 6-5, the relative responses of the ZnO-In$_2$O$_3$ (2.49) and ZnO-SnO$_2$ (2.21) sensors were higher than that of pristine ZnO NWs (1.6). Excessive shell coating, however, introduces additional grain boundaries and increases the charge transfer resistance, resulting in lower carrier separation efficiency.

The enhancement of the photo-induced sensing response of ZnO-In$_2$O$_3$ and ZnO-SnO$_2$ sensors, compared to pristine ZnO nanowires, may be attributed to the improved photon absorption, electron utilization and more active sites on the surface of the nanowires [141]. The electrons in the shell material

can be easily excited by striking photons due to the higher number of defects in the polycrystalline shell structure, compare to pristine NWs, which subsequently improves the surface interactions. The electron exchange with the adsorbed gas molecules affects the charge balance on the surface. Due to the high electron mobility and ideal geometry of the vertical-aligned core-shell nanowires, the unbalanced electrons are effectively collected by the core. This separation of charge carriers suppresses the rate of hole–electron recombination, which effectively improves the photo-electrochemical behavior of the sensor.

Surface acidity or basicity can also change the catalytic behaviour of the surface and influence the reaction directions in response. For metal oxides acidity and basicity are dependent on the charge and the radius of the metal ions as well as the character of the metal-oxygen bond. Structural defects can greatly contribute to the acidity or basicity as sites of high unsaturation can occur from oxygen or metal ion vacancies. The incorporation of In_2O_3 and SnO_2 as shell materials highly affects the surface acidity/basicity, thus enhancing the catalytic properties of the nanowires, resulting in improved interaction with the gas molecules.
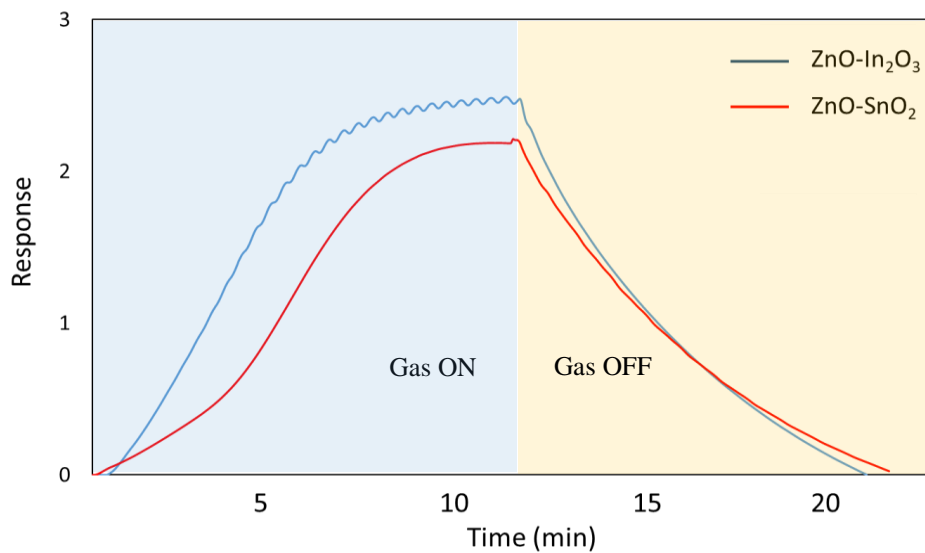
Figure 6-5: The transient response of core-shell structures to 5 ppm NO_2

One of the most important parameters in any sensor setup is the ability to accurately detect and measure a wide range of concentrations of the target gas. Figure 6-6 shows the response of developed sensors in the 5–40 ppm NO_2 concentration range. The results confirm that the ZnO-In_2O_3 sensor still has a higher response, compared to ZnO-SnO_2, in the experimented concentration range. The slope of the increased response was greater in lower concentrations and decreased as the concentration approached the upper level. The increased response at higher concentrations is mainly because of the larger number of electrons that are involved in the surface reactions, which results in higher band bending and more resistance variation.
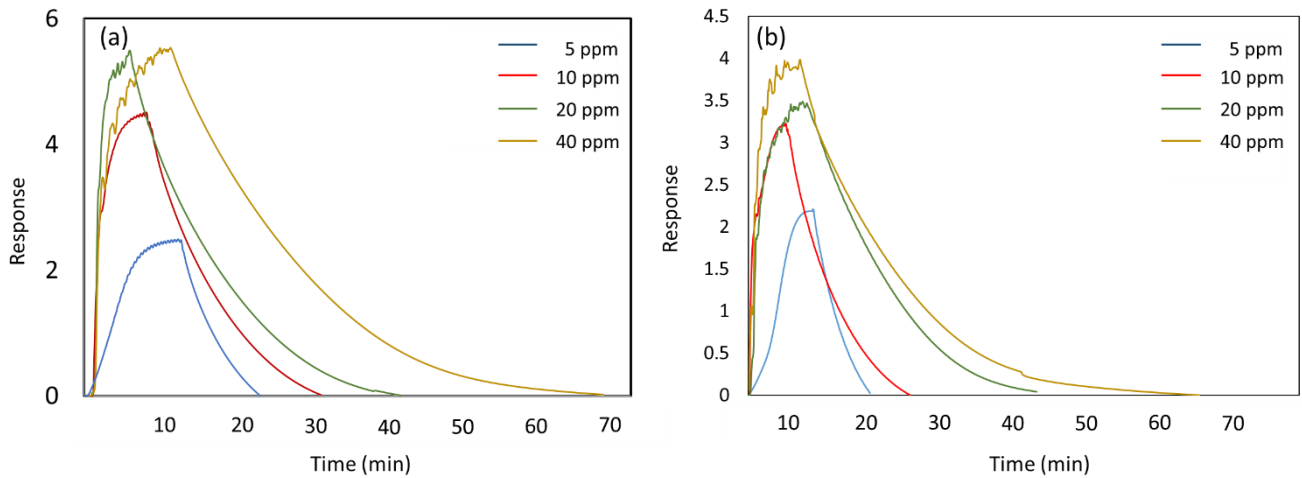
Figure 6-6: The response of the (a) ZnO-In_2O_3 and (b) ZnO-SnO_2 core-shell sensors to different concentrations of NO_2

It is evident from Figure 6-6 that the response and recovery times are also a function of concentration. Response time decreases while recovery time increases at higher concentrations. As NO_2 is highly reactive, all the NO_2 molecules that diffuse into the film are immediately oxidized and hence, there is no concentration build-up. Consequently, higher concentration allows for a faster diffusion rate due to the

higher driving force. Following the surface reactions, the products do not leave the sensor surface immediately. Thus, the desorption of gas molecules is delayed, resulting in longer recovery time.

6.5   Sensing improvement using core-shell nanowires

In pristine ZnO nanowires, homo-interfaces are only present at the junctions, while in the core-shell structures, combinations of homo and hetero-interfaces can exist which provide additional energy barrier at the junctions, augmenting the resistance changes in the presence of gas molecules (Figure 6-7). As discussed in Chapter 1, electron-hole pairs are generated upon UV irradiation, and a depletion layer is formed at the interface due to gas adsorption. The thickness of the depletion layer plays a crucial role in the charge carrier transport between active spots and gas molecules.

In nanowires structures, the electrons travel in percolation paths through multiple nano-junctions with a potential barrier at each junction. Surface states, oxygen vacancies and the depletion layer on the nanowire surface determine the height of the potential barrier at the homo-junctions. In hetero-junctions (i.e. core-shells), however, the potential barrier depends on the work function and band-gap differences between the two materials [140]. Due to the differences in the work function of the core and shell materials, an additional electron depletion layer forms at the interface of core-shell nanowires structures. If the shell layer is too thin, it may get fully depleted.

In the ZnO-In_2O_3 and ZnO-SnO_2 core-shell sensors, there are three energy barriers, consisting of two barriers at the hetero-interfaces between the two semiconductors and one at the homo-interface between the polycrystalline shell layers on the nearby nanowires. In pristine ZnO nanowires, the relative change in the resistance (sensor response) is limited by the modulation of the surface depletion layer, leading to a lower response. In core-shell nanowires, however, the polycrystalline shell layer provides more potential barriers to be modulated, thus creating more adsorption sites. The combined effect of the

90

inherent surface properties of polycrystalline shell layer and modulation of potential barriers on the percolation path upon gas exposure, determine the sensor response. Therefore, a significant enhancement in the sensor response can be achieved by adding a polycrystalline shell material on a nanowire core.
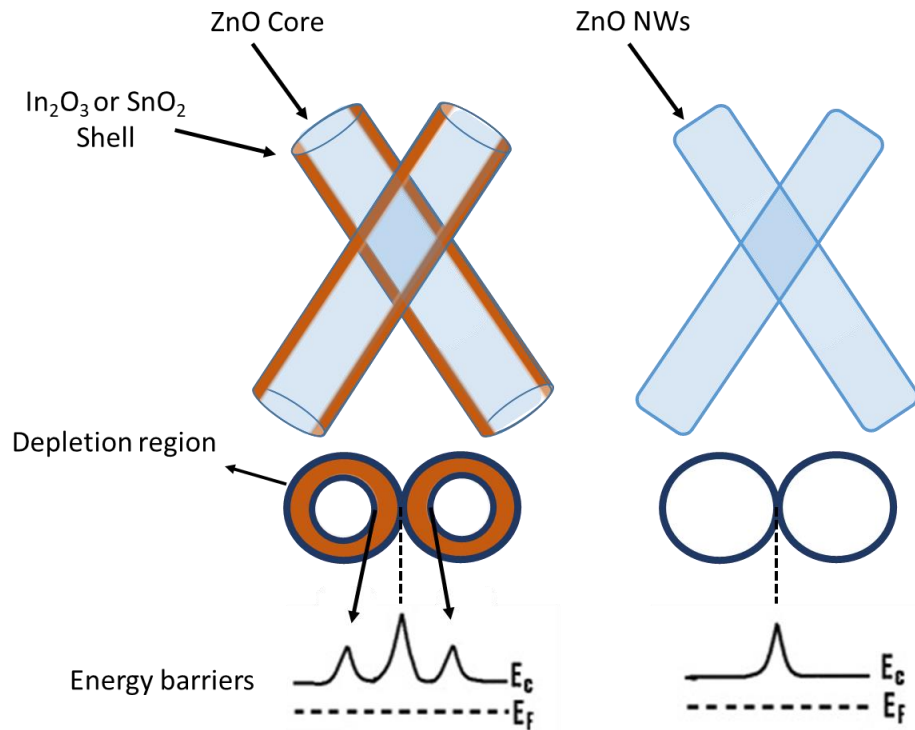
Figure 6-7: Illustration of the charge transport through hetero-structured core–shell nanowire junction with two depletion regions and formation of three energy barriers at the interfaces.

In conclusion, the results presented in this chapter indicate that incorporating a polycrystalline shell material on a core semiconductor may produce a more sensitive gas detector. It is believed that ZnO facilitates the flow of charge carriers, while In_2O_3 and SnO_2 shell layers enhance chemisorption ability in the structure. A combination of these two phenomena leads to the synergistic effect of the core-shell sensor with superior performance.

Chapter 7: **Synthesis and performance evaluation of photo-activated ZnO nanoparticles on ordered carbon mesoporous materials**

7.1 Introduction

To develop sensitive sensors, efforts have been made to prepare highly engineered sensing materials that have high surface areas and high carrier mobility. It has been recently shown that gas sensors based on mesoporous sensing layers show superior responses to a variety of gases, compared to non-porous metal oxides, mainly due to their large specific surface areas [143–145]. Ordered carbon mesoporous materials (CMMs), such as CMK series materials, have specifically gained attention as catalyst supports due to their ordered hexagonal pore structure, narrow pore size distribution, and high-specific surface area [143,146–150]. Therefore, coupling the mesoporous carbon materials with a sensitive nanostructured semiconductor may help to promote electron-transfer reactions, thus enhancing sensing responses. Wide band-gap, large exciton binding energy and fast carrier transport kinetics of ZnO induce exceptional opto-electrical properties and make it a promising candidate for sensing applications [99,151]. A ZnO layer with high surface/volume ratio possesses more chemically active sites and shows improved performance towards sensing and catalytic applications.

This study is the first, to the best of our knowledge, to investigate the UV-activated metal oxide materials on ordered CMMs for gas sensing application. In this research, we demonstrate the high sensitive UV-LED activated ZnO/CMK-3 hybrid gas sensor, where CMK-3 is a representative of ordered CMMs with 2D hexagonal and high specific surface area (> 1000 m^2/g). Owing to the synergistic effects of structural, optical and electronic properties of sensing material components, significantly higher responses were achieved, compared to pristine ZnO nanoparticles.

7.2 Material preparation

7.2.1 Preparation of carbon mesoporous supporting material, CMK-3

The CMK-3 was prepared using mesoporous silica SBA-15 as a sacrificial template, where SBA-15 was prepared using a previously reported method [146]. In this research, P123 surfactant was used for the synthesis of mesoporous materials. Pluronic P123 surfactant is a symmetric triblock copolymer comprising poly-ethylene oxide and poly-propylene oxide in an alternating linear fashion. Its behavior is similar to hydrocarbon surfactant, and will form micelles when placed in a selective solvent such as water. As shown in Figure 7-1, in a typical synthesis process, 2.3 g of silica source (tetraethyl orthosilicate, $\geqq$99.0%, Aldrich) was added to a mixture solution containing HCl (8.0 g, 37% HCl), H_2O (30.0 g) and a triblock co-polymersurfactant (1.0 g, P123; Acros). The prepared mixture was stirred under 313 K for 2 h and the solution was then aged at 373 K for 48 h. After washing, drying, and calcination in air at 833 K for 6 h, the SBA-15 powders were collected for subsequent CMK-3 preparation. In the second step, SBA-15 was impregnated with a sucrose/H_2SO_4/H_2O solution with a weight ratio of 1.25:0.14:5 (sucrose/H_2SO_4/H_2O) by capillary absorption. The wet powders were then dried at 333 K for 6 h and dehydrated at 433 K for 6 h. The resultant dark brown powders were carbonized under an anaerobic environment at 1173 K for 1 h. Finally, CMK-3 powders constructed with carbon meso-rods and carbon micro-rods were collected after SBA-15 removal in 1 M HF (Acros; 48–51%) solution.

7.2.2 Preparation of ZnO$_x$/CMK-3 composite materials

ZnO$_x$/CMK-3 composites, where the subscript x represents the ZnO content (wt%), adopted as active materials for detecting target gases were prepared by the following steps. First, zinc nitrate hexahydrate precursor was dissolved in desired concentration in pure ethanol. Then, the previously prepared CMK-3

was added to the solution and stirred for 1 h to obtain a uniform slurry. Subsequently, the slurry was dried in 343K, ground and decomposed under air at 523K for 2 h. For further comparison, a pure ZnO sample (ZnO_{100}) was also prepared by precipitation of zinc nitrate hexahydrate with ammonia solution. The sample designation and materials characterizations are depicted in Table 1.
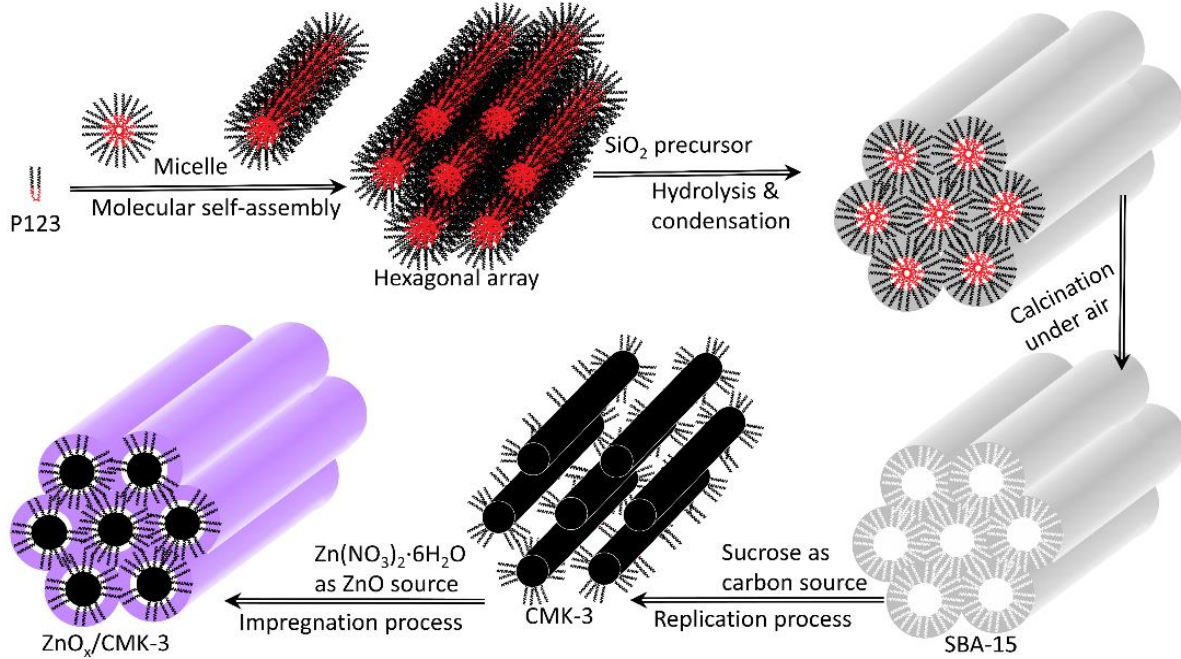
Figure 7-1: Schematic drawing of synthesis process of ZnO_x/CMK-3.

7.2.3   Characterization

The morphology and microstructures of the gas sensing materials were examined by scanning electron microscopy (SEM, JSM-7100F) and transmission electron microscopy (TEM, JEOL JEM-2100, 200 keV), respectively. X-ray diffraction (XRD) analyses (PANalytical X'Pert PRO, CuKα radiation, $\lambda = 0.1541$ nm) were used to determine the pore structure, crystallinity, and grain size of ZnO. Scherrer's equation (Eq. (2)) was used to calculate the average grain size (AGS) of ZnO, where k is a coefficient (0.9), λ is the wavelength (nm) of the X-rays used, β is the FWHM of the respective diffraction peak in

radians, and θ is the angle corresponding to the peak maximum. The Brunauer-Emmett-Teller (BET) surface areas of the samples were derived using the N_2 adsorption/desorption analysis under 77 K (Micromeritics; ASAP2020).

$$AGS\ (nm) = \frac{k\lambda}{\beta cos\theta} \qquad (13)$$

7.3 Results and discussion

7.3.1 Morphology and microstructure analyses

The SEM images (Figure 7-2) show the morphology of pristine CMK-3 and ZnO_x/CMK-3, where x is from 13 to 85. As is shown in figure 7-2(a-d), ZnO_x/CMK-3 sensors have similar morphology up to 44 wt% ZnO concentration. This could possibly mean that almost all ZnO-NPs have been formed in the CMK-3 framework in such concentrations. However, further addition of ZnO (i.e. ZnO_{57}/CMK-3), leads to precipitation of ZnO nanoparticles outside the CMK-3 structure (Figure 7-2(f-h)). Figure 7-2(i) shows the agglomerated nano-sized ZnO particles in pseudo-spherical shapes with the average grain size of 40 nm.
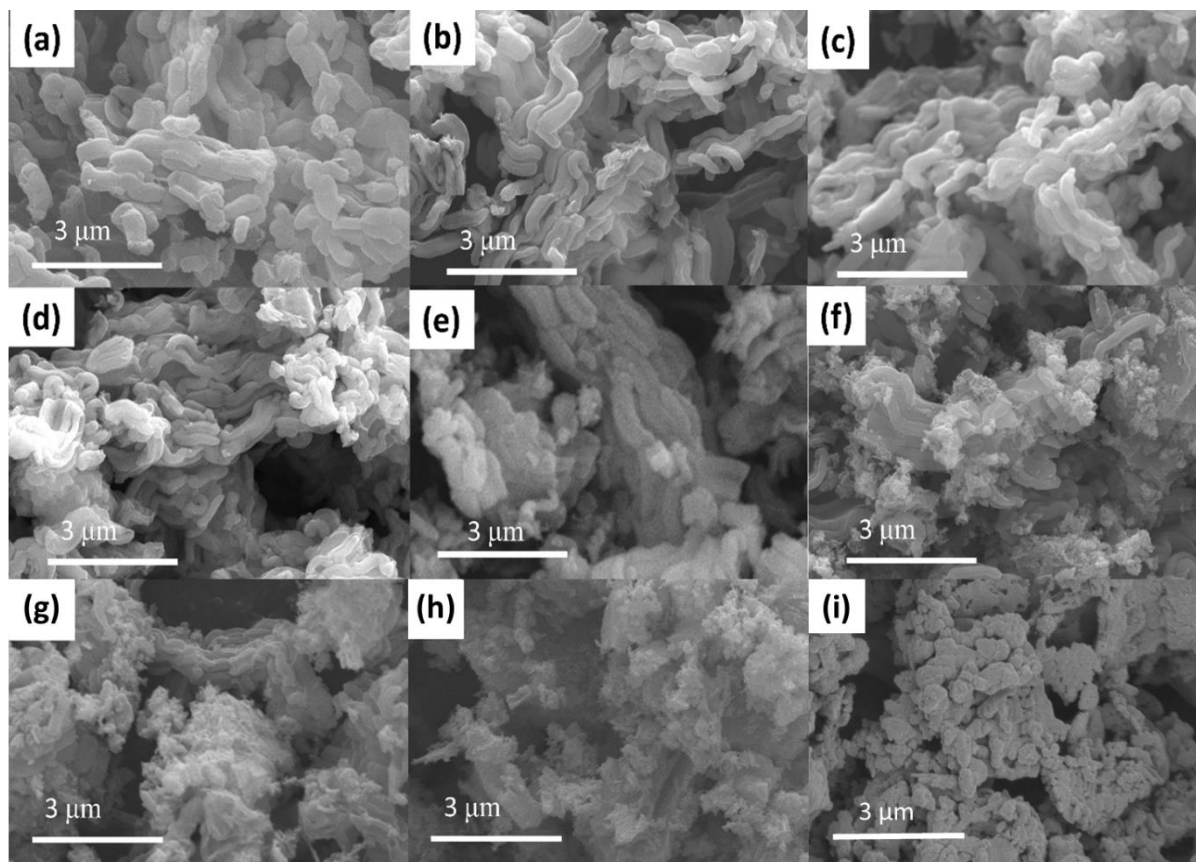
Figure 7-2: SEM images of (a) pristine CMK-3; ZnO_x/CMK-3 with (b) 13, (c) 27, (d) 44, (e) 49, (f) 57, (g) 70, (h) 85 wt% ZnO , and (i) pristine ZnO nanoparticles

TEM images of CMK-3 and ZnO_{57}/CMK-3 are shown in Figure 7-3, corresponding to Figure 7-3(a) and 6-3f, respectively. The 2-D hexagonal mesoporous structure of CMK-3 constructed by carbon rods is evident in Figure 7-3(a). After being loaded with ZnO, no mesopore could be found in the TEM images, and the exceeding ZnO nanostructures precipitated on the outside of the CMK-3 framework (Figure 7-3(b)). The results are in good agreement with the SEM images.
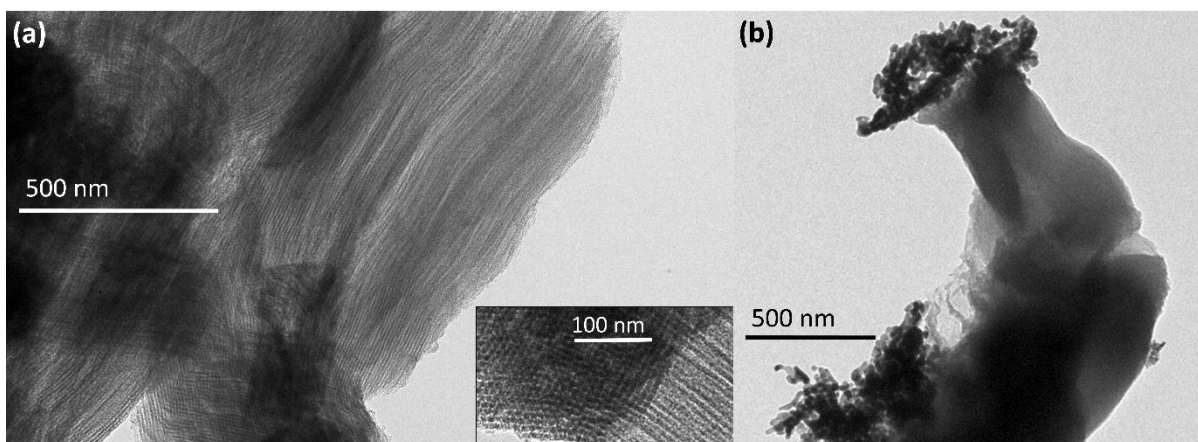
Figure 7-3: TEM images of (a) CMK-3 (side view) and its cross-section view (inset), and (b) the ZnO_{57}/CMK-3 (side view).

As demonstrated in Figure 7-4(a), the low angle XRD of SBA-15, CMK-3 and ZnO_x/CMK-3 samples show the ordered mesostructured ZnO. The weak (100) diffraction peak of ZnO_{57}/CMK-3 suggests that CMK-3 has been filled with ZnO nanoparticles. The specific surface area and t-plot micropore surface area of ZnO_x/CMK-3 (as shown in Table 1) decline with increasing ZnO content. However, the specific surface area is still significantly larger than that of ZnO nanoparticles (about several tens m^2/g [152]) until 57 wt% ZnO loading. Besides, there is still considerable slit-type micropore surface area in the ZnO_{57}/CMK-3 (as discussed in section Appendix A.4). It hints that further addition of ZnO would gradually fill the entire micropores and possibly block the active sites.

Figure 7-4(b) compares the XRD patterns of ZnO_x/CMK-3 samples with different loading concentrations and confirms the crystalline hexagonal wurtzite phase of ZnO which is in agreement with JCPDS card No. 00-036-1451. Figure 7-4(c) also shows the corresponding (102) and (110) peaks for AGS calculation. As shown in Table 1, the AGS of ZnO on ZnO_x/CMK-3 are between 9 and 11 nm, where x is from 13 to 57. Further increase in ZnO content (x=70) would dramatically increase the AGS (16 nm) which may consequently inhibit the gas sensing response. For instance, ZnO_{85}/CMK-3 exhibits

97

greater AGS; therefore its sensing response may decline. In addition to the BET surface areas, pore size, and micropore surface area of the prepared samples, which are depicted in Table 1, N_2 adsorption/desorption isotherms have also been provided in the Appendix A.4 (Figure A4-1). Both BET surface area and t-plot micropore surface areas are decreasing as the ZnO content is increased.
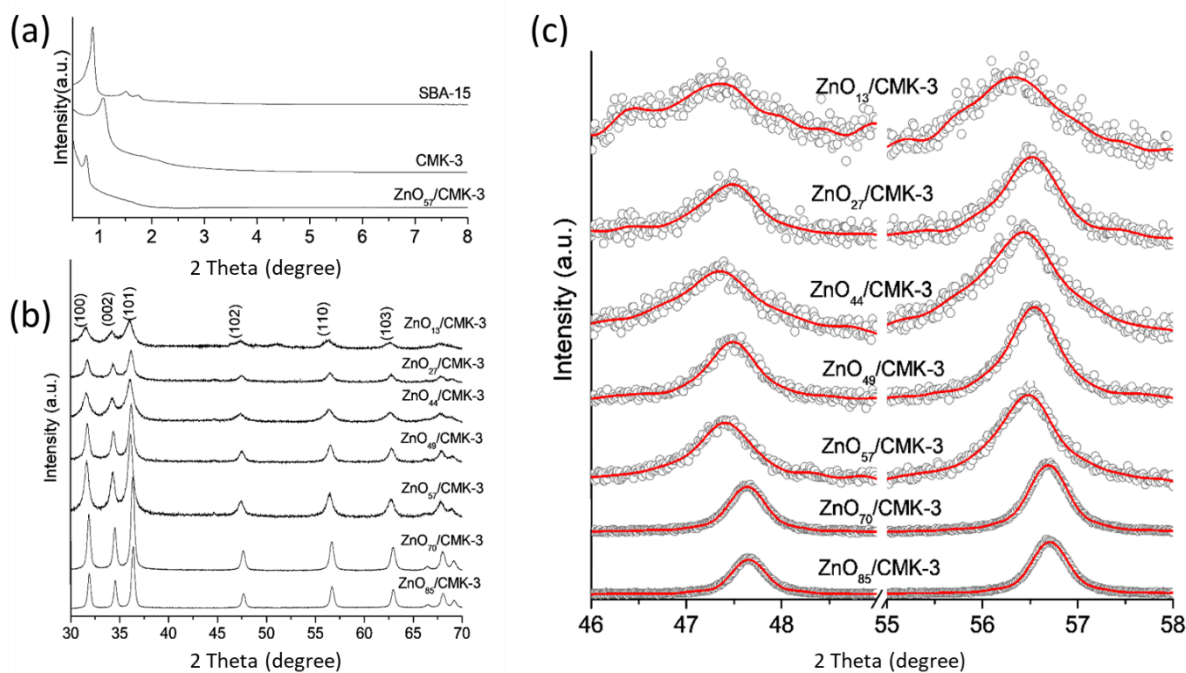
Figure 7-4: (a) Low angle XRD of SBA-15, CMK-3, and ZnO_{57}/CMK-3, (b) XRD of ZnO_x/CMK-3 samples and (c) the corresponding (102) and (110) peaks for AGS calculation.

Table 7-1: Average grain size, t-plot micropore and BET surface area of CMK-3 samples with various ZnO loading concentrations.

Sample designation	ZnO (wt %)	BET surface area (m²/g)	t-plot micropore surface area (m²/g)	AGS$_{ZnO(102)}$[1] (nm)	AGS$_{ZnO(110)}$[1] (nm)
SBA-15	0	807.9	--	N/A	N/A
CMK-3	0	1340.0	--	N/A	N/A
ZnO$_{13}$/CMK-3	13	855.5	96.6	11.3	9.0
ZnO$_{27}$/CMK-3	27	415.7	112.8	9.0	10.0
ZnO$_{44}$/CMK-3	44	351.2	72.5	11.3	11.3
ZnO$_{49}$/CMK-3	49	202.8	43.3	12.9	15.0
ZnO$_{57}$/CMK-3	57	123.5	37.9	10.8	11.3
ZnO$_{70}$/CMK-3	70	59.8	18.7	15.8	15.8
ZnO$_{85}$/CMK-3	85	25.6	3.4	21.2	19.7
ZnO$_{100}$	100	--	--	21.2	20.5

[1] Average grain size (AGS) of ZnO calculated using (102) and (110) peaks.

7.3.2 XPS analysis and surface species

Studies on band-gap and compositional properties of sensing materials confirm that an enhanced photo-activation phenomenon can be achieved by incorporating carbon within the structure (C-dopant), possibly due to the creation of oxygen vacancies (O$_{Vac}$) [153]. Therefore, XPS measurements were conducted to compare the surface species of the pure ZnO and optimal ZnO$_x$/CMK-3 composite (i.e. ZnO$_{57}$/CMK-3). As shown in Figure 7-5(a), Zn 2p$_{3/2}$ and Zn 2p$_{5/2}$ XPS lines in the ZnO$_{57}$/CMK-3 are blue-shifted with respect to pure ZnO. The difference of binding energies between lines of ZnO$_{57}$/CMK-3 is about 23.1 eV, suggesting the standard reference value of ZnO [153]. The deconvolution of Zn 2p$_{3/2}$ peak of pristine ZnO gives rise to two components at around 1021.3 eV and 1022.4 eV, corresponding to Zn–O and ZnO$_{Vac}$, respectively, where O$_{Vac}$ represents the oxygen vacancies. Comparing with pure ZnO, the surface of ZnO$_{57}$/CMK-3 is almost composed of ZnO$_{Vac}$. The O 1s spectra in Figure 7-6 confirms that there is more oxygen in the deficient regions in ZnO$_{57}$/CMK-3 compared to pristine ZnO

sample, which is in good agreement with Zn 2p XPS discussion. Figure 7-7 shows the deconvolution of C 1s, of ZnO$_{57}$/CMK-3, where the peaks at 284.8, and 286.2 eV can be ascribed to the surface adventitious carbon and Zn-O-C, respectively [153]; the peak at 288.6 eV represents the adsorbed CO$_2$ and structural carbonate species containing C=O [154,155].
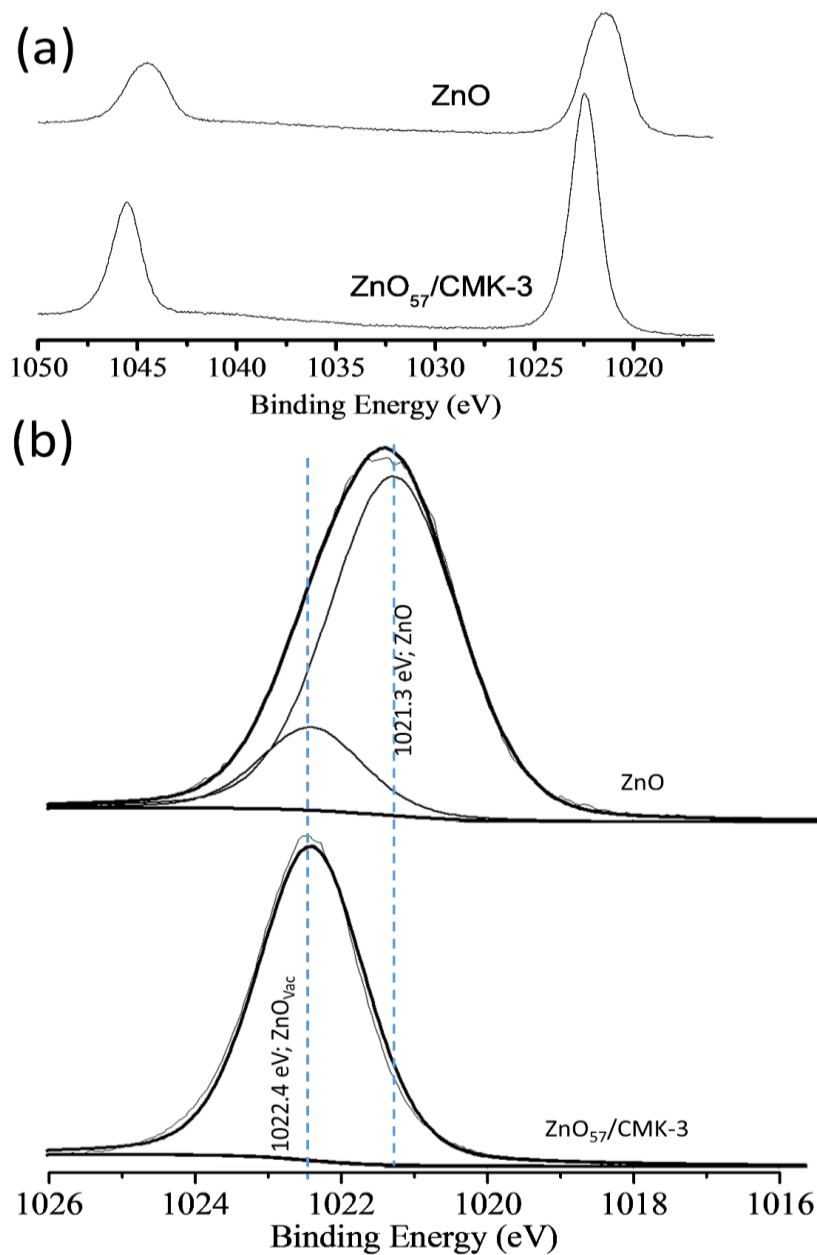
Figure 7-5: Zn 2p XPS spectra of ZnO and ZnO$_{57}$/CMK-3, and (b) corresponding deconvolution of 2p$_{3/2}$ peaks.
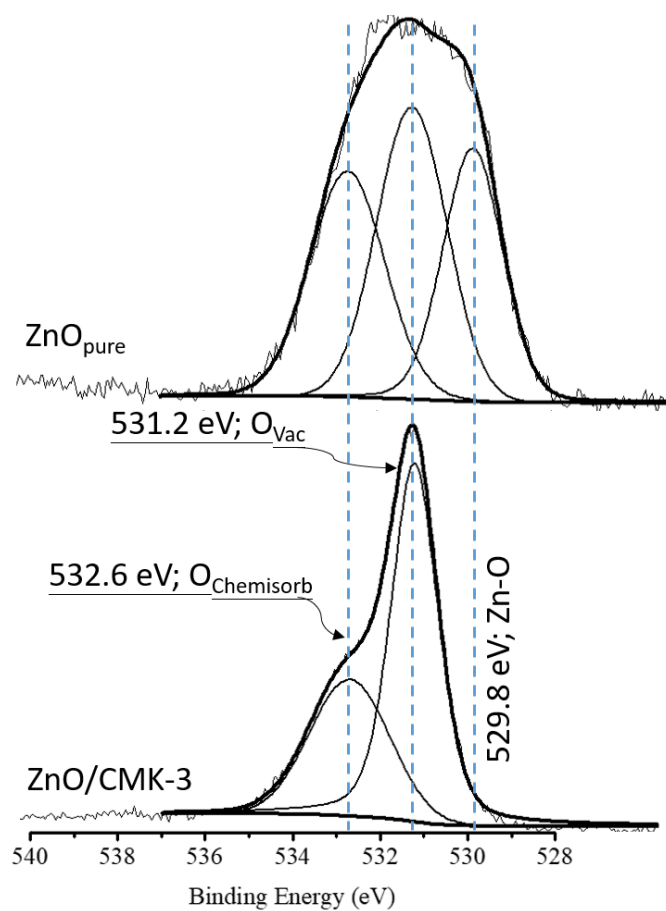
Figure 7-6: Decomposed O1s XPS spectrum of pure ZnO and ZnO_{57}/CMK-3.
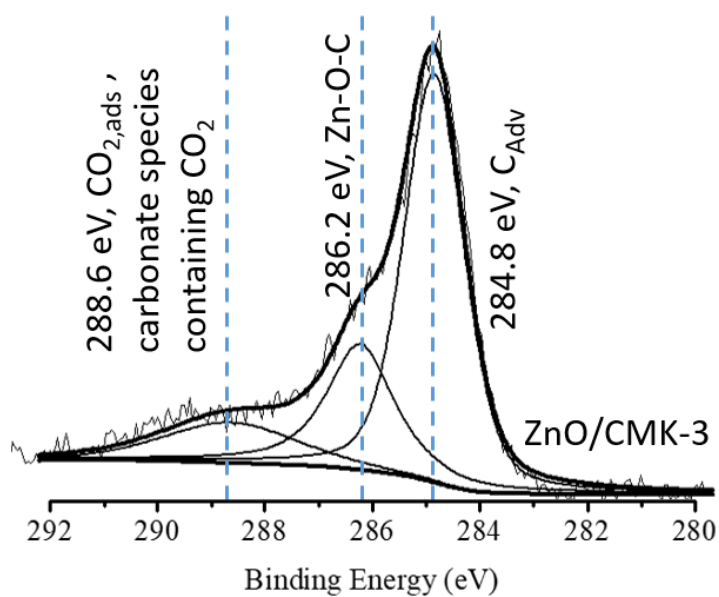
Figure 7-7: Decomposed C1s XPS spectrum of ZnO_{57}/CMK-3.

7.4 Photo-induced gas sensing performance

To examine the chemi-resistive sensing characteristics of the developed sensors, they were exposed to known concentrations of NO_2 and NH_3 gases, as the two common indoor air pollutants. In most countries, the legal thresholds for long-term exposure to NO_2 and NH_3 gases without health issues are 5 ppm and 25 ppm, respectively. Therefore, 5 ppm NO_2 and 25 ppm NH_3 were selected as target concentrations to cover the aforementioned range.

The sensors did not show any response in the absence of UV radiation. This was mainly due to the lack of surface charge carriers which are required for surface chemical reactions. However, UV-LED irradiation leads to a significant sensor response upon exposure to NO_2 and NH_3. The sensing responses were measured under continuous UV irradiation with 365 nm wavelength and 25 mW/cm^2 irradiance. The effectiveness of these operating conditions has been discussed previously in a research article [45].

Considering NO_2 as the targeted gas (Figure 7-8), the response values and response time constants are highly dependent on the ZnO loading concentration. The obtained results indicate that loaded ZnO on carbon with appropriate concentrations could result in a significant improvement in the sensor response, more than four times greater, compared to pristine ZnO NPs.

The pristine ZnO sample shows a response of 0.41 at 25 mW/cm^2 against NO_2 [61]. Upon loading on CMK-3 framework, the sensor response dramatically increased, e.g. the response of ZnO_{13}/CMK-3 is 3-fold of pristine ZnO. The responses then gradually increased as ZnO was further added to the CMK-3 and reached its maximum (1.91) at 57 wt% (i.e. ZnO_{57}/CMK-3). This improvement in response can be attributed to the higher specific surface area (123.5 m^2/g; *see Table 1*) and more oxygen vacant sites due to C-doping (*see Figure 7-5*) that collectively occur in the optimal sensor composition (i.e. ZnO_{57}/CMK-3). Further increase in loading concentration resulted in a decrease in the gas response. This reduction is a result of the decrease in the amount of gas that was adsorbed on the ZnO surface due to blockage of

the pores and non-accessible interior active sites. Also, it has been reported that excess C-doping can result in a higher recombination of photo-generated charge carriers [153].

As shown in Figure 7-8, the response and recovery time for the developed sensors varied as a function of ZnO loading concentration. The response time (T_{90}) increased from 2 mins for ZnO_{13}/CMK-3 to about 36 mins for ZnO_{70}/CMK-3. The recovery time followed the same trend with respect to ZnO loading concentration. This might be due to the longer migration time of the gas molecules within the pores to reach active ZnO sites. The response and recovery time decreased for ZnO_{85}/CMK-3 possibly due to the blockage of pores and not accessible inner surface, thus leaving the external surface area for the interaction with the gas.
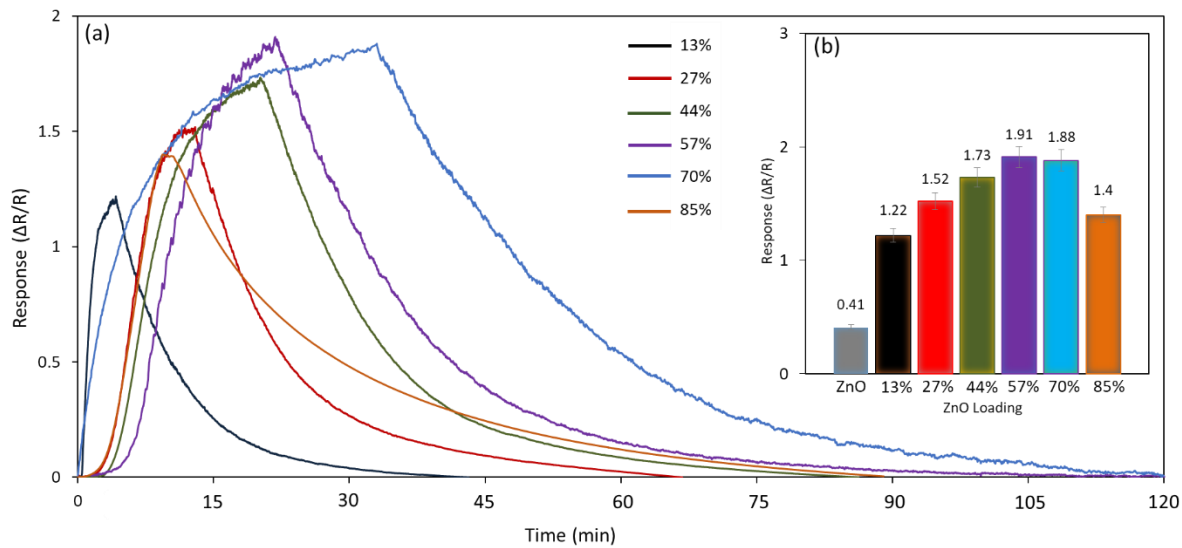
Figure 7-8: Responses of the developed ZnOx/CMK-3 sensors to 5 ppm NO_2. The error bars represent 95% confidence intervals for the results.

The response values and response curves against NH_3 are shown in Figure 7-9. The resistance of the sensors decreased rapidly upon exposure to NH_3 and recovered slowly in the presence of pure air. Similar to the response against NO_2, the response values increased to reach a maximum of 1.35 while adding

103

ZnO to 70 wt% (ZnO$_{70}$/CMK-3). This response is almost eight times greater than the response of pristine ZnO nanoparticles. The response characteristics of the developed sensors, however, were different when they were exposed to 25 ppm NH$_3$. Although the responses were lower than those of NO$_2$, the sensors responded faster, compared to NO$_2$, and the response time and recovery time remained constant over all ZnO$_x$/CMK-3 samples. The difference in the optimal compositions of the best NO$_2$ and NH$_3$ sensors presented in this study could be due to the size of gas molecules and their capability to diffuse in the micropores.
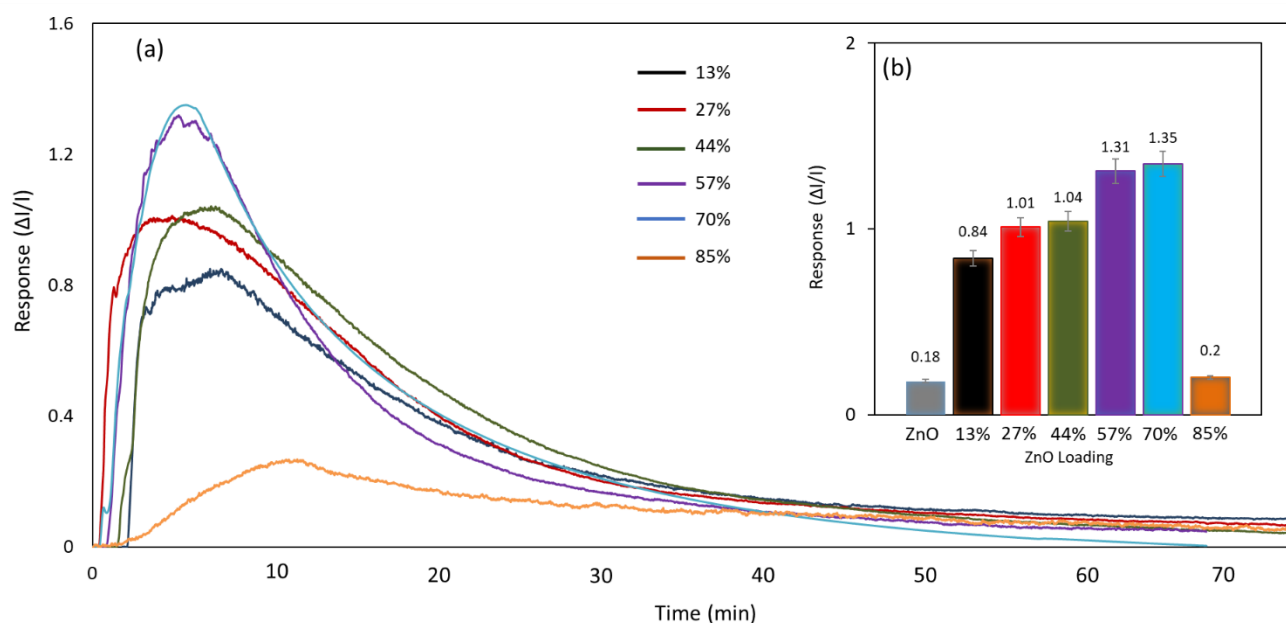
Figure 7-9: Responses of the developed ZnOx/CMK-3 sensors to 25 ppm NH$_3$. The error bars represent 95% confidence intervals for the results.

The relatively faster and constant response time of the sensors to 25 ppm NH$_3$ may be due to the fast reaction kinetics of NH$_3$ gas molecules. Upon irradiating the ZnOx/CMK-3 sensors, the electrons are moved to the lower carbon structure, leaving holes accessible to the gas. Due to the electron-donating nature of reducing gases (i.e. NH$_3$), the generated holes participate in the reactions, resulting in an increased conductance of the device. Therefore, the instant reaction of NH$_3$ with ZnO nanoparticles.

104

Similarly, excessive loading (i.e. 85 wt%) would block the pores and prevent the gas molecules to reach inner active sites, resulting in a low response value.

The study on the long-term stability of the developed sensor with optimal concentration (ZnO$_{57}$/CMK-3) revealed that the sensor response decreases initially to about 1.75 (NO$_2$) and 1.28 (NH$_3$) after 1 month and remains nearly constant in the next several months. The slight decrease in the gas response could be attributed to the adsorption of moisture or initial structural defects induced by the first UV exposure [70].

The sensitivities of the gas sensors with optimal loadings were also investigated against different concentrations of NO$_2$ and NH$_3$ (Figure 7-10). It can be observed that the response values increase with increasing the concentration; the sensitivities (slope of the trend-line) against NO$_2$ and NH$_3$ were found to be 5.24 and 2.26, respectively, where the linear part of the NH$_3$ chart was only considered for sensitivity determination.
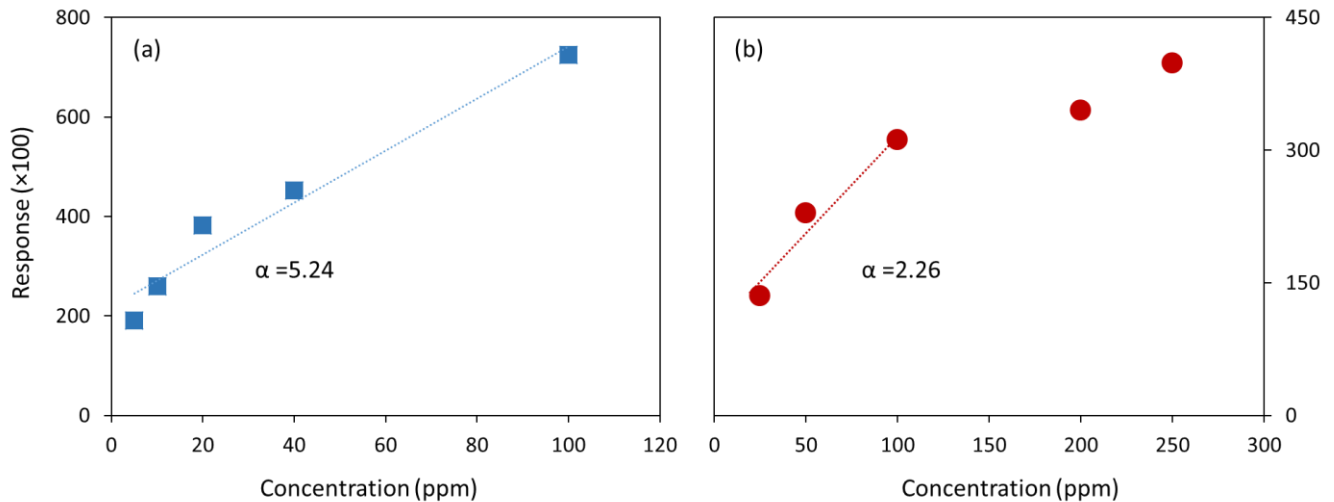
Figure 7-10: The response of sensors with optimal compositions after exposure to different concentrations of a) NO$_2$ and b) NH$_3$

7.5   Improvement in gas sensor response using ZnO-CMM

Studies on the transient photo-voltage (TPV) characteristics of ZnO-carbon mixtures have shown that lower recombination of charge carriers is wholly responsible for the gas sensing improvement in ZnO/CMK-3 sensors [156]. As confirmed by the results of the present study, the extended separation and restrained recombination of the photo-induced electron-hole carriers in C-doped ZnO can significantly improve the photoelectrical activity of samples.

In conclusion, loading ZnO on carbon mesoporous materials with appropriate concentration could result in a significant improvement in the sensor response, more than four times greater, compared to pristine ZnO NPs.

Chapter 8: **Conclusions and recommendations**

8.1   Conclusions

UV-LED activated metal oxide semiconductor sensors are promising alternatives for conventional high-temperature gas sensors. This new sensor platform is able to produce low cost, small size, sensitive sensors that can be integrated into micro-electronic devices. In this research, a number of practical issues of photo-activated gas sensors were addressed. In Chapter 1, the importance of gas sensing technology, and the fundamental mechanisms of chemi-resistive gas sensing in photo-activation mode were presented. In Chapter 2, different sections of the experimental platform were presented, and the fabrication process of sensors was discussed. Subsequently, the effects of irradiation parameters, sensing layer composition and strucutre on the sensing performance of the developed sensors were reported in Chapters 3–7. The sensors that were developed in this research were mainly tested against NO_2, which is a common indoor/outdoor air pollutant. The selectivity of some of the sensors were also tested in the presence of NH_3 and CO. The developed sensing materials may also respond to other gases (i.e. CH_4, CO_2, H_2 and O_3) but their response characteristics such as sensitivity, speed and stability might be different. The sensors were all tested in zero humidity. It is expected that the response values may decline in the presence of moisture due to the competitive adsorption of water molecules on the surface. However, the trend in the sensor response improvement made in this research will still stand. A study was also conducted to analyze the UV penetration depth and surface temperature of the sensors, which is presented in Appendix A5.

A summary of the results of the sensors that have been prepared in this report has been provided in the following table:

Table 8-1: A summary of the best sensor results against NO_2 and NH_3 under 365 nm UV-LED irradiation studied in the present research project

Sensor Material	Sensor Response ($\Delta R/Ra$)	Target Gas	Concentration (ppm)	Irradiance (mW/cm^2)
ZnO NPs	0.41	NO_2	5	25
SnO_2 NPs	0.53	NO_2	5	65
WO_3 NPs	16.76	NO_2	5	65
In_2O_3 NPs	0.67	NO_2	5	65
In_2O_3 NPs	2.06	NH_3	25	65
Ag-ZnO	0.98	NO_2	5	25
ZnO NWs	1.60	NO_2	5	25
Pt-ZnO NWs	4.33	NO_2	5	25
ZnO @ In_2O_3	2.49	NO_2	5	25
ZnO @ SnO_2	2.21	NO_2	5	25
ZnO_{57}-CMM	1.91	NO_2	5	25
ZnO_{70}-CMM	1.35	NH_3	25	25

8.1.1   Sensors' performances under various irradiation parameters

The results of this study indicated that the light source specifications could significantly affect the adsorption/desorption of NO_2 gas molecules. It was found that an appropriate range of irradiance is required for each sensor to achieve the highest sensitivity and shortest response time while having a complete recovery. It was also revealed that the surface should receive a minimum net energy to provide stable responses and prevent unwanted adsorption of the gas molecules. The highest response was observed at an intermediate UV wavelength. Under pulsed irradiation, the sensing signal level improved substantially for some sensors with slower responses and recovery times.

8.1.2 Ag:ZnO composite sensor with improved performance

The FE-SEM images exhibited the ellipsoidal Ag:ZnO nanoparticles that are uniformly distributed in the layer, and the XRD results confirmed the presence of Ag in the sensing material. Upon exposure to NO_2 at ambient temperature, although the pristine ZnO sensor provided a reasonable response (0.41), the newly developed Ag-doped ZnO sensor showed a superior response of 0.98, which is two times greater. The irradiance of the UV radiation was also shown to be a determining parameter for the response of the sensors. The synergetic effects of the semiconductor composite can explain the enhancement in the sensing response. Incorporating Ag increases the electron utilization ratio and reduces the recombination rate through trapping excited electrons in the Ag. This led to the injection of more electrons into the active surface area and improved the adsorption capability of the target gas.

8.1.3 ZnO nanowires decorated with Pt nanoparticles

A single-crystal array of ZnO NWs decorated with Pt nanoparticles was synthesized through self-assembly crystallization and photo-deposition, respectively. XRD and SEM data indicated the growth of NWs towards the hexagonal c-axis, with diameters between 140–300 nm. The presence of Pt nanoparticles, 1.0–5.0 nm in size, on the surface of ZnO NWs was confirmed through HRTEM and HAADF STEM analyses. The sensing performance analysis results confirmed that Pt-loading in a controlled concentration (i.e. 0.1 wt%) increases the response of the sensor from 1.6 to about 4.33 against 5 ppm NO_2 response under 25 mW/cm^2 UV-LED irradiation with 365nm wavelength. Metal loading also shortened the response time to about 140s, which was 50s faster than that of bare ZnO sample. This improvement in response characteristic was attributed to the more oxygen vacancies and more significant amount of photo-generated electrons in Pt-loaded sensing materials.

8.1.4　ZnO NWs hybridized with a shell layer of In_2O_3 and SnO_2

The synthesis of the core-shell NWs array films was carried out by a two-step process: hydrothermal synthesis of the base ZnO NW arrays and dip-coating deposition of In_2O_3 and SnO_2 shell layers. FE-SEM and XRD analyses demonstrated single-crystalline ZnO NWs with hexagonal shapes with an average diameter of $\sim$100 nm and a length of 1–2 μm, evenly distributed on the alumina substrate. Grainy polycrystalline In_2O_3 and SnO_2 shell layers covering the nanowire core could also be observed in the SEM images. The presence of Zn, In, Sn and O were confirmed by the broad area energy dispersive X-ray spectroscopy on the as-grown samples.

After exposure to 5ppm NO_2, the relative responses of the ZnO-In_2O_3 (2.49) and ZnO-SnO_2 (2.21) sensors were higher than that of pristine ZnO NWs (1.6). Excessive shell coating, however, resulted in lower carrier separation efficiency and reduced sensing response.

The enhancement of the photo-induced sensing response of ZnO-In_2O_3 and ZnO-SnO_2 sensors, compared to pristine ZnO nanowires, was attributed to the improved photon absorption, electron utilization and more active sites on the surface of the nanowires. It was suggested that ZnO core provides an additional depletion layer in the structure, while In_2O_3 and SnO_2 shell layers promote radiation absorption efficiency and enhance chemisorption ability in the structure. A combination of these phenomena led to the synergistic effect of the core-shell sensor with superior performance.

8.1.5　ZnO nanoparticles loaded on ordered carbon mesoporous materials

The CMK-3 was prepared by using mesoporous silica SBA-15 as a sacrificial template, and ZnO nanoparticles were loaded through a facile solution impregnation. TEM images of CMK-3 and ZnO_{57}/CMK-3 showed the 2-D hexagonal mesoporous structure of CMK-3 constructed by carbon rods. After being loaded with ZnO, no mesopore could be found in TEM images, and exceeding ZnO

nanostructures precipitated on the outside of the CMK-3 framework. The specific surface area and t-plot micropore surface area of ZnO_x/CMK-3 declined with increasing ZnO content. However, the specific surface area was still significantly larger than that of ZnO nanoparticles until 57 wt% ZnO loading. Studies on band-gap and compositional properties of sensing materials confirmed that an enhanced photo-activation phenomenon can be achieved by incorporating carbon within the structure (C-dopant), possibly due to the creation of oxygen vacancies (O_{Vac})

The fabricated sensors exhibited superior gas-sensing properties under UV illumination, as compared to pristine ZnO nanoparticles sensors. The hybrid sensors with 57 wt% and 70 wt% of ZnO were found to be the optimal compositions to have the maximum response against NO_2 and NH_3, respectively. The pristine ZnO sample showed a response of 0.41 at 25 mW/cm^2 against NO_2. Upon loading on CMK-3 framework, the sensor response dramatically increased, e.g. the response of ZnO_{13}/CMK-3 is 3-fold of pristine ZnO. The responses then gradually increased as ZnO was further added to the CMK-3 and reached its maximum (1.91) at 57 wt% (i.e. ZnO_{57}/CMK-3). This improvement in response could be attributed to the higher specific surface area and more oxygen vacant sites due to C-doping that collectively occur in the optimal sensor composition (i.e. ZnO_{57}/CMK-3). Further increase in loading concentration resulted in a decrease in the gas response.

The response characteristics of the developed sensors, however, were different when they were exposed to 25 ppm NH_3. Although the responses were lower than those of NO_2, the sensors responded faster, compared to NO_2, and the response time and recovery time remained constant over all ZnO_x/CMK-3 samples. This response was almost eight times greater than the response of pristine ZnO nanoparticles to NH_3. The difference in the optimal compositions of the best NO_2 and NH_3 sensors presented in this study could be due to the size of gas molecules and their capability to diffuse in the micropores.

111

8.2   Recommendations

The idea of using photo-activated chemical gas sensors as an alternative to conventional high-temperature sensors has been recently flourished, with the advances in novel high-power UV-LEDs. Thus, a broad area is provided for the scientific world to improve the specifications of UV-LED activated sensors. There are several vital areas with great potentials for more investigations; those include:

1) As discussed in Chapter 1, unique features of UV-LEDs, such as small size and low operating power, along with an innovative design strategy (i.e. backside-irradiation) enable integrating these sensors into portable electronic devices (PEDs) such as smartphones, tablets or e-readers. A method of fabricating these photo-activated sensors could be based on depositing interdigitated electrodes and relevant circuits over the light source during UV-LED fabrication, followed by material deposition using state-of-the-art printing technologies (Figure 8-1). In this case, several arrays of sensing layers can be developed to overcome the issues such as poor selectivity.
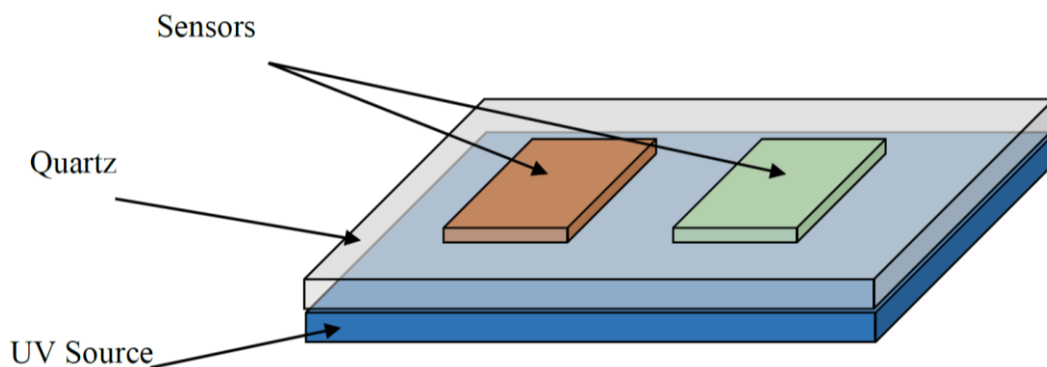
Figure 8-1: The suggested design consisting of a sensor network over a flat shape UV-LED

Integrating gas-sensitive films with UV light-emitting diodes (LEDs) will result in reduced power consumption, and lower production costs, accompanied by significant miniaturization. The gas-UV interaction will be also minimized in the new configuration, and the sensing materials will receive uniform irradiation with higher irradiance at lower operating power.

2) Theoretical modeling and simulation of gas sensing processes can be significantly helpful in selecting optimal materials, optimal configurations and optimal operational parameters. Moreover, many experimental observations, particularly in novel research projects such as photo-activated gas sensing, need a theory to interpret the results correctly. These theoretical simulation and modeling can promote understanding of the nature of interactions between photo-activated layer and surrounding gases that are responsible for high functionality of the sensors.

Although very few aspects of chemistry can be computed currently, a model comprising the governing equations of all the main phenomena can give useful insight into the importance of the mechanisms involved in the sensing process. For instance, starting from the macroscopic parameters, surface-molecule or photon-surface interactions can be used in describing the sensor response. Meanwhile, using quantum mechanics calculations, these macro-scale interactions can be corresponded to the energy (electronic) levels of the surface or sensing material. After all, statistical thermodynamics and kinetics can dig down into the electronic behaviour by using the molecular properties of the compound. Finally, a model that embed all those phenomena quantitatively should be able to describe real experimental results.

Therefore, it is highly recommended to conduct studies on comprehensive modeling approaches that simulate all main phenomena in photo-activated chemical gas sensing process such as optics,

surface diffusion, adsorption/desorption, surface reactions kinetics, electrochemistry and fluid dynamics.

3) Commercial resistive gas sensors exhibit various sensitivity to different gases when working at different elevated temperatures. This is particularly due to the change in the adsorption/desorption rates that can be modulated by temperature. To enhance the selectivity, a method which is called the sampling-and-hold method, is be used in high-temperature sensors during the sensing process. In this technique, the temperature of the sensing material is constantly fluctuating within a pre-determined range. The gas molecules are captured (adsorbed) at lower temperatures and then are slowly released (desorbed) by heating up the sensing material. This sampling-and-hold method could be a promising technique in photo-activated gas sensing, if being modified for UV irradiance on the sensor surface. Modulating irradiance on the sensor surface alters the adsorption/desorption kinetics (as shown in this research) and improves sensor selectivity to a particular gas. This idea not only shortens the response time of these sensors, but also reduces the power consumption and elongates UV source lifetime.

4) One potential area to study further in photo-activated sensors is to develop novel sensory material based on Tellurium such as TeO_2, TeO_3 and CdTe. Tellurium is a p-type semiconductor and has a unique lattice structure that contains six spiral chains in the corner and one in the center. Based on its structure, it shows some interesting photoconductivity, thermoelectric and catalytic properties, which may be beneficial for photo-activated gas sensing.

5) Humidity is considered as a deteriorating source of sensitivity, selectivity and response/recovery times, as the water vapor adsorption acts as a major competitor to target gaseous components. It is therefore necessary to do measurements under different humidity conditions, aiming to lower the humidity effects on the operation of sensors at room temperature, and to calibrate sensors' responses.

6) Porosity, pore size and particle size control of gas sensing films is another interesting area that can be worked to further improve the selectivity of the sensors. Porous materials are of significant interest due to their high surface area and special physical properties. Having a porous structure with controlled pore size distribution may help to control the diffusion rate of gases within the structure and tune the selectivity.

Bibliography

[1]   M. Kampa, E. Castanas, Human health effects of air pollution, Environ. Pollut. 151 (2008) 362–367.

[2]   K. Katsouyanni, Ambient air pollution and health, Br. Med. Bull. 68 (2003) 143–156.

[3]   C.-T. Rock, B.A., Wu, Performance of fixed, air-side economizer, and neural network demand-controlled ventilation in CAV systems, in: 1998 ASHRAE Annu. Meet., Toronto, Canada, 1998: pp. 234–245.

[4]   and J.B. Brandemuehl, M., The Impact of Demand Controlled and Economizer Ventilation Strategies on Energy Use in Buildings, ASHRAE Trans. 105 (1999) 39–50.

[5]   S.M. di Giacomo, Differential CO_2 based demand control ventilation: (Maximum energy savings & optimized IAQ) History, theory and myths, Energy Eng. J. Assoc. Energy Eng. 96 (1999) 58–76.

[6]   M.B. Schell, S.C. Turner, R.O. Shim, Application of CO_2-based demand-controlled ventilation using ASHRAE Standard 62: optimizing energy use and ventilation, ASHRAE Trans. 104 (1998) 1213–1225.

[7]   A.K. Persily, R.A. Morris, D.S. Butler, M. Beaton, C.O. Muller, J.D. Bowman, F.J. Offermann, J.E. Osborn, P.O. Fanger, F.M. Gallo, R.S. Rushing, D.S. Godwin, L.J. Schoen, W.J. Groah, M.H. Sherman, J.L. Halliwell, S.D. Hanson, D.D. Thayer, J.A. Tiffany, H. Levin, D.Y. Vyavaharkar, D.R. Warden, M.F. Mamayek, Ventilation for Acceptable Indoor Air Quality, Atlanta, GA, 1999.

[8]   Government of Canada, WHMIS 2015 — New Hazardous Products Regulations Requirements, (2015).

[9]   E. Espid, UV-LED photo-activated metal oxide semiconductors for gas sensing application :

fabrication and performance evaluation, University of British Columbia Dissertations, 2015.

[10]   K. Arshak, E. Moore, G.M. Lyons, J. Harris, S. Clifford, A review of gas sensors employed in electronic nose applications, Sens. Rev. 24 (2004) 181–198.

[11]   D. Zhang, J. Tong, B. Xia, Humidity-sensing properties of chemically reduced graphene oxide/polymer nanocomposite film sensor based on layer-by-layer nano self-assembly, Sensors Actuators B Chem. 197 (2014) 66–72.

[12]   E. Espid, F. Taghipour, UV-LED Photo-activated Chemical Gas Sensors : A Review, Crit. Rev. Solid State Mater. Sci. 0 (2017) 1–17.

[13]   a Bielanski, J. Deren, J. Haber, Electric Conductivty And Catalytic Activity Of Semiconduction Oxide Catalysts, Nature. 179 (1957) 668–669.

[14]   T. Seiyama, K. Fujiishi, M. Nagatani, A. Kato, A New Detector for Gaseous Components Using Zinc Oxide Thin Films, J. Soc. Chem. Ind. Japan. 66 (1963) 652–655.

[15]   T. Naoyoshi, Gas detecting device US 3695848 A, (1972).

[16]   C. Wang, L. Yin, L. Zhang, D. Xiang, R. Gao, Metal oxide gas sensors: sensitivity and influencing factors., Sensors (Basel). 10 (2010) 2088–106.

[17]   H. Chen, Y. Liu, C. Xie, J. Wu, D. Zeng, Y. Liao, A comparative study on UV light activated porous TiO_2 and ZnO film sensors for gas sensing at room temperature, Ceram. Int. 38 (2012) 503–509.

[18]   S. Mishra, C. Ghanshyam, N. Ram, R.P. Bajpai, R.K. Bedi, Detection mechanism of metal oxide gas sensor under UV radiation, Sensors Actuators B Chem. 97 (2004) 387–390.

[19]   C.A. Grimes, G.K. Mor, TiO_2 Nanotube Arrays: Synthesis, Properties, and Applications, Springer Science & Business Media, 2009.

[20]   F. Ingemar Lundstrom, Marten Armgarth, Anita Spetz, Winquist, Gas sensors based on catalytic

field-effect devices, Sensors and Actuators B, 10 (1986) 399–421

[21]   A. C. Partridge, P. Harris, M.K. Andrews, High sensitivity conducting polymer sensors, Analyst. 121 (1996) 1349.

[22]   J. Saura, Gas-sensing properties of SnO_2 pyrolytic films subjected to ultrviolet radiation, Sensors Actuators B Chem. 17 (1994) 211–214.

[23]   E. Comini, A. Cristalli, G. Faglia, G. Sberveglieri, Light enhanced gas sensing properties of indium oxide and tin dioxide sensors, Sensors Actuators B Chem. 65 (2000) 260–263.

[24]   V. Palmisano, E. Weidner, L. Boon-brett, C. Bonato, F. Harskamp, Selectivity and resistance to poisons of commercial hydrogen sensors, Int. J. Hydrogen Energy. 40 (2015) 11740–11747.

[25]   C. Guo, Z. Lin, W. Song, X. Wang, Y. Huang, K. Wang, Synthesis, UV response, and room-temperature ethanol sensitivity of undoped and Pd-doped coral-like SnO_2, J Nanopart Res. 15 (2013) 1998.

[26]   P. Camagni, G. Faglia, P. Galinetto a, C. Perego, G. Samoggia, G. Sberveglieri, Photosensitivity activation of SnO_2 thin film gas sensors at room temperature, 31 (1996) 99–103.

[27]   E. Comini, G. Faglia, G. Sberveglieri, UV light activation of tin oxide thin films for NO_2 sensing at low temperatures, Sensors Actuators, B Chem. 78 (2001) 73–77.

[28]   K. Anothainart, M. Burgmair, A. Karthigeyan, M. Zimmer, I. Eisele, Light enhanced NO_2 gas sensing with tin oxide at room temperature: conductance and work function measurements, Sensors Actuators B Chem. 93 (2003) 580–584.

[29]   A.Y. Nazzal, L. Qu, X. Peng, M. Xiao, Photoactivated CdSe Nanocrystals as Nanosensors for Gases, Nano Letters, 3 (2003) 819–822.

[30]   O.K. Varghese, G. Mor, M. Paulose, C.A. Grimes, A Room-Temperature, Self-cleaning, High-performance Hydrogen Sensor Based on Nanoporous Titania, Sensor Letters, 1 (2003) 42-46.

[31] T.Y. Yang, H.M. Lin, B.Y. Wei, C.Y. Wu, C.K. Lin, UV enhancement of the gas sensing properties of nano-TiO$_2$, Rev. Adv. Mater. Sci. 4 (2003) 48–54.

[32] D. Ito, M. Ichimura, Room-temperature hydrogen sensing properties of SnO$_2$ thin films fabricated by the photochemical deposition and doping methods, Japanese J. Appl. Physics, 45 (2006) 7094–7096.

[33] V.M. Arakelyan, K.S. Martirosyan, V.E. Galstyan, G.E. Shahnazaryan, V.M. Aroutiounian, Room temperature gas sensor based on porous silicon/metal oxide structure, Phys. Status Solidi. 4 (2007) 2059–2062.

[34] C. Ge, C. Xie, M. Hu, Y. Gui, Z. Bai, D. Zeng, Structural characteristics and UV-light enhanced gas sensitivity of La-doped ZnO nanoparticles, Mater. Sci. Eng. B Solid-State Mater. Adv. Technol. 141 (2007) 43–48.

[35] L.R. Skubal, N.K. Meshkov, M.C. Vogt, Detection and identification of gaseous organics using a TiO$_2$ sensor, J. Photochem. Photobiol. A Chem. 148 (2002) 103–108.

[36] C.-H. Han, D.-W. Hong, S.-D. Han, J. Gwak, K.C. Singh, Catalytic combustion type hydrogen gas sensor using TiO$_2$ and UV-LED, Sensors Actuators B Chem. 125 (2007) 224–228.

[37] N. Barsan, U. Weimar, Conduction model of metal oxide gas sensors, J. Electroceramics. 7 (2001) 143–167.

[38] M. Batzill, U. Diebold, The surface and materials science of tin oxide, Prog. Surf. Sci. 79 (2005) 47–154.

[39] A. Labidi, E. Gillet, R. Delamare, M. Maaref, K. Aguir, Ethanol and ozone sensing characteristics of WO$_3$ based sensors activated by Au and Pd, Sensors Actuators, B Chem. 120 (2006) 338–345.

[40] T. Samerjai, N. Tamaekong, K. Wetchakun, V. Kruefu, C. Liewhiran, C. Siriwong, A.

Wisitsoraat, S. Phanichphat, Flame-spray-made metal-loaded semiconducting metal oxides thick films for flammable gas sensing, Sensors Actuators, B Chem. 171–172 (2012) 43–61.

[41] L.I. Trakhtenberg, G.N. Gerasimov, V.F. Gromov, T.V. Belysheva, O.J. Ilegbusi, Effect of composition on sensing properties of SnO_2-In_2O_3 mixed nanostructured films, Sensors Actuators B Chem. 169 (2012) 32–38.

[42] E. Comini, L. Ottini, G. Faglia, G. Sberveglieri, SnO 2 RGTO UV Activation for CO Monitoring, 4 (2004) 17–20.

[43] S.W. Fan, A.K. Srivastava, V.P. Dravid, UV-activated room-temperature gas sensing mechanism of polycrystalline ZnO, Appl. Phys. Lett. 95 (2009) 2007–2010.

[44] T. Wagner, C.D. Kohl, S. Morandi, C. Malagú, N. Donato, M. Latino, G. Neri, M. Tiemann, Photoreduction of mesoporous In_2O_3: Mechanistic model and utility in gas sensing, Chem. - A Eur. J. 18 (2012) 8216–8223.

[45] E. Espid, A.S. Noce, F. Taghipour, The effect of radiation parameters on the performance of photo-activated gas sensors, J. Photochem. Photobiol. A Chem. 374 (2019) 95–105.

[46] K. Wetchakun, T. Samerjai, N. Tamaekong, C. Liewhiran, C. Siriwong, V. Kruefu, a. Wisitsoraat, a. Tuantranont, S. Phanichphant, Semiconducting metal oxides as sensors for environmentally hazardous gases, Sensors Actuators B Chem. 160 (2011) 580–591.

[47] S. Phanichphant, Semiconductor Metal Oxides as Hydrogen Gas Sensors, Procedia Eng. 87 (2014) 795–802.

[48] P. Zhang, G. Pan, B. Zhang, J. Zhen, Y. Sun, High Sensitivity Ethanol Gas Sensor Based on Sn-doped ZnO Under Visible Light Irradiation at Low Temperature, 17 (2014) 817–822.

[49] L. Liu, X. Li, P.K. Dutta, J. Wang, Room temperature impedance spectroscopy-based sensing of formaldehyde with porous TiO_2 under UV illumination, Sensors Actuators, B Chem. 185 (2013)

1–9.

[50] H. Ahn, Y. Wang, S. Hyun Jee, M. Park, Y.S. Yoon, D.J. Kim, Enhanced UV activation of electrochemically doped Ni in ZnO nanorods for room temperature acetone sensing, Chem. Phys. Lett. 511 (2011) 331–335.

[51] N. Yamazoe, Toward innovations of gas sensor technology, Sensors Actuators, B Chem. 108 (2005) 2–14.

[52] N. Yamazoe, G. Sakai, K. Shimanoe, Oxide semiconductor gas sensors, Catal. Surv. from Asia. 7 (2003) 63–75.

[53] D. Naturwissenschaften, Characterisation and Functionality of SnO_2 Gas Sensors Using Vibrational Spectroscopy, University of Tubingen Dissertation (2005).

[54] O. Casals, N. Markiewicz, C. Fabrega, I. Gràcia, C. Cane, H.S. Wasisto, A. Waag, J.D. Prades, A Parts per Billion (ppb) Sensor for NO_2 with Microwatt (μW) Power Requirements Based on Micro Light Plates, ACS Sensors. 4 (2019) 822–826.

[55] N. Markiewicz, O. Casals, C. Fabrega, I. Gràcia, C. Cané, H.S. Wasisto, A. Waag, J.D. Prades, Micro light plates for low-power photoactivated (gas) sensors, Appl. Phys. Lett. 114 (2019).

[56] C.Y. Wang, V. Cimalla, T. Kups, C.C. Röhlig, T. Stauden, O. Ambacher, M. Kunzer, T. Passow, W. Schirmacher, W. Pletschen, K. Köhler, J. Wagner, Integration of In_2O_3 nanoparticle based ozone sensors with GaInNGaN light emitting diodes, Appl. Phys. Lett. 91 (2007) 1–4.

[57] J.H. Yu, H.J. Yang, H.S. Mo, T.S. Kim, T.S. Jeong, C.J. Youn, K.J. Hong, Sensing mechanism and behavior of sputtered ZnCdO ozone sensors enhanced by photons for room- temperature operation, J. Electron. Mater. 42 (2013) 720–725.

[58] C.L. Hsu, L.F. Chang, T.J. Hsueh, Light-activated humidity and gas sensing by ZnO nanowires grown on LED at room temperature, Sensors Actuators, B Chem. 249 (2017) 265–277.

[59] B. Gong, T. Shi, W. Zhu, G. Liao, X. Li, J. Huang, T. Zhou, Z. Tang, UV irradiation-assisted ethanol detection operated by the gas sensor based on ZnO nanowires/optical fiber hybrid structure, Sensors Actuators, B Chem. 245 (2017) 821–827.

[60] G. Lu, J. Xu, J. Sun, Y. Yu, Y. Zhang, F. Liu, UV-enhanced room temperature NO_2 sensor using ZnO nanorods modified with SnO_2 nanoparticles, Sensors Actuators B Chem. 162 (2012) 82–88.

[61] E. Espid, F. Taghipour, Development of highly sensitive ZnO/In_2O_3 composite gas sensor activated by UV-LED, Sensors Actuators B. Chem. 241 (2017) 828–839.

[62] B. Fabbri, A. Gaiardo, A. Giberti, V. Guidi, C. Malagù, A. Martucci, M. Sturaro, G. Zonta, S. Gherardi, P. Bernardoni, Chemoresistive properties of photo-activated thin and thick ZnO films, Sensors Actuators B Chem. 222 (2015) 1251–1256.

[63] S. Chang, K. Chen, UV Illumination Room-Temperature ZnO Nanoparticle Ethanol Gas Sensors, 2012 (2012).

[64] S.W. Fan, A.K. Srivastava, V.P. Dravid, Nanopatterned polycrystalline ZnO for room temperature gas sensing, Sensors Actuators, B Chem. 144 (2010) 159–163.

[65] A.S. Chizhov, M.N. Rumyantseva, R.B. Vasiliev, D.G. Filatova, K.A. Drozdov, I. V Krylov, A.M. Abakumov, A.M. Gaskov, Sensors and Actuators B : Chemical Visible light activated room temperature gas sensors based on nanocrystalline ZnO sensitized with CdSe quantum dots, Sensors Actuators B. Chem. 205 (2014) 305–312.

[66] D. Klaus, D. Klawinski, S. Amrehn, M. Tiemann, T. Wagner, Light-activated resistive ozone sensing at room temperature utilizing nanoporous In_2O_3 particles: Influence of particle size, Sensors Actuators B Chem. 217 (2015) 181–185.

[67] T. Wagner, C.D. Kohl, C. Malagù, N. Donato, M. Latino, G. Neri, M. Tiemann, UV light-enhanced NO_2 sensing by mesoporous In_2O_3: Interpretation of results by a new sensing model,

Sensors Actuators, B Chem. 187 (2013) 488–494.

[68] S. Trocino, P. Frontera, A. Donato, C. Busacca, L.A. Scarpino, P. Antonucci, G. Neri, Gas sensing properties under UV radiation of In_2O_3 nanostructures processed by electrospinning, Mater. Chem. Phys. 147 (2014) 35–41.

[69] J.D. Prades, R. Jimenez-Diaz, F. Hernandez-Ramirez, S. Barth, a. Cirera, a. Romano-Rodriguez, S. Mathur, J.R. Morante, Equivalence between thermal and room temperature UV light-modulated responses of gas sensors based on individual SnO_2 nanowires, Sensors Actuators B Chem. 140 (2009) 337–341.

[70] E. Comini, L. Ottini, G. Faglia, G. Sberveglieri, SnO2 RGTO UV Activation for CO Monitoring, IEEE Sens. J. 4 (2004) 17–20.

[71] F.H. Saboor, T. Ueda, K. Kamada, T. Hyodo, Y. Mortazavi, A.A. Khodadadi, Y. Shimizu, Enhanced NO_2 gas sensing performance of bare and Pd-loaded SnO_2 thick film sensors under UV-light irradiation at room temperature, Sensors Actuators, B Chem. 223 (2016) 429–439.

[72] S. Park, T. Hong, J. Jung, C. Lee, Room temperature hydrogen sensing of multiple networked ZnO/WO3 core–shell nanowire sensors under UV illumination, Curr. Appl. Phys. 14 (2014) 1171–1175.

[73] M. Trawka, J. Smulko, L. Hasse, C. Granqvist, Sensors and Actuators B : Chemical Fluctuation enhanced gas sensing with WO_3 -based nanoparticle gas sensors modulated by UV light at selected wavelengths, Sensors Actuators B. Chem. 234 (2016) 453–461.

[74] P. Kubelka, New contributions to the optics of intensely light-scattering materials., J. Opt. Soc. Am. 38 (1948) 448–457.

[75] A. Janotti, C.G. Van de Walle, Fundamentals of zinc oxide as a semiconductor, Reports Prog. Phys. 72 (2009) 126501.

123

[76] P.D.C. King, T.D. Veal, F. Fuchs, C.Y. Wang, D.J. Payne, a. Bourlange, H. Zhang, G.R. Bell, V. Cimalla, O. Ambacher, R.G. Egdell, F. Bechstedt, C.F. McConville, Band gap, electronic structure, and surface electron accumulation of cubic and rhombohedral In_2O_3, Phys. Rev. B - Condens. Matter Mater. Phys. 79 (2009) 1–10.

[77] J.D. Yao, J.M. Shao, G.W. Yang, Ultra-broadband and high- responsive photodetectors based on bismuth film at room temperature, Nat. Publ. Gr. (2015) 1–7.

[78] T.O. Mason, G.B. Gonzalez, D.R. Kammler, N. Mansourian-Hadavi, B.J. Ingram, Defect chemistry and physical properties of transparent conducting oxides in the CdO-In_2O_3-SnO_2 system, Thin Solid Films. 411 (2002) 106–114.

[79] A. Giberti, B. Fabbri, A. Gaiardo, V. Guidi, C. Malag, Resonant photoactivation of cadmium sulfide and its effect on the surface chemical activity, Appl. Phys. Lett. 104 (2014) 20–24.

[80] A. Giberti, C. Malag, V. Guidi, WO_3 sensing properties enhanced by UV illumination: An evidence of surface effect, Sensors Actuators, B Chem. 165 (2012) 59–61.

[81] A. Afzal, N. Cioffi, L. Sabbatini, L. Torsi, NO x sensors based on semiconducting metal oxide nanostructures: Progress and perspectives, Sensors Actuators, B Chem. 171–172 (2012) 25–42.

[82] M. Ahmad, J. Zhu, ZnO based advanced functional nanostructures: synthesis, properties and applications, J. Mater. Chem. 21 (2011) 599–614.

[83] A. Wei, L. Pan, W. Huang, Recent progress in the ZnO nanostructure-based sensors, Mater. Sci. Eng. B. 176 (2011) 1409–1421.

[84] Ö.A. Yıldırım, H.E. Unalan, C. Durucan, Highly Efficient Room Temperature Synthesis of Silver-Doped Zinc Oxide (ZnO:Ag) Nanoparticles: Structural, Optical, and Photocatalytic Properties, J. Am. Ceram. Soc. 96 (2013) 766–773.

[85] N. Serpone, P. Maruthamuthu, P. Pichat, E. Pelizzetti, H. Hidaka, Exploiting the interparticle

electron transfer process in the photocatalysed oxidation of phenol, 2-chlorophenol and pentachlorophenol: chemical evidence for electron and hole transfer between coupled semiconductors, J. Photochem. Photobiol. A Chem. 85 (1995) 247–255.

[86] R. Wang, J.H. Xin, Y. Yang, H. Liu, L. Xu, J. Hu, The characteristics and photocatalytic activities of silver doped ZnO nanocrystallites, Appl. Surf. Sci. 227 (2004) 312–317.

[87] J.J. Wu, C.H. Tseng, Photocatalytic properties of nc-Au/ZnO nanorod composites, Appl. Catal. B Environ. 66 (2006) 51–57.

[88] J. Liqiang, W. Baiqi, X. Baifu, L. Shudan, S. Keying, C. Weimin, F. Honggang, Investigations on the surface modification of ZnO nanoparticle photocatalyst by depositing Pd, J. Solid State Chem. 177 (2004) 4221–4227.

[89] R. Georgekutty, M.K. Seery, S.C. Pillai, A highly efficient Ag-ZnO photocatalyst: Synthesis, properties, and mechanism, J. Phys. Chem. C. 112 (2008) 13563–13570.

[90] J. Yuan, E.S.G. Choo, X. Tang, Y. Sheng, J. Ding, J. Xue, Synthesis of ZnO-Pt nanoflowers and their photocatalytic applications., Nanotechnology. 21 (2010) 185606.

[91] R. Kumar, D. Rana, A. Umar, P. Sharma, S. Chauhan, M.S. Chauhan, Ag-doped ZnO nanoellipsoids: Potential scaffold for photocatalytic and sensing applications, Talanta. 137 (2015) 204–213.

[92] M.K. Seery, R. George, P. Floris, S.C. Pillai, Silver doped titanium dioxide nanomaterials for enhanced visible light photocatalysis, J. Photochem. Photobiol. A Chem. 189 (2007) 258–263.

[93] Y. Zheng, L. Zheng, Y. Zhan, X. Lin, Q. Zheng, K. Wei, Ag/ZnO heterostructure nanocrystals: Synthesis, characterization, and photocatalysis, Inorg. Chem. 46 (2007) 6980–6986.

[94] T. Alammar, A.-V. Mudring, Facile preparation of Ag/ZnO nanoparticles via photoreduction, J. Mater. Sci. 44 (2009) 3218–3222.

[95] Z. Zhang, H. Liu, H. Zhang, H. Dong, X. Liu, H. Jia, B. Xu, Synthesis of spindle-like Ag/ZnO heterostructure composites with enhanced photocatalytic performance, Superlattices Microstruct. 65 (2014) 134–145.

[96] Y. Zheng, C. Chen, Y. Zhan, X. Lin, Q. Zheng, K. Wei, J. Zhu, Photocatalytic activity of Ag/ZnO heterostructure nanocatalyst: Correlation between structure and property, J. Phys. Chem. C. 112 (2008) 10773–10777.

[97] J. Cui, D. Wang, T. Xie, Y. Lin, Study on photoelectric gas-sensing property and photogenerated carrier behavior of Ag-ZnO at the room temperature, Sensors Actuators, B Chem. 186 (2013) 165–171.

[98] S. Ghosh, C. Roychaudhuri, R. Bhattacharya, H. Saha, N. Mukherjee, Palladium − Silver-Activated ZnO Surface : Highly Selective Methane Sensor at Reasonably Low Operating Temperature, ACS Appl. Mater. Interfaces. 6 (2014) 3879−3887.

[99] T. Wu, Z. Wang, M. Tian, J. Miao, H. Zhang, J. Sun, UV excitation NO_2 gas sensor sensitized by ZnO quantum dots at room temperature, Sensors Actuators B Chem. 259 (2018) 526–531.

[100] R. Chen, J. Wang, Y. Xia, L. Xiang, Near infrared light enhanced room-temperature NO_2 gas sensing by hierarchical ZnO nanorods functionalized with PbS quantum dots, Sensors Actuators B Chem. 255 (2018) 2538–2545.

[101] Y. Zhou, C. Gao, Y. Guo, UV assisted ultrasensitive trace NO_2 gas sensing based on few-layer MoS_2 nanosheet–ZnO nanowire heterojunctions at room temperature, J. Mater. Chem. A. 6 (2018) 10286–10296.

[102] L. Qi, L. Yu, Z. Liu, F. Guo, Y. qiang Gu, X. Fan, An enhanced optoelectronic NO_2 gas sensors based on direct growth ZnO nanowalls in situ on porous rGO, J. Alloys Compd. 749 (2018) 244–249.

[103] H. Tian, H. Fan, J. Ma, Z. Liu, L. Ma, S. Lei, J. Fang, C. Long, Pt-decorated zinc oxide nanorod arrays with graphitic carbon nitride nanosheets for highly efficient dual-functional gas sensing, J. Hazard. Mater. 341 (2018) 102–111.

[104] X. Su, G. Duan, Z. Xu, F. Zhou, W. Cai, Structure and thickness-dependent gas sensing responses to NO_2 under UV irradiation for the multilayered ZnO micro/nanostructured porous thin films, J. Colloid Interface Sci. 503 (2017) 150–158.

[105] A.C. Catto, L.F. da Silva, C. Ribeiro, S. Bernardini, K. Aguir, E. Longo, V.R. Mastelaro, An easy method of preparing ozone gas sensors based on ZnO nanorods, RSC Adv. 5 (2015) 19528–19533.

[106] Y. Ding, B. Yang, H. Liu, Z. Liu, X. Zhang, X. Zheng, Q. Liu, FePt-Au ternary metallic nanoparticles with the enhanced peroxidase-like activity for ultrafast colorimetric detection of H_2O_2, Sensors Actuators, B Chem. 259 (2018) 775–783.

[107] M. Chen, B. Yang, J. Zhu, H. Liu, X. Zhang, X. Zheng, Q. Liu, FePt nanoparticles-decorated graphene oxide nanosheets as enhanced peroxidase mimics for sensitive response to H_2O_2, Mater. Sci. Eng. C. 90 (2018) 610–620.

[108] E. Espid, F. Taghipour, Facile Synthesis and UV-Activated Gas Sensing Performance of Ag : ZnO Nano-Ellipsoids, ECS J. Solid State Sci. Technol. 7 (2018) 3089–3093.

[109] T. Hsueh, S. Chang, C. Hsu, Y. Lin, I. Chen, T. Hsueh, S. Chang, Highly sensitive ZnO nanowire ethanol sensor with Pd adsorption Highly sensitive ZnO nanowire ethanol sensor with Pd adsorption, Appl. Phys. Lett. 053111 (2007).

[110] P. Albers, K. Seibold, High-Dispersion Direct Current Sputtered Platinum-TiO_2 Powder Catalyst Active in Ethane Hydrogenolysis, Phys. Inorg. Chem. 20 (1989) 1510–1515.

[111] J. He, I. Ichinose, T. Kunitake, A. Nakao, In Situ Synthesis of Noble Metal Nanoparticles in

Ultrathin TiO_2 - Gel Films by a Combination of Ion-Exchange and Reduction Processes, Langmuir. 25 (2002) 10005–10010.

[112] Y. Zhang, J. Xu, P. Xu, Y. Zhu, Decoration of ZnO nanowires with Pt nanoparticles and their improved gas sensing and photocatalytic performance, Nanotechnology. 21 (2010).

[113] K. Wu, X. Zhao, M. Chen, H. Zhang, Z. Liu, X. Zhang, X. Zhu, Q. Liu, Synthesis of well-dispersed Fe_3O_4 nanoparticles loaded on montmorillonite and sensitive colorimetric detection of H2O2based on its peroxidase-like activity, New J. Chem. 42 (2018) 9578–9587.

[114] H. Liu, Y. Ding, B. Yang, Z. Liu, Q. Liu, X. Zhang, Colorimetric and ultrasensitive detection of H_2O_2 based on Au/Co_3O_4-CeO_x nanocomposites with enhanced peroxidase-like performance, Sensors Actuators, B Chem. 271 (2018) 336–345.

[115] N. Sakamoto, H. Ohtsuka, T. Ikeda, K. Maeda, D. Lu, M. Kanehara, K. Teramura, T. Teranishi, K. Domen, Highly dispersed noble-metal/chromia (core/shell) nanoparticles as efficient hydrogen evolution promoters for photocatalytic overall water splitting under visible light, Nanoscale. 1 (2009) 106.

[116] B. Adeli, F. Taghipour, Facile synthesis of highly efficient nano-structured gallium zinc oxynitride solid solution photocatalyst for visible-light overall water splitting, Appl. Catal. A Gen. 521 (2016) 250–258.

[117] B.A. Koudehi, Solar Hydrogen Generation Through Overall Water Splitting on Gallium-Zinc Oxynitride Visible Light Activated Photocatalyst, University of British Columbia Dissertation, 2017.

[118] L. Zhang, M. Qin, W. Yu, Q. Zhang, H. Xie, Z. Sun, Q. Shao, X. Guo, L. Hao, Y. Zheng, Z. Guo, Heterostructured TiO_2/WO_3 Nanocomposites for Photocatalytic Degradation of Toluene under Visible Light, J. Electrochem. Soc. 164 (2017) H1086–H1090.

[119] L. Zhang, W. Yu, C. Han, J. Guo, Q. Zhang, H. Xie, Q. Shao, Z. Sun, Z. Guo, Large Scaled Synthesis of Heterostructured Electrospun TiO_2/SnO_2 Nanofibers with an Enhanced Photocatalytic Activity, J. Electrochem. Soc. 164 (2017) H651–H656.

[120] K. Maeda, A. Xiong, T. Yoshinaga, T. Ikeda, N. Sakamoto, T. Hisatomi, M. Takashima, D. Lu, M. Kanehara, T. Setoyama, T. Teranishi, K. Domen, Photocatalytic overall water splitting promoted by two different cocatalysts for Hydrogen and Oxygen evolution under visible light, Angew. Chemie - Int. Ed. 49 (2010) 4096–4099.

[121] K. Maeda, K. Teramura, D. Lu, T. Takata, N. Saito, Y. Inoue, K. Domen, Characterization of Rh-Cr mixed-oxide nanoparticles dispersed on $(Ga_{1-x}Zn_x)(N_{1-x}O_x)$ as a cocatalyst for visible-light-driven overall water splitting, J. Phys. Chem. B. 110 (2006) 13753–13758.

[122] B. Adeli, F. Taghipour, Reduced graphene oxide composite of gallium zinc oxynitride photocatalyst with improved activity for overall water splitting, Chem. Eng. Technol. 39 (2016) 142–148.

[123] H. Tian, H. Fan, G. Dong, L. Ma, J. Ma, NiO/ZnO p-n heterostructures and their gas sensing properties for reduced operating temperature, RSC Adv. 6 (2016) 109091–109098.

[124] X. Wang, F. Sun, Y. Duan, Z. Yin, W. Luo, Y.A. Huang, J. Chen, Highly sensitive, temperature-dependent gas sensor based on hierarchical ZnO nanorod arrays, J. Mater. Chem. C. 3 (2015) 11397–11405

[125] M. Ahn, K. Park, J. Heo, J. Park, D. Kim, K.J. Choi, J. Lee, S. Hong, Gas sensing properties of defect-controlled ZnO-nanowire gas sensor Gas sensing properties of defect-controlled ZnO-nanowire gas sensor, Appl. Phys. Lett. 93 (2008) 1–4.

[126] M. Ahn, K. Park, J. Heo, J. Park, D. Kim, K.J. Choi, J. Lee, S. Hong, M. Ahn, K. Park, J. Heo, J. Park, D. Kim, K.J. Choi, J. Lee, Gas sensing properties of defect-controlled ZnO-nanowire gas

sensor Gas sensing properties of defect-controlled ZnO-nanowire gas sensor, 263103 (2008) 1–4.

[127] A. Cabot, J. Arbiol, J.R. Morante, U. Weimar, N. Bârsan, W. Göpel, Analysis of the noble metal catalytic additives introduced by impregnation of as obtained SnO_2 sol–gel nanocrystals for gas sensors, Sensors Actuators B Chem. 70 (2000) 87–100.

[128] Y. Mun, S. Park, S. An, C. Lee, H.W. Kim, NO_2 gas sensing properties of Au-functionalized porous ZnO nanosheets enhanced by UV irradiation, Ceram. Int. 39 (2013) 8615–8622.

[129] Y. Kang, S. Pyo, D.-H. Baek, J. Kim, Flexible and transparent NO_2; sensor using functionalized MoS, in: 2017 19th Int. Conf. Solid-State Sensors, Actuators Microsystems, IEEE, 2017: pp. 1429–1432.

[130] Y. Zhou, C. Gao, Y. Guo, UV assisted ultrasensitive trace NO_2 gas sensing based on few-layer MoS_2 nanosheet–ZnO nanowire heterojunctions at room temperature, J. Mater. Chem. A. 6 (2018) 10286–10296.

[131] R. Kumar, N. Goel, M. Kumar, UV-Activated MoS_2 Based Fast and Reversible NO_2 Sensor at Room Temperature, ACS Sensors. 2 (2017) 1744–1752.

[132] T. Wagner, C.D. Kohl, C. Malagù, N. Donato, M. Latino, G. Neri, M. Tiemann, UV light-enhanced NO_2 sensing by mesoporous In_2O_3: Interpretation of results by a new sensing model, Sensors Actuators, B Chem. 187 (2013) 488–494.

[133] I. Karaduman, D.E. Yıldız, M.M. Sincar, S. Acar, UV light activated gas sensor for NO_2 detection, Mater. Sci. Semicond. Process. 28 (2014) 43–47.

[134] W. An, X. Wu, X.C. Zeng, Adsorption of O_2 , H_2 , CO , NH_3 , and NO_2 on ZnO Nanotube : A Density Functional Theory Study, J. Phys. Chem. C. 112 (2008) 5747–5755.

[135] K. Ahmadi, A.A. Ziabari, K. Mirabbaszadeh, A. Ahadpour Shal, Synthesis and characterization

of ZnO/TiO$_2$ composite core/shell nanorod arrays by sol-gel method for organic solar cell applications, Bull. Mater. Sci. 38 (2015) 617–623.

[136] Y. Liu, P. Zhang, B. Tian, J. Zhang, Core-Shell Structural CdS/SnO$_2$ Nanorods with Excellent Visible-Light Photocatalytic Activity for the Selective Oxidation of Benzyl Alcohol to Benzaldehyde, ACS Appl. Mater. Interfaces. 7 (2015) 13849–13858.

[137] R. Ghosh Chaudhuri, S. Paria, Core/shell nanoparticles: Classes, properties, synthesis mechanisms, characterization, and applications, Chem. Rev. 112 (2012) 2373–2433.

[138] L.C. Tien, D.P. Norton, B.P. Gila, S.J. Pearton, H.T. Wang, B.S. Kang, F. Ren, Detection of hydrogen with SnO$_2$ -coated ZnO nanorods, Appl. Surf. Sci. 253 (2007) 4748–4752.

[139] X. Li, X. Li, N. Chen, X. Li, J. Zhang, J. Yu, J. Wang, Z. Tang, CuO-in2O3 core-shell nanowire based chemical gas sensors, J. Nanomater. 2014 (2014).

[140] N. Singh, A. Ponzoni, R.K. Gupta, P.S. Lee, E. Comini, Synthesis of In$_2$O$_3$-ZnO core-shell nanowires and their application in gas sensing, Sensors Actuators, B Chem. 160 (2011) 1346–1351.

[141] F. Zhou, X. Li, J. Shu, J. Wang, Synthesis and visible light photo-electrochemical behaviors of In$_2$O$_3$-sensitized ZnO nanowire array film, J. Photochem. Photobiol. A Chem. 219 (2011) 132–138.

[142] Y. Zhou, C. Xia, X. Hu, W. Huang, A.A. Aref, B. Wang, Z. Liu, Y. Sun, W. Zhou, Y. Tang, Dye-sensitized solar cells based on nanoparticle-decorated ZnO/SnO$_2$ core/shell nanoneedle arrays, Appl. Surf. Sci. 292 (2014) 111–116.

[143] T. Wagner, T. Waitz, J. Roggenbuck, M. Fröba, C.D. Kohl, M. Tiemann, Ordered mesoporous ZnO for gas sensing, Thin Solid Films. 515 (2007) 8360–8363.

[144] Z. Wen, L. Zhu, Z. Zhang, Z. Ye, Fabrication of gas sensor based on mesoporous rhombus-

shaped ZnO rod arrays, Sensors Actuators, B Chem. 208 (2015) 112–121.

[145] X. Feng, J. Jiang, H. Ding, R. Ding, D. Luo, J. Zhu, Y. Feng, X. Huang, Carbon-assisted synthesis of mesoporous SnO_2 nanomaterial as highly sensitive ethanol gas sensor, Sensors Actuators, B Chem. 183 (2013) 526–534.

[146] A.Y. Lo, Y.C. Chung, W.-H. Hung, Y.C. Hsua, C.M. Tsenge, W.L. Zhanga, F.-K. Wanga, C.Y. Lin, $Pt_{20}Ru_xSn_y$ nanoparticles dispersed on mesoporous carbon CMK-3 and their application in the oxidation of 2-carbon alcohols and fermentation effluent, Electrochim. Acta. 227 (2017) 207–214.

[147] A.Y. Lo, Y. Jheng, T.C. Huang, C.M. Tseng, Study on RuO_2/CMK-3/CNTs composites for high power and high energy density supercapacitor, Appl. Energy. 153 (2015) 15–21.

[148] W.H. Hung, S.N. Lai, A.Y. Lo, Synthesis of Strong Light Scattering Absorber of TiO_2–CMK-3/Ag for Photocatalytic Water Splitting under Visible Light Irradiation, ACS Appl. Mater. Interfaces. 7 (2015) 8412–8418.

[149] K. Montiel-Centeno, D. Barrera, J. Villarroel-Rocha, J.J. Arroyo-Gómez, M.S. Moreno, K. Sapag, CMK-3 nanostructured carbon: Effect of temperature and time carbonization on textural properties and H_2 storage, Chem. Eng. Commun. 206 (2019) 1592–1606.

[150] M. Vorokhta, J. Morávková, D. Řimnáčová, R. Pilař, A. Zhigunov, M. Švábová, P. Sazama, CO_2 capture using three-dimensionally ordered micromesoporous carbon, J. CO_2 Util. 31 (2019) 124–134.

[151] R. Chen, J. Wang, Y. Xia, L. Xiang, Near infrared light enhanced room-temperature NO_2 gas sensing by hierarchical ZnO nanorods functionalized with PbS quantum dots, Sensors Actuators B Chem. 255 (2018) 2538–2545.

[152] C. Liewhiran and S. Phanichphantandast, Improvement of Flame-made ZnO Nanoparticulate

Thick Film Morphology for Ethanol Sensing, Sensors. 7 (2007) 650–675.

[153] D.K. Mishra, J. Mohapatra, M.K. Sharma, R. Chattarjee, S.K. Singh, S. Varma, S.N. Behera, S.K. Nayak, P. Entel, Carbon doped ZnO: Synthesis , characterization and interpretation, J. Magn. Magn. Mater. 329 (2013) 146–152.

[154] A.S. Alshammari, L. Chi, X. Chen, A. Bagabas, D. Kramer, A. Alromaeh, Z. Jiang, Visible-light photocatalysis on C-doped ZnO derived from polymer-assisted pyrolysis, RSC Adv. 5 (2015) 27690–27698.

[155] H. Pan, J.B. Yi, L. Shen, R.Q. Wu, J.H. Yang, J.Y. Lin, Y.P. Feng, J. Ding, J.H. Yin, Room-Temperature Ferromagnetism in Carbon-Doped ZnO, 127201 (2007) 1–4.

[156] J. Zhai, L. Wang, D. Wang, Y. Lin, D. He, T. Xie, UV-illumination room-temperature gas sensing activity of carbon-doped ZnO microspheres, Sensors Actuators, B Chem. 161 (2012) 292–297.

[157] Z.A. Alothman, A review: Fundamental aspects of silicate mesoporous materials, Materials (Basel). 5 (2012) 2874–2902.

[158] K. Ramesh, K.S. Reddy, I. Rashmi, A.K. Biswas, Porosity Distribution, Surface Area, and Morphology of Synthetic Potassium Zeolites: A SEM and N_2 Adsorption Study, Commun. Soil Sci. Plant Anal. 45 (2014) 2171–2181.

Appendices

A.1   Gas sensing apparatus

Figure A1-1: Experimental platform, composed of a delivery section to control the gas flow and concentrations through a set of MFCs, a sensing chamber to expose the sensor to the photons and gas (in the black box), and the electrical section which powers the LED and sensor, also monitors the sensor resistance by using a digital Multimeter.
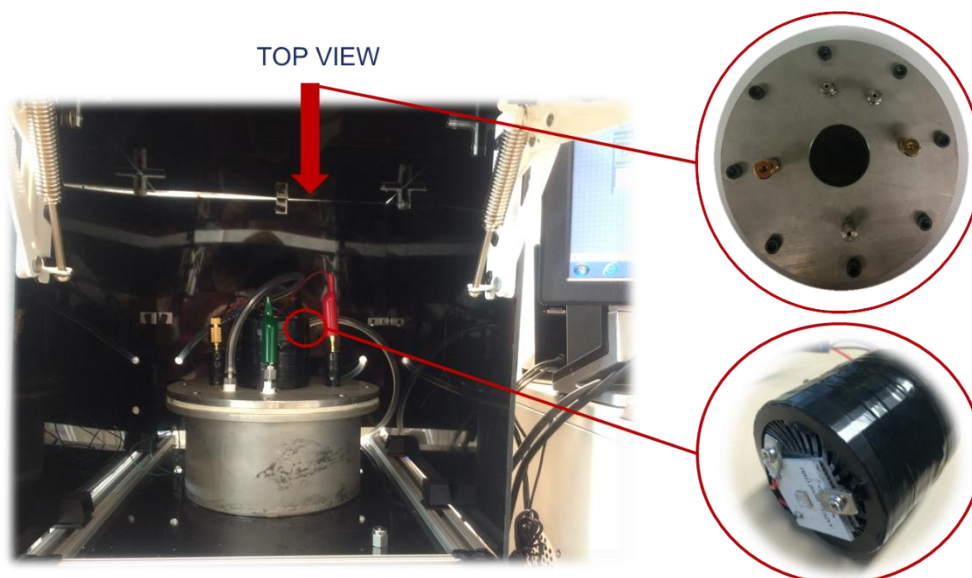

Figure A1-2: The black box which accommodates the reaction chamber and the radiation source. The chamber is made of stainless steel with a designated quartz window on the lid to allow UV transmission. UV-LED is mounted on a PCB and is connected to a thermo-electric cooler, a heat sink and a fan for heat dissipation.
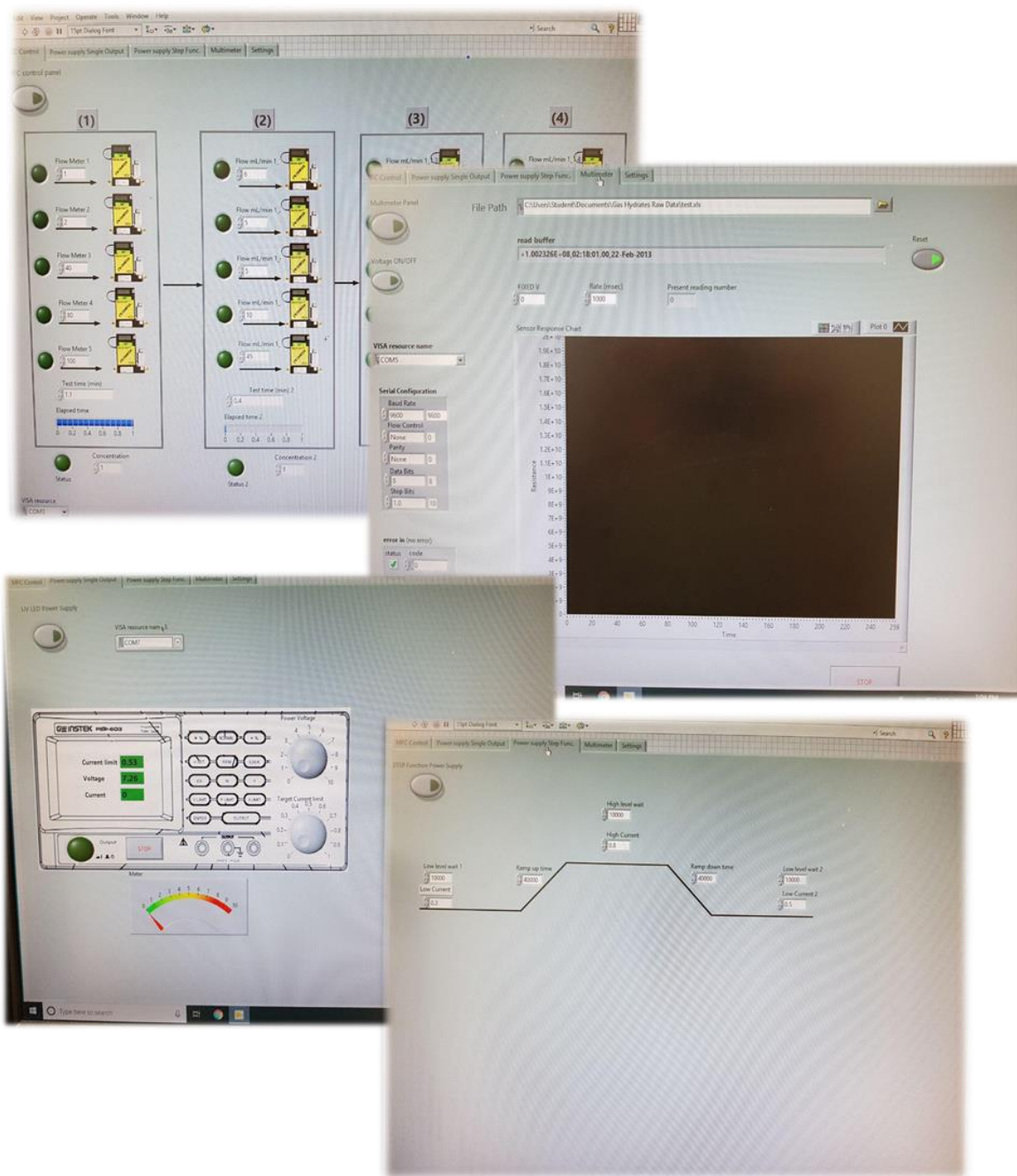
Figure A1-3: LabView interface which remotely controls the MFCs, UV-LED power supply, and digital multimeter, and continuously collects the data from the sensor. The program is able to expose the sensor to various concentrations of gases stepwise (up to 5 gases). It can also modulate the illumination for pulsed irradiation or sampling-and-hold method, explained in Chapter 8.

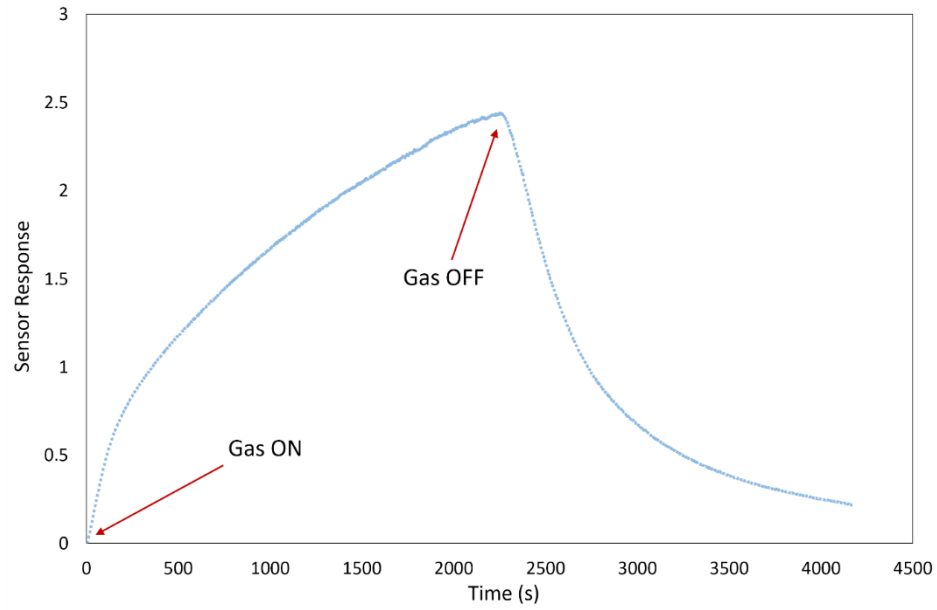## A.2 Effect of irradiation parameters on sensors' responses

Figure A2-1: In$_2$O$_3$ sensor failure in NO$_2$ detection due to stable adsorption of NO$_2$ molecules on the surface at low irradiance (25 mW/cm^2). The response signal did not recover completely (to its initial resistance level) after tuning off NO$_2$
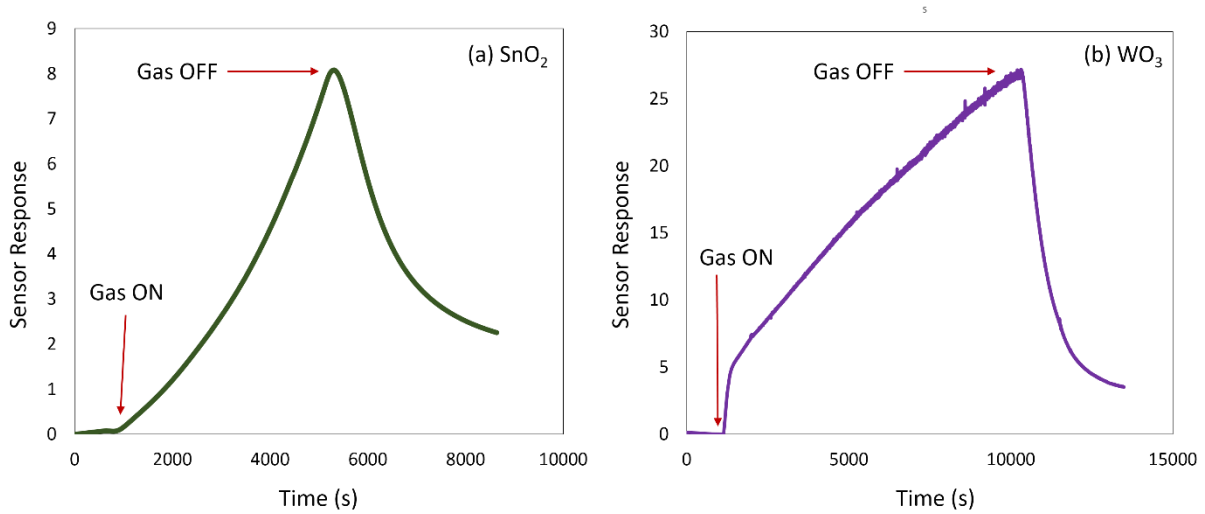

Figure A2-2: Sensor response failures to 5 ppm NO$_2$ under 365 nm UV-LED irradiation at 10 Hz pulsation frequency, a) SnO$_2$ b) WO$_3$. The response increased without reaching a steady-state plateau for over 2 hours.
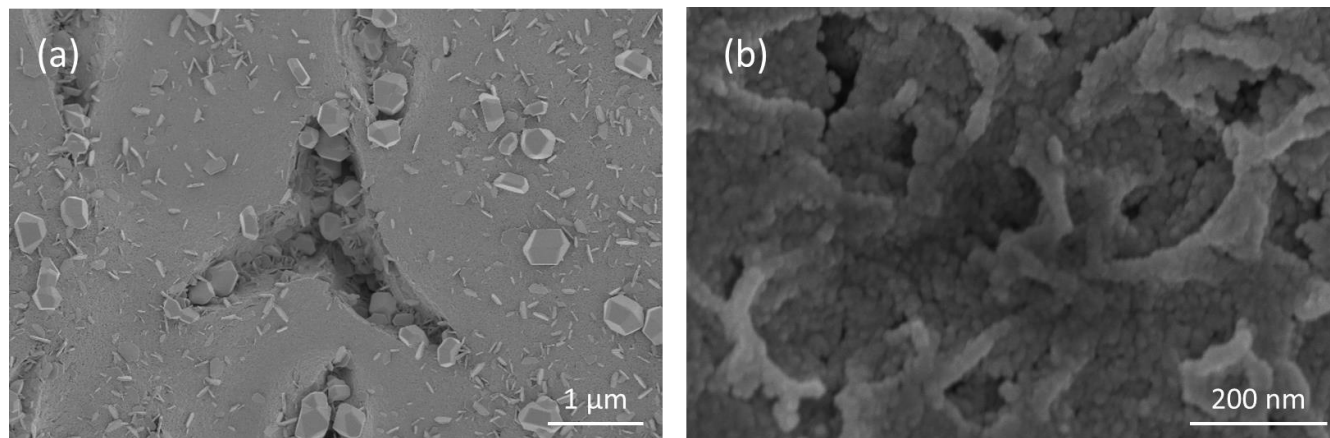
A.3 Core-shell synthesis

Figure A3-1: FE-SEM images of buried ZnO NWs in In_2O_3 shell material a) double dipping b) triple dipping. The results confirmed that excessive coating of ZnO NWs may results in losing nanowire structure and that an optimized deposition amount is required
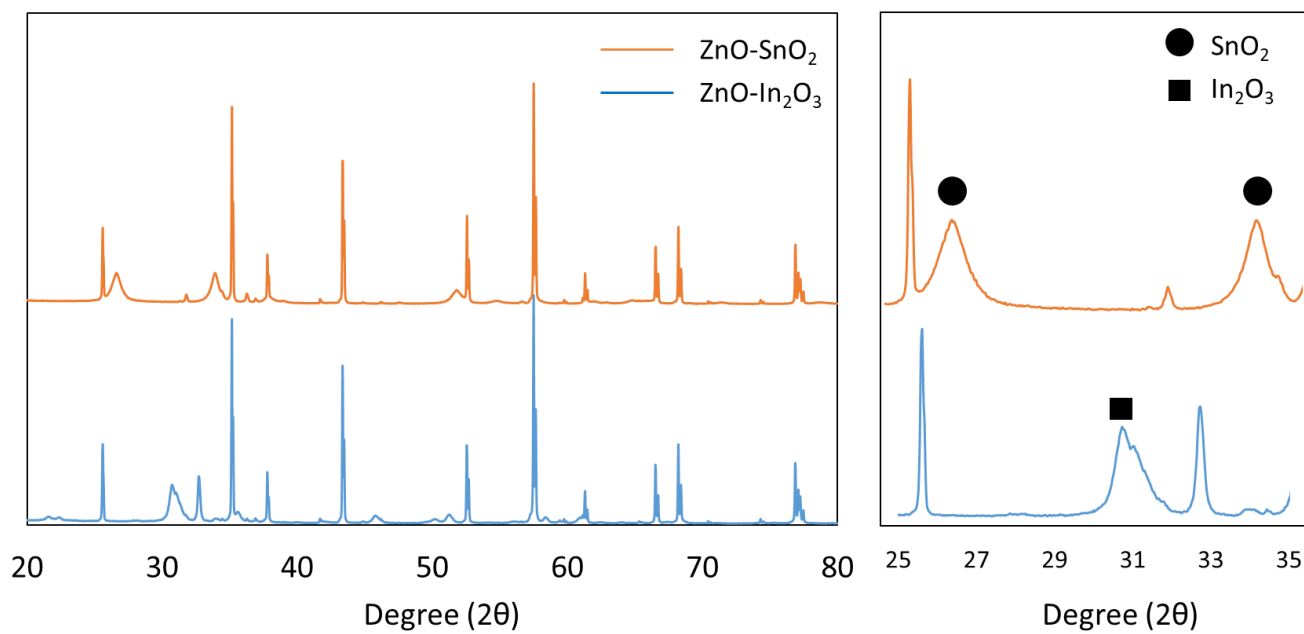

Figure A3-2: XRD results of excessive coated sample in core-shell structures. This confirms the existence of the coated materials as well as their phase and crystallinity

A.4   Effect of ZnO content on porosity of ZnO$_x$/CMK-3

Figure A4-1(a) shows the N$_2$ adsorption/desorption isotherm of SBA-15, CMK-3, and ZnO$_x$/CMK-3 samples. The SBA-15 template shows a typical type-IV isotherm with type-H1 hysteresis loop, representing an ordered mesoporous material with cylindrical-like pore channel and narrow pore size distribution. Instead, the replica CMK-3 presents its typical type-H$_2$ hysteresis loop, represent a rather broadened mesoporous distribution [157].
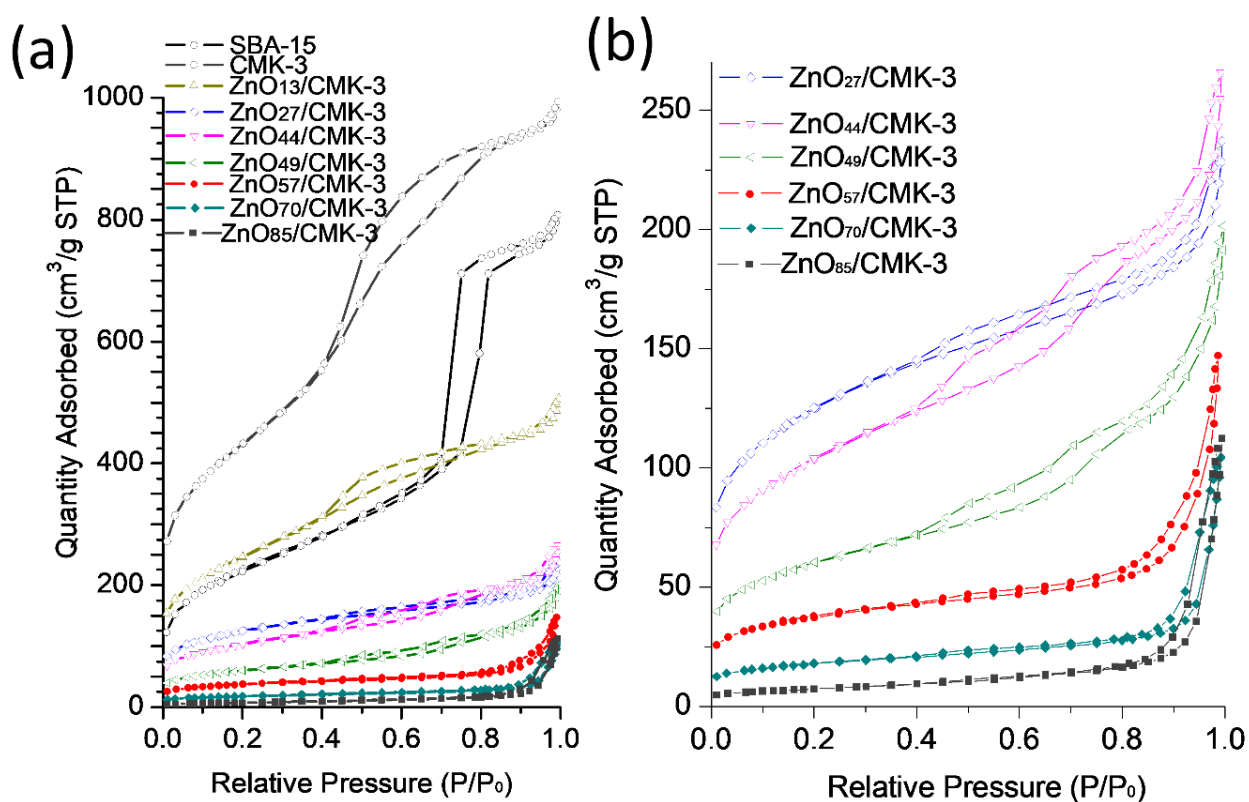

Figure A4-1: (a) N$_2$ adsorption/desorption isotherm of SBA-15, CMK-3, and ZnO$_x$/CMK-3 samples (b) Higher magnitude of hysteresis curve of ZnO$_x$/CMK-3 (x from 27 to 85)

By increasing ZnO content, ZnO_x/CMK-3 (x from 0 to 57), the isotherm curve gradually transferred from type-H_2 to type-H_3 hysteresis loops (Figure A4-1(b)). According to the empirical classification of hysteresis loops given by International Union of Pure and Applied Chemistry (IUPAC), the type-H_3 hysteresis loop with adsorption occurs at low relative pressure ($P/P_0 < 0.1$) represents the existence of slit-shaped micropores [158]. In other words, upon addition of ZnO content, most of the mesopores of ZnO_x/CMK-3 are filled with ZnO until 57 wt% loading concentration. However, there are still considerable microporous surface area left. Further increase the ZnO content would not lead to any change of hysteresis loop type, but would decline the quantity adsorbed.

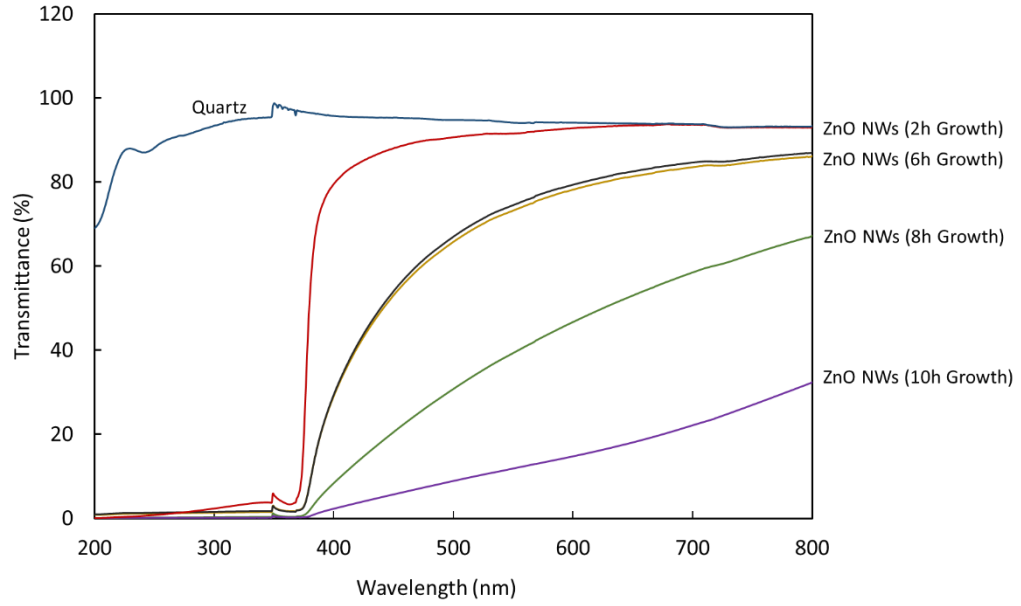## A.5   UV penetration depth and surface temperature

Figure A5-1: UV penetration analysis on ZnO NWs grown on quartz sheet. The trend in UV transmission is decreasing when the nanowires length is increased. Given the low transmission values at wavelengths around 360 nm, it can be concluded that the photons are mostly absorbed by the layer. The samples with 6 hour growing time seem promising as homogeneous exposed illumination of the entire surface is guaranteed.
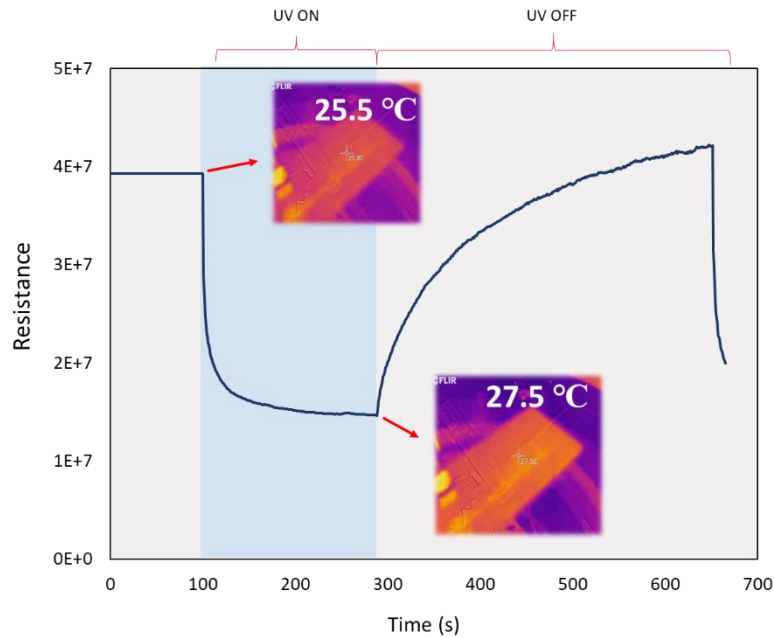

Figure A5-2: Temperature variation on sensor surface in a sensing cycle. The temperature upon exposure to UV is increased slightly but remained in the range of ambient condition.